

INVESTIGATION INTO HIGH SPECTRAL RESOLUTION LIDAR TECHNOLOGIES

by

Martha Wallis Dawsey

A Dissertation Submitted to the Faculty of the

COLLEGE OF OPTICAL SCIENCES

In Partial Fulfillment of the Requirements
For the Degree of

DOCTOR OF PHILOSOPHY

In the Graduate College

THE UNIVERSITY OF ARIZONA

2013

THE UNIVERSITY OF ARIZONA
GRADUATE COLLEGE

As members of the Dissertation Committee, we certify that we have read the dissertation prepared by Martha Dawsey, titled Investigation Into High Spectral Resolution Lidar Technologies, and recommend that it be accepted as fulfilling the dissertation requirement for the Degree of Doctor of Philosophy.

_____ Date: (9-25-2013)

John Reagan

_____ Date: (9-25-2013)

Tom Milster

_____ Date: (9-25-2013)

Jose Sasian

Final approval and acceptance of this dissertation is contingent upon the candidate's submission of the final copies of the dissertation to the Graduate College.

I hereby certify that I have read this dissertation prepared under my direction and recommend that it be accepted as fulfilling the dissertation requirement.

_____ Date: (9-25-2013)

Dissertation Director: John Reagan

STATEMENT BY AUTHOR

This dissertation has been submitted in partial fulfillment of the requirements for an advanced degree at the University of Arizona and is deposited in the University Library to be made available to borrowers under rules of the Library.

Brief quotations from this dissertation are allowable without special permission, provided that an accurate acknowledgment of the source is made. Requests for permission for extended quotation from or reproduction of this manuscript in whole or in part may be granted by the head of the major department or the Dean of the Graduate College when in his or her judgment the proposed use of the material is in the interests of scholarship. In all other instances, however, permission must be obtained from the author.

SIGNED: Martha W. Dawsey

ACKNOWLEDGMENTS

I would like to thank my advisor, Dr. John Reagan, for his guidance and encouragement in my research. His deep knowledge of the subject matter has been invaluable, and I will always be grateful for his expertise, constructive inputs, and wisdom.

Additionally, I would like to thank Dr. Tom Milster and Dr. Jose Sasian for the effort of being on my dissertation committee, and for their advice and support during my time in graduate school. I will be forever grateful to Dr. Gary Gimmestad and the lidar group at Georgia Tech Research Institute for starting me along this path in 2003. I would not have pursued this research without them.

I would also like to thank the lidar group at NASA Langley Research Center, which includes Dr. Chris Hostetler, Dr. Tony Cook, Dr. David Harper, and Dr. Johnathan Hair, for both funding my research and being supportive and available. Additionally, the support of the lidar group at Montana State University, which includes Dr. David Repasky, Kerry Neal, and Dr. David Hoffman, has been invaluable. I have benefited greatly from the willingness of both groups to share their expertise, hardware, and advice. I am grateful to Photon Engineering, for providing their software, FRED, and their support for this research. Also, Sandra Myers, and the students in the LaRC Graduate Student Researchers Program (GSRP) were a large source of support, and I am thankful that I was able to share that experience with them all. Additionally, I would like to express my gratitude to the Optics Branch at NASA Goddard Space Flight Center for their patience and understanding as I have finished this research.

For Amber Young, Lori Moore, Tom Zobrist, Rene Zehnder, Jennifer Harwell, Kali Wilson, Miena Armanious, Anna Britt Mahler, James Johnson, Scott Gibb, Tim Renkoski, Chris McPherson, Blake Anderton, Srikanth Venkata, and the legions of graduate students who have encouraged me and walked with me through graduate school, I have only love, respect, and gratitude for our time together.

To my family, Rick and Susan Dawsey, Curt, James, and Rebecca, I would like to express my love and gratitude for your continuous support and encouragement in all aspects of my life. To my in-laws, I would like to give my thanks for your love and constant belief in me.

Finally, to my husband, Erich, I would like to express my deepest love and thanks: your patience, support, and love made this dissertation possible. You have been my partner and my home in this, as in all things, and I am so grateful.

DEDICATION

I left home to complete this research, and I'd like to dedicate it to my loved ones who are no longer there:

James R. Dawsey, Sr. (1914 - 2007), my grandfather,

Eugene M. Foster (1957 - 2011), my uncle, and

Curt D. de Leon (1932- 2012), my father-in-law.

TABLE OF CONTENTS

LIST OF FIGURES.....	9
LIST OF TABLES.....	16
ABSTRACT.....	18
CHAPTER 1: INTRODUCTION AND BACKGROUND.....	19
1.1 Purpose of Dissertation.....	19
1.2 Motivation.....	19
1.3 Background and Significance.....	21
1.3.1. Lidar.....	21
1.3.2. Lidar Equation.....	23
1.3.3. High Spectral Resolution Lidar.....	29
1.3.4. High Spectral Resolution Lidar Equation.....	32
1.3.5. Filters for Comparisons.....	34
1.4 Methodology.....	35
1.4.1. Software.....	37
1.4.2. Comparison Criteria.....	38
1.5 Modeling the Lidar Return.....	40
1.5.1. Simple Gaussian Method for Modeling the Lidar Return.....	40
1.5.2. Bruneau Method for Modeling the Lidar Return.....	42
1.6 Goals and Contributions.....	44
CHAPTER 2: THE SPHERICAL FABRY-PEROT INTERFEROMETER.....	47
2.1 Introduction and Description.....	47
2.2 Modeling of the SFPI.....	50
2.2.1. Coherent Ray Tracing in Zemax.....	51
2.2.2. SFPI Modeling in FRED.....	55
2.2.3. Source Description.....	57
2.3 SFPI Analysis.....	59
2.3.1. Spectral Analysis: Finesse in the SFPI.....	59
2.3.1.1. Finesse from Reflectivity.....	60
2.3.1.2. Finesse from Spherical Aberration.....	66
2.3.1.3. Resolving Power in a SFPI.....	70
2.3.1.4. Spectral Comparison of FRED Model to MSU Experiment.....	71
2.3.2. Angular Analysis of the SFPI.....	73
2.3.3. Analysis of the SFPI Efficiency.....	78
2.4 Summary of SFPI Analysis.....	81

TABLE OF CONTENTS – *Continued*

CHAPTER 3: THE WIDE ANGLE MICHELSON INTERFEROMETER.....	83
3.1 Introduction and Description.....	83
3.1.1. Standard Michelson Interferometer.....	85
3.1.2. Wide-Angle Michelson Interferometer.....	86
3.1.3. The WAMI at NASA LaRC.....	88
3.2 WAMI Modeling.....	90
3.2.1. Modeling the WAMI in Ray-Tracing Software.....	90
3.2.2. FRED Model Verification.....	95
3.2.3. WAMI Transmission Functions.....	96
3.2.3.1. Modeled Transmission Function.....	97
3.2.3.2. Bruneau Transmission Function.....	97
3.2.3.3. Modeling the Signal on the Detector.....	99
3.3 Analysis of the WAMI.....	104
3.3.1. Spectral Analysis of the WAMI.....	104
3.3.1.1. The Resolving Power of the WAMI.....	104
3.3.1.2. Effect of the Glass Arm on WAMI Signal.....	105
3.3.2. Angular Analysis of WAMI.....	109
3.3.2.1. WAMI Tilt Angle.....	109
3.3.2.2. WAMI Acceptance Angle.....	112
3.3.3. Analysis of the WAMI Efficiency.....	114
3.4 Summary of the WAMI Analysis.....	115
 CHAPTER 4: COMPARATIVE ANALYSIS AND DESIGN	
METHODOLOGY.....	116
4.1 Introduction.....	116
4.2 Comparative Analysis of a SFPI and a WAMI.....	117
4.2.1. Spectral Comparative Analysis.....	117
4.2.2. Angular Comparative Analysis.....	119
4.2.3. Efficiency Comparative Analysis.....	123
4.2.3.1. Throughput.....	124
4.2.3.2. Transmission.....	125
4.2.4. Comparison with the Iodine Vapor Filter.....	128
4.3 Design Methodology for a Narrow Band Filter in a HSRL.....	128
4.3.1. Specifying the Narrow Band Filter.....	129
4.3.2. Spectral Design Methodology.....	132
4.3.2.1. SFPI Spectral Design Methodology.....	136
4.3.2.2. WAMI Spectral Design Methodology.....	138
4.3.2.3. Summary of Spectral Design Methodology.....	140

TABLE OF CONTENTS – *Continued*

- 4.3.3 Angular Design Methodology..... 142
 - 4.3.3.1 SFPI Angular Design Methodology..... 143
 - 4.3.3.2 WAMI Angular Design Methodology..... 148
 - 4.3.3.3 Summary of Angular Design Methodology..... 151
- 4.3.4 Efficiency Design Methodology..... 153
 - 4.3.4.1 SFPI Design for Efficiency..... 154
 - 4.3.4.2 WAMI Design for Efficiency..... 156
 - 4.3.4.3 Summary of Efficiency Design Methodology..... 158
- 4.3.5 Summary of Design Methodology..... 160
- 4.4 Summary 161

- CHAPTER 5: CONCLUSIONS AND FUTURE WORK.....162**
 - 5.1 Conclusions..... 162
 - 5.2 Future Work..... 164

- APPENDIX A..... 165**

- APPENDIX B..... 167**

- APPENDIX C..... 169**

- APPENDIX D..... 174**

- REFERENCES.....175**

LIST OF FIGURES

Figure 1-1: A block diagram of a general lidar.....	22
Figure 1-2: On the left is an example of a bi-axial lidar geometry, and on the right is an example of a co-axial lidar geometry.....	24
Figure 1-3: The angular distribution of Mie scattering changes with the size parameter, with dramatically more scattering for larger size parameters.....	27
Figure 1-4: On the left is a block diagram of the receiver optics for a HSRL. On the right are the signals on the detectors.....	31
Figure 1-5: Flow diagram showing the analysis steps to arrive at the comparative analysis of the WAMI and SFPI for a narrow band filter in a HSRL.....	37
Figure 1-6: The incident Doppler broadened lidar return incident on the HSRL, modeled using a simple Gaussian.....	42
Figure 1-7: The Doppler broadened lidar return modeled using a simple Gaussian, at 355nm, 532nm, and 1064nm, going from left to right. The wavelength range is the same scale for each.....	42
Figure 1-8: The incident Doppler broadened lidar return incident on the HSRL, modeled using the technique outlined in Bruneau (2003), and a scale factor of 75..	44
Figure 1-9: The Doppler broadened lidar return modeled using the Bruneau model, at 355nm, 532nm, and 1064nm, going from left to right. The wavelength range is the same scale for each.....	44
Figure 2-1: Diagram of the HSRL at MSU (Hoffman et al. 2012).....	49
Figure 2-2: Properties for a Detector Rectangle in the NSC Zemax mode. Note the circled "Normalize Coherent Power" switch.....	51
Figure 2-3: The PPP, as modeled in Zemax.....	52
Figure 2-4: Analysis of a plane parallel plate with the "Normalize Coherent Power" switched off.....	54
Figure 2-5: Analysis of a PFPI with the "Normalize Coherent Power" switched on.....	54

LIST OF FIGURES – *Continued*

Figure 2-6: The transmitted and reflected power from a PPP, exhibiting the ability of FRED software to model both the interferometric effects and conservation of energy over a range of wavelengths.....	56
Figure 2-7: FRED model of SFPI with source focusing in the center of the cavity..	56
Figure 2-8: The coherent ray structure in FRED. The secondary beamlets keep track of the divergence and the waist of the primary, or base, ray. From the FRED Application Note, "Modeling Coherence" (2013).....	58
Figure 2-9. Fiber Coupling Lens and Beam Size.....	58
Figure 2-10. For each entrant ray A, there are four emergent rays, at A, B, C and D.....	60
Figure 2-11. The transmitted power versus the cavity separation for a confocal cavity with an off-axis, single-mode source. The finesse of these fringes is 25.....	61
Figure 2-12. The transmitted power versus the cavity separation for a confocal cavity with an on-axis, single-mode source. The finesse of these fringes is 50.....	63
Figure 2-13: The transmitted power versus the cavity separation for an on-axis source with mode 1,0.....	64
Figure 2-14: The transmitted power versus the cavity separation for an on-axis source with mode 1,1.....	64
Figure 2-15: A comparison of the modeled and theoretical finesse for a range of reflectivity values.....	66
Figure 2-16a. In a paraxial cavity, an incident beam would traverse the path length four times before closing its trajectory.....	68
Figure 2-16b. In a cavity that takes spherical aberration into account, the trajectory does not close, and after four transits, the path length deviates from paraxial by an amount described in equation 2-14.....	68
Figure 2-17. The effect of the beam height at mirror 1 on the reflectivity finesse, spherical aberration finesse, and the total finesse for the MSU SFPI.....	70

LIST OF FIGURES – *Continued*

Figure 2-18. The resonances for a 532 nm source compared with a 1064nm source, as determined by FRED model.....	72
Figure 2-19: The measured cavity transmission and reflection as a function of cavity separation for 532nm (top) and the transmission for 1064nm (bottom), from the HSRL at MSU (Hoffman et al. 2012).....	72
Figure 2-20: Illustration of the acceptance angle limitations for a PFPI.....	73
Figure 2-21: Illustration of the effect that a change in the incident angle will have on the beam height at the center of the SFPI.....	75
Figure 2-22: The transmission for an on-axis SFPI source, for a range of incident angles.....	76
Figure 2-23: The FRED model of the SFPI at a resonant cavity length, with the source angle tilted at 0.33 degrees in the y-axis. The transmission detector is on the right, highlighted in red. It's apparent that some transmitted rays (yellow) are not incident on the detector.....	77
Figure 2-24: The transmission for a SFPI source that is offset from the optical axis by 1/2mm, for a range of incident angles.....	78
Figure 3-1: A schematic diagram of a WAMI, from Liu et al. (2012) at NASA LaRC.....	85
Figure 3-2: A standard Michelson interferometer (Hilliard 1966).....	86
Figure 3-3: A wide-angle Michelson interferometer (Hilliard 1966).....	86
Figure 3-4: A schematic of the WAMI, and the tilt necessary to separate the forward and reverse channels (Liu et al. 2012).....	89
Figure 3-5: Triple-V AR coating designed for 355, 532, and 1064 nm, from CVI-Melles Griot (Antireflection 2013).....	90
Figure 3-6: High Reflective coating, from CVI-Melles Griot (Optical Coatings 2013).....	90

LIST OF FIGURES – *Continued*

Figure 3-7: A schematic of the WAMI modeled in FRED.....	91
Figure 3-8: Spot diagrams shown for 9 different field angles, at the entrance face of the WAMI. These diagrams were produced using a Zemax file provided by NASA LaRC.....	92
Figure 3-9: The distance "S" is varied to find the optimal spacing between Mirror 1 (the glass arm) and the beam splitter, in order to eliminate material ambiguity errors in FRED.....	94
Figure 3-10: The power on each detector for a range of separations between the beam splitter and the glass arm (Mirror 1), labeled "S" in figure 3-9.....	94
Figure 3-11: The irradiance profile at the forward detector for a WAMI with 1.978E-3 degrees of tilt on the left, and for a WAMI with 8.475E-4 degrees of tilt on the right. Note the expected 7 fringes on the left and the 3 fringes on the right.....	96
Figure 3-12: Transmission through two paths in the WAMI, using the FRED model.....	97
Figure 3-13: Transmission through two paths in the WAMI, using the Bruneau transmission function.....	99
Figure 3-14: Comparisons of the signal on the detector for four scenarios. The signals are evaluated separately. (a) The Bruneau return model with the Bruneau transmission function, (b) the Simple Gaussian return model with the Bruneau transmission function, (c) the Bruneau return model with the FRED transmission function, and (d) the Simple Gaussian return model with the FRED transmission function.....	102
Figure 3-15: The power on each detector (Signal 1 and 2) for the four scenarios shown in Figure 3-14. It is labeled so that where A x B, A = the model for the lidar return, and B = the model for the transmission function.....	103
Figure 3-16: The effect of the glass arm length on the signal, for the WAMI at LaRC. The x-axis is the shift away from the LaRC WAMI glass arm length of 87.578um, indicated by the red vertical line.....	106

LIST OF FIGURES – *Continued*

Figure 3-17: The effect of the index of refraction on the WAMI signal. The red vertical line indicates the index for the LaRC WAMI.....	107
Figure 3-18: The effect of the WAMI's index on the signal. This plot is a close-up of figure 3-17. The red vertical line indicates the index for the LaRC WAMI.....	108
Figure 3-19: The optimal OPD, the OPD for a standard Michelson interferometer, and the OPD for a WAMI, plotted for a range of tilt angles.....	110
Figure 3-20: The difference between the optimal OPD and the WAMI OPD, plotted with the difference between the optimal OPD and the OPD for a standard Michelson, for a range of tilt angles, plotted in wave units.....	111
Figure 3-21: The power on each detector for a range of WAMI tilt angles, using the FRED model set at the central wavelength of 355nm. The power sum, and the number of rays on each detector is also plotted. In this plot, the source has no divergence, and is perfectly centered.....	112
Figure 3-22: The power on each detector for a range of source angles, and the ray count for the respective detectors. For the LaRC WAMI, with a full field source divergence of 0.92 degrees, and a WAMI tilt of -1 degrees.....	113
Figure 4-1: The RP of the LaRC WAMI for a range of wavelengths. The maximum RP is 11E5 at 0.2 um.....	118
Figure 4-2: The RP of the MSU SFPI for a range of wavelengths. The maximum RP is 5.5E7 at 0.2 um.....	118
Figure 4-3: The normalized power for the transmitted and reflected channels in the SFPI, for a range of source angles. The ray count is also plotted, and it should be noted that this is identical for both the transmitted and reflected channels.....	120
Figure 4-4: The angular dependent normalized power for the transmitted and reflected channels in the SFPI when the beam is focused onto the cavity center. The ray count is also plotted.....	121
Figure 4-5: The departure from the optimal OPD (in wavelength units) for both a standard Michelson and for the LaRC WAMI.....	122

LIST OF FIGURES – *Continued*

Figure 4-6: The power on each detector for a range of source angles, and the ray count for each detector. The plot is centered on the WAMI tilt angle of -1 degree, and then offset by the half-field divergence of 0.46 degrees.....	123
Figure 4-7: Illustration of the two possible directions for the narrow band HSRL filter to take. Figure A shows the elimination of the Mie signal from the total lidar return using a notch filter, and figure A shows the elimination of the Rayleigh signal from the total lidar return using a bandpass filter. Both the MSU SFPI and the LaRC WAMI use the method in figure A.....	134
Figure 4-8: The wavelength dependent bandwidth necessary to remove the Mie signal from a HSRL return, for a range of filtering levels.....	135
Figure 4-9: The reflectivity dependent RP, for a SFPI operating at 355nm, for a range of mirror radius of curvatures.....	137
Figure 4-10: The SFPI RP for a range of wavelengths and mirror reflectivity values.....	138
Figure 4-11: The wavelength dependent WAMI RP for a range of glass arm lengths.....	139
Figure 4-12: The wavelength dependent WAMI RP for a range of air arm indices of refraction.....	140
Figure 4-13: Flow chart showing the spectral design methodology discussed in section 4.3.2.....	141
Figure 4-14: The angle dependent, normalized power transmitted through a SFPI. The beam is focused into the center of the SFPI with a lens, and plots are included for a range of focal lengths.....	144
Figure 4-15: The effect of the incident angle on the SFPI transmission, for a) a source that is on-axis, b) a source that 1/2mm off axis, and c) a source that is 5mm off axis.....	146
Figure 4-16: The total angular dependent SFPI finesse, for a range of wavelengths.....	147

LIST OF FIGURES – *Continued*

Figure 4-17: The angular dependent WAMI OPD, for a range of glass arm lengths.....	149
Figure 4-18: The angular dependent WAMI OPD, for a range of air arm lengths....	149
Figure 4-19: The angular dependent WAMI OPD, for a range of air arm indices.....	150
Figure 4-20: The power on each detector for a range of source angles, and the ray count for the respective detectors. For the LaRC WAMI, with a half field source divergence of 0.9 degrees, and a tilt of -1 degrees.....	151
Figure 4-21: Flow chart showing the angular design methodology discussed in section 4.3.3.....	152
Figure 4-22: The SFPI Throughput vs the finesse, for a range of possible cavity spacings.....	155
Figure 4-23: The transmitted SFPI power and ray count for a source that is on axis, 0.5mm off axis, 1mm off axis, 1.5mm off axis, and 5mm off axis (from left to right and top to bottom).....	156
Figure 4-24: The WAMI throughput versus the RP, for a range of design wavelengths.....	157
Figure 4-25: The WAMI wavelength dependent transmission function, for a range of glass arm lengths.....	158
Figure 4-26: Flow chart showing the efficiency design methodology discussed in section 4.3.4.....	159

LIST OF TABLES

Table 2-1: Specifications for the modeled plane parallel plate.....	53
Table 2-2: Finesse comparison for a range of reflectivity values, and an incident angle of 0.2 degrees at 1E-3mm above the optical axis.....	66
Table 4-1: The RP for the WAMI and SFPI at four common wavelengths.....	118
Table 4-2: The transmission of each interferometer channel over a range of wavelengths. In these calculations, the instruments are “as built” by MSU and NASA LaRC.....	125
Table 4-3: Values used to adjust the SFPI model for alternate wavelengths.....	127
Table 4-4: The transmission of each filter channel over a range of wavelengths. The instruments are wavelength adjusted, and ideal illumination is assumed for the SFPI.....	127
Table 4-5: A list of candidate specifications for the design of a SFPI.....	131
Table 4-6: A list of candidate specifications for the design of a WAMI.....	132
Table 4-7: The bandwidth at certain filtering levels for common lidar wavelengths.....	136
Table 4-8: The trend of optimization for an increase RP using a SFPI.....	142
Table 4-9: The trend of optimization for an increase RP using a WAMI. The starred (*) specifications have the caveat that the aforementioned QZP be maintained.....	142
Table 4-10: The angular window for transmission levels of a SFPI , for a range of focal lengths.....	145
Table 4-11: The trend of optimization for an increased acceptance angle using a SFPI.....	153
Table 4-12: The trend of optimization for an increase in the acceptance angle using a WAMI. The starred (*) specifications have the caveat that the aforementioned QZP be maintained.....	153

LIST OF TABLES – *Continued*

Table 4-13: The trend of optimization for an increased throughput using a SFPI. A balance between the RP and throughput is found at 70% of the initial RP (Connes 1956, Vaughn 1989)..... 160

Table 4-14: The trend of optimization for an increase in the throughput using a WAMI. The starred (*) specifications have the caveat that the aforementioned QZP be maintained.....160

ABSTRACT

The Intergovernmental Panel on Climate Change (IPCC) found in their 2007 report that aerosol radiative forcing contributed larger uncertainties to estimates affecting future climate change than any other radiative forcing factor. Lidar is a tool with which this uncertainty can be reduced, increasing our understanding of the impact of aerosols on climate change. Lidar, or laser radar, is a monostatic active remote sensing technique used to measure aerosols and particulates in the atmosphere, with accuracies comparable to in-situ measurements (Russell 2002). High Spectral Resolution Lidar (HSRL) systems use a narrow band filter to spectrally separate Doppler broadened aerosol and molecular back-scattered return signals, which allows for range resolved profiles of aerosol extinction and backscatter. The narrow band filter is a key component, for which two novel approaches are currently being used: NASA Langley Research Center has implemented a wide-angle Michelson interferometer in the second version of their airborne HSRL, and Montana State University is using a spherical Fabry-Perot interferometer in a ground based HSRL. In this research, a comprehensive comparative analysis of these two interferometric filters is performed, the result of which is a methodology for the design of narrow band filters for HSRL systems. The techniques presented identify the critical components and analyze the performance of each filter based on the spectral and angular properties, as well as the efficiency.

CHAPTER 1: INTRODUCTION AND BACKGROUND

1.1 Purpose of Dissertation

The purpose of this dissertation is to develop a generalized methodology for the design of narrow band filters to be used in a High Spectral Resolution Lidar (HSRL).

1.2 Motivation

In their 2007 report on the physical science basis for climate change, the Intergovernmental Panel for Climate Change (Solomon et al., 2007), found that aerosols contribute the largest uncertainty to our understanding of how radiative forcing factors affect climate change. Radiative forcing relates changes in the surface temperatures to the net irradiance (W/m^2) at the tropopause (Ramaswamy 2002). An increase in net global irradiance (positive radiative forcing) is associated with a warming of global temperatures, while negative radiative forcing is associated with a decrease in net global irradiance (global cooling). Our understanding of direct aerosol radiative forcing has increased from a very low level of understanding to a medium-low level (a 20% to 50% confidence) of scientific understanding, so that a value of $-0.5 \pm 0.4 W/m^2$ can now be given as the total direct aerosol radiative forcing across all aerosol types. Indirect aerosol radiative forcing occurs when anthropogenic aerosols effect clouds, causing an indirect cloud albedo effect, which has an estimated value of $-0.7 W/M^2$ (Solomon et al., 2007). Because of their negative radiative forcing, atmospheric aerosols likely

counteract the positive radiative forcing effect of greenhouse gases, causing a lower global mean temperature rise over the last 50 years (Solomon et al., 2007, pp60).

Surface based aerosol lidar systems, in combination with satellite observations, have provided a “near-global” picture of aerosol properties, including size distribution, chemical composition, scattering and absorption (Solomon et al., 2007). These aerosol observations have been made with in-situ measurements, satellites, and ground based aerosol lidar networks, such as the European Aerosol Research Lidar Network (Matthias 2004) and the Micro-Pulse Lidar Network (Welton et al. 2001). The accuracy of these lidar observations compare favorably to the best in-situ measurements currently in use (Russell et al. 2002), and provide continuous vertical profiles of aerosol backscatter and extinction. The vertical profile allows for a better understanding of the indirect aerosol radiative forcing through observing how aerosols affect clouds (Feingold 1999) and a better understanding of the direct aerosol radiative forcing (Haywood and Ramaswamy 1998, Solomon et al., 2007).

High Spectral Resolution Lidar (HSRL) is one of the more advanced technologies used in understanding atmospheric aerosols. Moreover, with additional wavelengths, HSRL data could be obtained simultaneously at several wavelengths, leading to a better understanding of atmospheric aerosols. A limiting factor in the construction of a multi-spectral HSRL is the lack of a multi-spectral narrow band filter, which is addressed in this research.

1.3 Background and Significance

1.3.1 Lidar

Lidar stands for LIght Detection And Ranging, and is commonly described as laser radar. Lidar is a stable way to profile atmospheric scattering properties along an extended path in any direction in the visible wavelength range. An advantage of a lidar over other similar technologies is it is monostatic; lidar systems do not require hardware at each end of an extended path to take data. Additionally, it gives a profile of the extinction and scattering along a path, not just the mean value along a path. The operating range of a lidar is not fixed, but can be optimized based on the application and operating conditions, allowing for a wider range of measurements.

There are disadvantages to operating a lidar, chief among them being the expense. The Micro-Pulse Lidar (MPL) is the first commercially available, moderately priced lidar (Spinhirne 1993); a new MPL site costs between \$100K and \$200K. Additionally, the data processing of a lidar system can be very complex, resulting in the need for unique algorithms for each new lidar (a notable exception to this is the MPL). The complexity of the instruments also requires operators with a high level of knowledge and experience, which adds to the expense. Another disadvantage is that many lidars are not eye-safe, which curtails their usefulness.

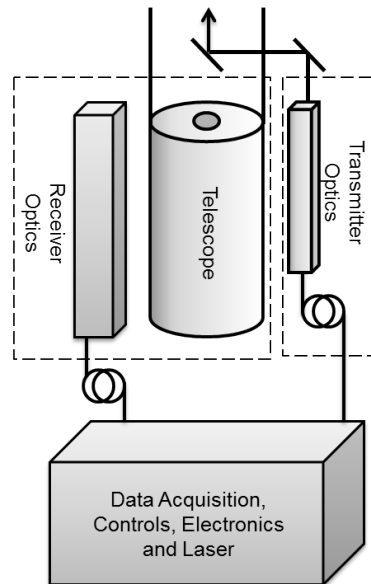


Figure 1-1: A block diagram of a general lidar.

There are three main components to a basic lidar system: the transmitter, the receiver, and the data acquisition system, as shown in Figure 1-1. In an atmospheric lidar, a pulsed laser beam is transmitted into the atmosphere, where it is scattered and absorbed by particulates and molecules. The backscattered photons are collected by the lidar receiver, where they are detected and the detector response is recorded as a function of time. The data acquisition system uses complex algorithms, based on the particular lidars geometry and function, to produce useable data. This technology has a wide range of applications, including topography (Yu, 2011), measuring trace gas concentrations (Riris, 2010), aerosol properties (Russell, 1982), turbulence (Gimmestad, 2007), temperature (Khanna, 2012), and cloud properties (Chen, 2002). However, all lidar instruments have the lidar equation in common.

1.3.2 Lidar Equation

The lidar equation solves for the number of photons, $P(R)$, received from a specified range, R , for one pulse of the laser. The complexity of this equation contributes to the intricacy of lidar technology in general. Because the lidar equation depends in part on the geometry of an individual instrument, new algorithms must be developed for each lidar. Equation 1-1 gives a general form of the lidar equation, where K is the instrument function, $G(R)$ is the geometric factor, $\beta(R)$ is the backscatter, and $T(R)$ is the round-trip transmission. Each of these is developed more fully in the following section.

$$P(R) = K G(R) \beta(R) T(R) \quad (1-1)$$

The function of the instrument, K , includes quantities that are determined by the hardware in that particular lidar, and is not related to the measurement range R . In equation 1-2, P_0 is the average power of a single pulse, τ is the temporal pulse length of the laser transmitter, A is the area of the primary collecting optics, c is the speed of light, and η is the overall system efficiency. The system efficiency includes the efficiency of the optics, as well as the quantum efficiency of the detector.

$$K = \frac{P_0 c \tau}{2} A \eta \quad (1-2)$$

The range dependent geometric factor $G(R)$, shown in equation 1-3, takes the overlap function, O , into account.

$$G(R) = \frac{O}{R^2} \quad (1-3)$$

The overlap function is a measure of the overlap between the transmitted laser beam and the receiver field-of-view. Generally, the overlap function is assumed to be either 0 or 1, depending on whether or not full overlap has been reached. However, short range lidar returns can occur below full overlap and create problems in the data processing. In order to use these returns, the overlap function must be known, but currently there is no way to practically determine the overlap function except experimentally, and this is not realistic in an operational lidar because it must be re-determined with every adjustment to the system (Sassen, 1982). Because of this, full overlap is assumed for this research.

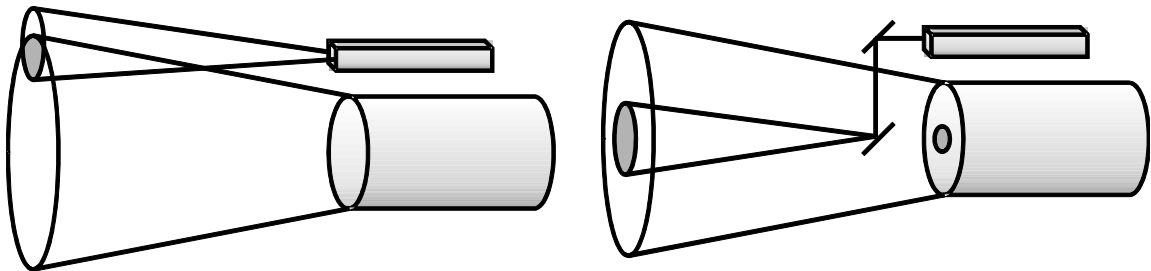


Figure 1-2: On the left is an example of a bi-axial lidar geometry, and on the right is an example of a co-axial lidar geometry.

There are two orientations for the geometry of a lidar: bi-axial, and co-axial, as seen in Figure 1-2. A bi-axial lidar transmits a laser beam parallel to the receiver's field-of-view. The transmitted laser beam from a co-axial lidar originates from the center of the receiver's field-of-view. In a co-axial lidar, full overlap ideally occurs immediately, but realistically, these systems have a central obscuration that extends the full overlap distance (such as a secondary mirror in a reflecting telescope, or a center mirror to merge

the transmitter with the receiver). As shown in figure 1-2, overlap occurs in the shaded region for both geometries.

The scattering and attenuation of the particle media through which the lidar pulse propagates are characterized in terms of the backscatter coefficient, $\beta(R)$, and the round-trip transmission, $T(R)$. Different types, sizes, shapes and compositions of atmospheric particles have different angular scattering characteristics.

A certain percentage of light is backscattered at a scattering angle of 180 degrees so that a lidar can sense it. There are two theories that describe this backscatter, dependent on the ratio of the scatterer to the wavelength. Mie scattering theory is used when the particle size approaches or exceeds the wavelength of the incident light. Rayleigh scattering is used when the particle is much smaller than the wavelength. It should be noted that Mie scattering is less sensitive to changes in the wavelength when compared with Rayleigh scattering. In this dissertation, Mie scattering is assumed for aerosol particles, while molecular scattering is described by Rayleigh scattering theory.

Mie scattering occurs when the particle size is on the order of the wavelength, and can therefore be thought of as the interference between a particle and the light wave. The particle interacts with the incident light over an area twice as large as its physical extent due to the refraction of the light. The simplest case is considered here, with spherical and homogeneous particles, so that each one has the same scattering properties. In this case, the Mie backscatter coefficient, $\beta_{Mie}(R, \lambda)$, depends on the range dependent number density of the scatterer, $N_{Mie}(R)$, and the wavelength dependent particle scattering

cross section, σ_{Mie} , so that

$$\beta_{Mie}(R, \lambda) = N_{Mie}(R) \sigma_{Mie}(\lambda) . \quad (1-4)$$

There are two additional parameters defined within Mie scattering theory: the scattering efficiency, Q_{sc} , and the size parameter, Φ . The ratio of the particle scattering cross section, σ_{Mie} , to the geometrical cross section of the scatterer, $\pi\rho^2$, is defined as the scattering efficiency. The size parameter is the ratio of 2π times the particle radius, ρ , to the wavelength, λ , so that

$$Q_{sc} = \frac{\sigma_{Mie}}{\pi\rho^2} , \quad (1-5)$$

and

$$\Phi = \frac{2\pi\rho}{\lambda} . \quad (1-6)$$

Using equations 1-4 and 1-5, the Mie backscatter coefficient can be rewritten as

$$\beta_{Mie}(R, \lambda) = N_{Mie}(R) Q_{sc} \pi\rho^2 . \quad (1-7)$$

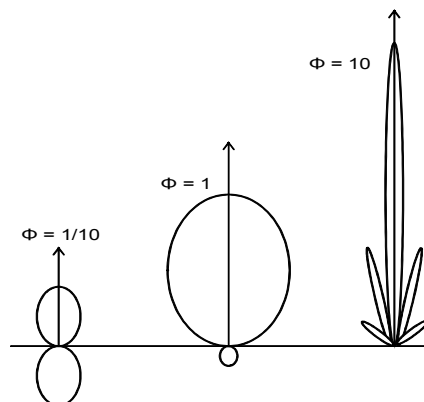


Figure 1-3: The angular distribution of Mie scattering changes with the size parameter, with dramatically more forward scattering for larger size parameters.

The angular distribution of the Mie scattered light depends heavily on the size parameter, with more forward scattering for larger values of Φ , as shown in figure 1-3, where the scattering for the largest size parameter has been scaled down by approximately 10,000 to show the shapes of the angular distributions.

Rayleigh scattering theory describes the scattering of light when it interacts with a particle much smaller than the incident wavelength. Here it is equated with molecular scattering, although very small aerosol particles could also produce Rayleigh scattering. Rayleigh scattering is better understood than Mie scattering, and has a symmetric phase function so the amount of forward scatter is equal to the amount of back-scatter. The Rayleigh backscatter coefficient, $\beta_{\text{Rayleigh}}(R, \lambda)$, depends heavily on wavelength, λ , and on the composition of the atmosphere, so that

$$\beta_{Rayleigh}(R, \lambda) = \frac{8\pi^3 N(R)(m^2-1)^2}{3 N_s^2 \lambda^4} , \quad (1-8)$$

where $N(R)$ is the range dependent number density (number of molecules per unit volume) of the scatterer at the existing temperature and pressure, N_s is the number density of the scatterer at standard temperature and pressure, and m is the real index of refraction.

The total backscatter, used in the lidar equation, is the sum of the Rayleigh and Mie backscatter coefficients:

$$\beta(R, \lambda) = \beta_{Rayleigh}(R, \lambda) + \beta_{Mie}(R, \lambda) \quad (1-9)$$

The round-trip atmospheric transmittance, $T(R, \lambda)$, varies from zero to one. It is a measure of the fraction of light that is lost during the transmission of light to the scatterer and back to the receiver, so that

$$T(R, \lambda) = \exp[-2 \int \alpha(R, \lambda) dR] , \quad (1-10)$$

where $\alpha(R, \lambda)$ is the extinction coefficient, which contains the losses of light as it travels through the atmosphere from scattering and absorption. Similar to the backscatter, the extinction can be defined using the number density of the specific scatterer species,

N_j , and the extinction cross section $\sigma_{j,ext}(\lambda)$, as seen in equation 1-11:

$$\alpha(R, \lambda) = \sum_j N_j(R) \sigma_{j,ext}(\lambda) . \quad (1-11)$$

Using the scattering and extinction relations, the lidar equation can be represented in a better known form:

$$P(R) = P_0 \frac{c\tau}{2} A \eta \frac{O(R)}{R^2} \beta(R, \lambda) \exp\left[-2 \int_0^R \alpha(R, \lambda) dR\right] \quad (1-12)$$

There are two quantities in the lidar equation that cannot be determined except by measurement: the backscatter coefficient, $\beta(R, \lambda)$, and the extinction coefficient, $\alpha(R, \lambda)$. Moreover, the general lidar equation is indeterminate, with more than one unknown for each range, R . This problem is usually solved with assumptions about the extinction-to-backscatter ratio (Kovalev, 2004), or independent measurements of the unknown parameters. Adding complexity, both the backscatter and extinction coefficients have components that are dependent on the Mie or Rayleigh nature of the scatterers.

1.3.3 High Spectral Resolution Lidar

High Spectral Resolution Lidar (HSRL) has proven to be uniquely valuable in profiling atmospheric aerosols, by spectrally separating the Doppler broadened Mie and molecular Rayleigh backscattered signal, allowing a determinate lidar equation. The HSRL technique was first discussed by Schweisow and Lading (1981), and demonstrated by Shipley et. al. (1983), who originally used a Fabry Perot etalon as the narrow band filter. Shimizu, Lee and She (1983) suggested the use of an atomic absorption filter in an HSRL, and She, Alvarez, Caldwell, and Krueger (1992) demonstrated a HSRL using a barium vapor filter to separate the Mie and Rayleigh lidar return. Piironen and Eloranta (1994) used an iodine atomic absorption filter in an HSRL which had the added advantage of having an absorption line that aligned with a Nd:YAG laser wavelength.

HSRL permits range resolved retrievals of the Mie-to-Rayleigh backscatter ratio, which allows the Mie backscatter, extinction, and extinction-to-backscatter ratio to be directly calculated. Basic elastic scatter lidars require assumptions about the Mie extinction-to-backscatter ratio as well as additional atmospheric data in order to acquire the same information. An HSRL takes advantage of the different Doppler broadening of the Mie (aerosol) and Rayleigh (molecular) backscattered signals to eliminate the need to assume a value for the extinction-to-backscatter ratio, which has been shown to be widely varying (Ferrare, 2001, Hair et al., 2008). As seen in Figure 4, an HSRL can use one channel to record signals proportional to the total Mie *and* Rayleigh backscatter (Channel A), while, on a different channel with a narrow band filter (Channel B), simultaneously record signals proportional to either the Mie *or* Rayleigh backscatter (Hair, 1998). Also shown are the signals from each channel when the narrow band filter eliminates the Mie signal from Channel B. A ratio of these two signals is recorded to obtain the Mie-to-Rayleigh backscatter ratio, thereby canceling the overlap function because of the common optics used by the two signals. For this reason, an HSRL can reliably take significant data below the full overlap distance. However, to implement the HSRL technique, HSRL systems must employ extremely narrow spectral filtering. The difference in the Doppler broadening of the Mie and Rayleigh filtering is on the order of several picometers, and it must be precisely and consistently done. The current standard is the iodine absorption filter operating at 532nm (Piironen et al, 1994, Hair, 1998), but there is a need to operate at additional wavelengths to confidently measure the properties

of global aerosols and their changes in time.

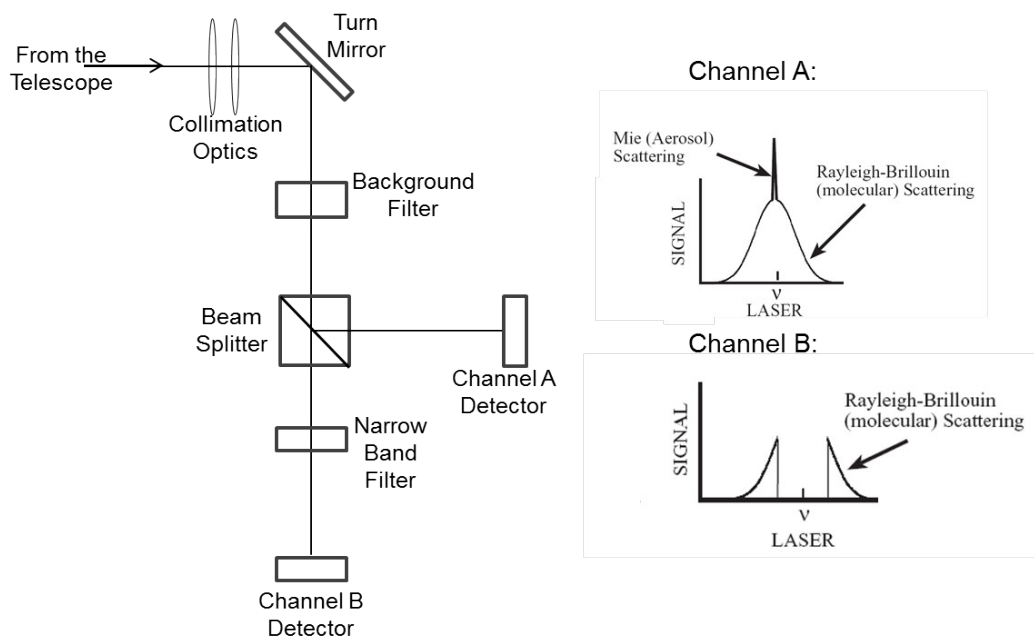


Figure 1-4: On the left is a block diagram of the receiver optics for an HSRL. On the right are the signals on the detectors.

In previous HSRL systems (Shipley et al, 1983, Piironen et al, 1994, Hair, 1998), the narrow band filter blocks the Mie backscattered signal, because it is less affected by the Doppler broadening and because there are reliable models for the line shape of the Rayleigh-Brillouin backscattered signal (Tenti, Boley & Desai, 1974). The laser line position and width must be stable enough to be small compared with the filter width, which is not a problem with the iodine vapor filter, in which only about 30 percent of the Rayleigh backscatter is passed. However, if a more efficient filter with a narrower bandpass could be employed, the laser line width and position would become more critical. Using such a theoretical filter, more of the Rayleigh backscatter could be passed,

allowing for improved system efficiency, as well as the possibility of operating at other wavelengths. Additionally, there is the possibility of using a narrow bandpass filter to pass only the Mie backscattered signal, although this has not yet (to the author's knowledge) been done.

1.3.4 High Spectral Resolution Lidar Equation

When the lidar return can be separated into its Mie and Rayleigh components using HSRL, the lidar equation can also be separated into its Mie and Rayleigh components, as seen in equations 1-13 and 1-14 below.

$$P(R)_{Mie} = P_0 \frac{c\tau}{2} \frac{A\eta_{Mie}}{R^2} \beta_{Mie}(R, \lambda) \exp\left[-2 \int_0^R \alpha(R, \lambda) dR\right] \quad (1-13)$$

$$P(R)_{Rayleigh} = P_0 \frac{c\tau}{2} \frac{A\eta_{Rayleigh}}{R^2} \beta_{Rayleigh}(R, \lambda) \exp\left[-2 \int_0^R \alpha(R, \lambda) dR\right] \quad (1-14)$$

If we allow C_i to contain all of the known parameters so that

$$C_i = P_0 \frac{c\tau}{2} A\eta_i \quad (1-15)$$

where i is either Rayleigh or Mie, then equations 1-13 and 1-14 are reduced to

$$P(R)_{Mie} = \frac{C_{Mie}}{R^2} \beta_{Mie}(R, \lambda) \exp\left[-2 \int_0^R \alpha(R, \lambda) dR\right] \quad (1-16)$$

and

$$P(R)_{Rayleigh} = \frac{C_{Rayleigh}}{R^2} \beta_{Rayleigh}(R, \lambda) \exp\left[-2 \int_0^R \alpha(R, \lambda) dR\right] \quad (1-17)$$

By inverting the equation 1-17 (the Rayleigh lidar equation), a unique value for the range

dependent total extinction coefficient can be found:

$$\alpha(R, \lambda) = -\frac{1}{2} \left(\frac{d}{dr} \ln[R^2 P_{Rayleigh}(R)] - \frac{d}{dr} \ln[\beta_{Rayleigh}(R, \lambda)] \right) . \quad (1-18)$$

The ratio of the Mie to the Rayleigh lidar return is known as the lidar backscatter ratio, $R_\beta(R)$, and can be found from the ratio of equations 1-16 and 1-17:

$$R_\beta(R) = \frac{\beta_{Mie}(R)}{\beta_{Rayleigh}(R)} = \left[\frac{C_{Rayleigh}}{C_{Mie}} \frac{P_{Mie}(R)}{P_{Rayleigh}(R)} \right] . \quad (1-19)$$

Using equation 1-8, the range dependent atmospheric Rayleigh backscatter coefficient,

$\beta_{Rayleigh}(R)$, can be calculated as a function of air density using a measured atmospheric temperature profile (Kovalev 2004). When combined with equation 1-19, the Mie backscatter coefficient can be found:

$$\beta_{Mie}(R) = R_\beta(R) \beta_{Rayleigh}(R) = \left[\frac{C_{Rayleigh}}{C_{Mie}} \frac{P_{Mie}(R)}{P_{Rayleigh}(R)} \right] . \quad (1-20)$$

The Mie backscatter to extinction ratio, $\Pi_{Mie}(R)$, can then be directly solved for, to obtain

$$\Pi_{Mie}(R) \equiv \frac{\beta_{Mie}(R)}{\alpha(R)} = \frac{\beta_{Rayleigh}(R)}{\alpha(R)} \left[\frac{C_{Rayleigh}}{C_{Mie}} \frac{P_{Mie}(R)}{P_{Rayleigh}(R)} \right] . \quad (1-21)$$

This demonstrates how the separation of the Mie and Rayleigh backscattered lidar signal can lead to a determinate lidar equation. This analysis assumes that the Mie and Rayleigh backscattered signals are completely separated by the narrow band filter in an HSRL. However, there may be a remnant of each signal measured in the other channel, so that the measured signals in each channel, $MS(R)_{Rayleigh}$ and $MS(R)_{Mie}$,

are a linear combination of fractions of the Mie and Rayleigh signal multiplied by the lidar's photon efficiency.

$$MS(R)_{Rayleigh} = \gamma [C_{Mr} P(R)_{Mie} + C_{Rr} P(R)_{Rayleigh}] + P_{bg, Rayleigh} \quad (1-22)$$

$$MS(R)_{Mie} = \gamma [C_{Mm} P(R)_{Mie} + C_{Rm} P(R)_{Rayleigh}] + P_{bg, Mie} \quad (1-23)$$

In equations 1-22 and 1-23, γ is the photon efficiency of the lidar, C_{Mr} is the fraction of the Mie scattering in the Rayleigh channel, C_{Rr} is the fraction of the Rayleigh scattering in the Rayleigh channel, C_{Mm} is the fraction of the Mie scattering in the Mie channel, and C_{Rm} is the fraction of Rayleigh scattering in the Mie channel, and $P_{bg, Rayleigh/Mie}$ is the background signal count in each channel. These coefficients are unique to an individual lidar system, and must be known to accuracies on the order of 0.01% (Kovalev 2004).

1.3.5 Filters for Comparison

This research analyzes and compares two different approaches to develop alternative narrow band filters for an HSRL that can operate at other wavelengths besides the 532nm allowed by the iodine vapor absorption filter. The first of these is a spherical Fabry-Perot interferometer (SFPI) that has been designed and built at Montana State University (Hoffman, Repasky, Reagan & Carlsten, 2012), and the second is a wide-angle Michelson interferometer (WAMI) that has been designed and built at the NASA Langley Research Center (LaRC) (Liu, Hostetler, Miller, Cook & Hair, 2012). The researcher had the opportunity to visit both MSU and NASA LaRC, and interact with the hardware for

both HSRL systems. Several weeks were spent at each facility, becoming familiar with the interferometers.

The SFPI at Montana State University (MSU) was built for use in an HSRL operating at 532nm, but has the ability to adjust for a wide potential spectrum (Neal, 2009). A SFPI is a stable resonator originally described by Pierre Connes (1956), and is used in spectroscopic applications ranging from laser diagnostics (Boyd & Gordon, 1961, Bradley & Mitchell, 1968) to high spectral filtering (Hoffman et al, 2012). A SFPI is preferred over a planar Fabry-Perot interferometer (PFPI) in situations where angular insensitivity and high etendue are priorities.

A WAMI has been designed and built for the second generation airborne HSRL at NASA LaRC, operating at 355nm. A WAMI is a Michelson interferometer that has been field-compensated by replacing one arm with a material of higher index (usually glass) and aligning the virtual images of each beam path to allow for a larger acceptance angle. By inducing complementary tilt fringes, and centering the phase on the narrower Mie signal, spectral separation of the Mie and Rayleigh signal is accomplished.

1.4 Methodology

This research employs the capabilities of current software to create a platform whereby a one to one comparison of these interferometers is possible, and to create a design tool for multi-spectral HSRL systems. To do this, the lidar return is modeled using two separate methods: the simple Gaussian lidar return model, and the Bruneau

lidar return model, detailed in the next section. The two interferometric narrow band filters, the SFPI and the WAMI, are modeled using the ray-tracing software packages FRED (from Photon Engineering), and Zemax (from Radiant-Zemax), discussed below. Additional data analysis is completed in Matlab. The modeled lidar return, composed of Mie and Rayleigh back-scattered photons, is used in conjunction with the interferometric filter models to determine the signal on the detector. Using this, a comprehensive comparative analysis of the two interferometers is completed, in which specific comparison criteria are analyzed and contributing factors are discussed. These comparison criteria are the spectral and angular selectivity as well as the efficiency, and are detailed below. A flow diagram of this process is shown in figure 1-5.

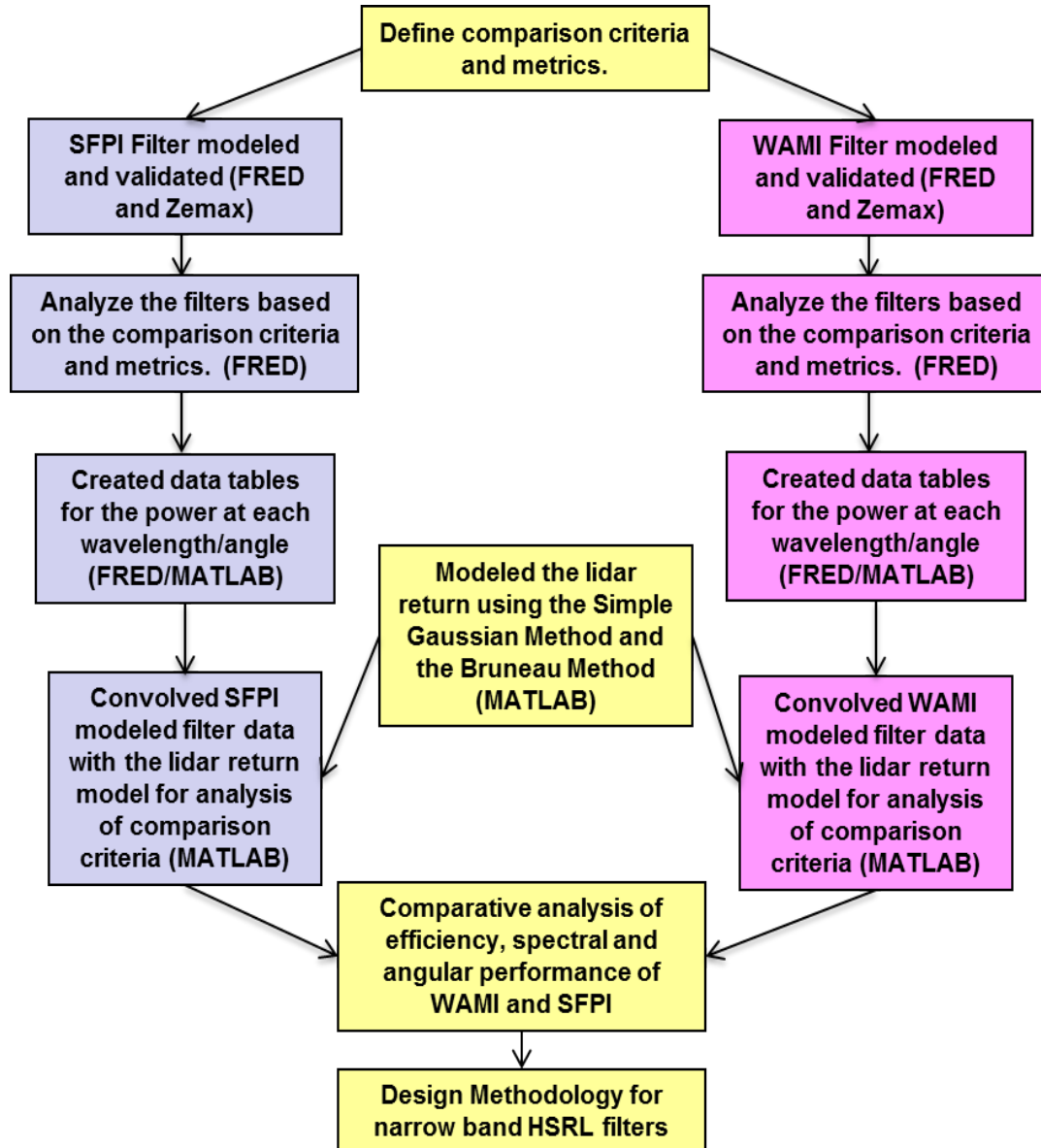


Figure 1-5: Flow diagram showing the analysis steps to arrive at the comparative analysis of the WAMI and SFPI for a narrow band filter in an HSRL.

1.4.1 Software

FRED is a ray tracing software developed to “merge the optical elements with the mechanical components” (Photon Engineering FAQ, 2013), and is generally used for

stray light analysis. The non-sequential mode of FRED was used for this research, meaning that the path the light takes through the system is systematically determined by the software. Ray tracing non-sequentially takes more analytical power because of the unknown paths, but can serve as a virtual prototype. There are some elements of the software that need care, such as definition of the source.

Zemax is a ray tracing software that was developed with strong sequential capabilities, meaning that a user defines the path that a ray will trace through a system. It has an effective multi-variable system optimization tool, as well as a capability for physical optics. Zemax was found to be somewhat limited for the analysis of the spherical FPI in terms of energy conservation, as detailed in Appendix C, so its use is limited to verification and determination of element locations.

1.4.2 Comparison Criteria

Three areas were chosen for comparison based on the requirements outlined by NASA LaRC in their original proposal for the second generation airborne HSRL, using an interferometric filter. These three criteria are the spectral selectivity, the angular selectivity, and the efficiency of the filter.

The spectral response of the interferometer is used in the retrieval of the aerosol extinction and backscatter coefficients. Inaccurate calibration can be the dominant source of error; therefore, the receiver must be locked to the transmission frequency. Both MSU and LaRC has developed innovative locking techniques that compliment the interferometric filters in use. The spectral evaluation of each instrument varies with the

technique, but the resolving power is a common spectral metric that is used to compare the two systems. It's found that both are sufficient, but the confocal cavity can produce a higher resolving power (RP) when necessary, which can be an advantage, as a wide spectral range decreases the contrast of the signal. A higher RP also allows more substantial Rayleigh signal, or "wing."

The acceptance angle determines which interferometer is better suited to certain situations. For example, a large entrance angle is necessary for a space based HSRL, stemming from the need for a large aperture receiver. Additionally, the central wavelength of an interferometric filter will shift to a shorter wavelength if the illuminating light is not perpendicular to the filter. The contrast is also affected by the angle at which the light is incident on the interferometer. The acceptance angle is the maximum angle from the normal at which the interferometer can effectively operate as a filter, and it determines the field of view (FOV) of the filter, which affects the Signal to Noise Ratio (SNR).

The efficiency of the narrow band filter in an HSRL is an important consideration, because the light levels in lidar are generally low enough to justify either photon counting or the averaging of many lidar returns in order to obtain useful data. To evaluate the efficiency of each interferometer, the throughput and the transmission are addressed. The throughput is an invariant system value that can be used for a one-to-one comparison of the geometric extent of the narrow band filters. It is a metric of the energy that a radiometric system can gather. The transmission of the system is a metric of how many

photons reach the detector in a lidar. The transmission is evaluated for each channel of the two interferometers, and is compared on a percentage level. The iodine absorption filter has a transmission rate of approximately 20%, so the potential transmission rates over of 99% that are found for both the SFPI and the WAMI are a significant improvement.

1.5 Modeling the Lidar Return

The range dependent lidar backscattered return is modeled two different ways in order to simulate the atmosphere and verify and test the interferometric models for the narrow band filter.

1.5.1 Simple Gaussian Method for Modeling the Lidar Return

The simple Gaussian model takes into account the fact that the Doppler broadened lidar return for both molecules (Rayleigh) and particulates (Mie) can be assumed to have a Gaussian spectral distribution (Bruneau, 2002). The full-width at half-maximum (FWHM) of the Doppler broadened Rayleigh return is approximately 3GHz, and is under 100 MHz for the Mie return (Liu et al., 2012, She 2001). The FWHM of the Mie backscatter is approximately equal to that of the transmitted laser pulse, in this case, the laser at NASA LaRC. The Rayleigh backscatter is Doppler broadened by several GHz, and varies with temperature and pressure; in this case STP is assumed. Using these assumptions and the general form of a Gaussian, equation 1-24 is used to produce figure 1-6, with i indicating either Mie or Rayleigh returns:

$$G_i(\lambda) = a_i \exp\left[-\frac{(\lambda - b_i)^2}{2d_i^2}\right] \quad (1-24)$$

In this form, a_i is the normalized peak value, b_i is the central wavelength value, and d_i is a value based on the FWHM of the signal so that

$$d_i = \frac{FWHM}{2\sqrt{2 \ln(2)}} \quad (1-25)$$

The sum of the Mie and Rayleigh Gaussian components ($G_R + G_M$) is calculated and scaled so that the peak Rayleigh return is one quarter of the peak Mie return (Bruneau & Pelon, 2003), which is itself normalized to 1. The ratio between the Mie and Rayleigh return is held constant for this simplified model, while in reality the ratio and the FWHM varies with atmospheric conditions and range. Standard temperature and pressure (STP) and a nominal range is assumed for these models. The expected broadening with increased wavelength is also observed (figure 1-7). The code used for this analysis is given in Appendix A.

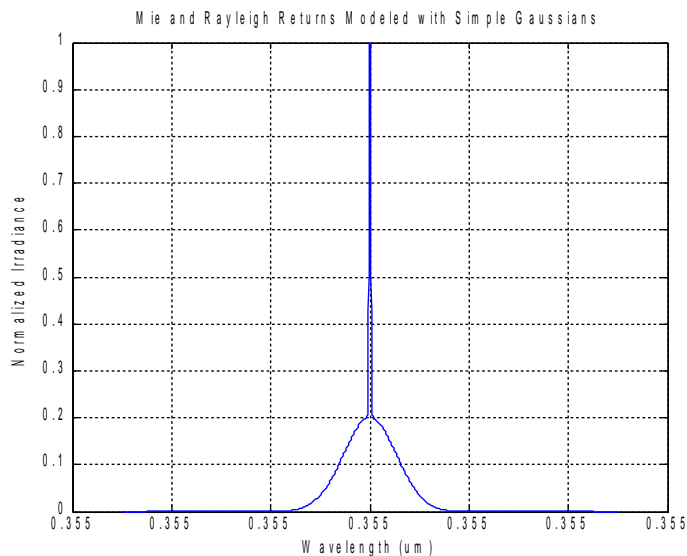


Figure 1-6: The Doppler broadened lidar return incident on the HSRL, modeled using a simple Gaussian.

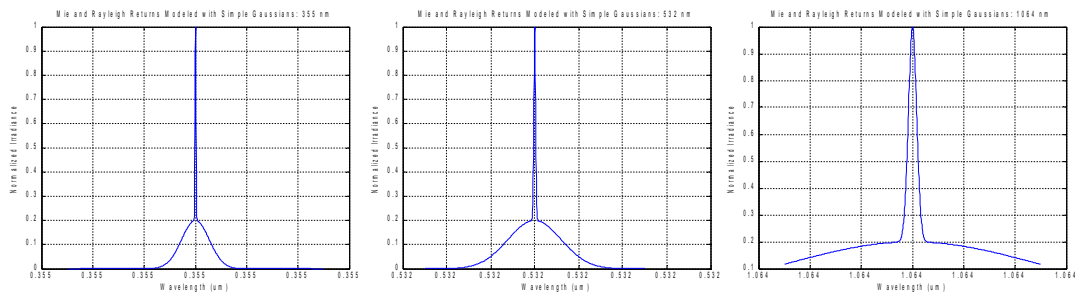


Figure 1-7: The Doppler broadened lidar return modeled using a simple Gaussian, at 355nm, 532nm, and 1064nm, going from left to right. The wavelength range is the same scale for each.

1.5.2 Bruneau Method for Modeling the Lidar Return

Bruneau and Pelon (2003) used a Gaussian based model to produce their version of the Doppler broadened lidar return, but took into account additional atmospheric criteria. A Gaussian distribution is assumed, so that the wave-number dependent

irradiance is

$$I_i(\sigma') = \frac{1}{\gamma_i \sqrt{\pi}} \exp\left[-\frac{(\sigma' - \sigma)^2}{\gamma_i^2}\right], \quad (1-26)$$

Where γ_i is the 1/e half-width (i indicates Mie or Rayleigh), σ' is the wave-number, and σ is the central wave-number ($1/\lambda_0$ where $\lambda_0 = 355\text{nm}$ here). At a temperature of 250 K for a central wavelength of 355nm, the half width of the molecular return, γ_R , is approximately $7.1\text{E-}6\text{m}^{-1}$. The Mie scattering line width ranges between 50 to 100 times smaller than the Rayleigh scattering line width (Bruneau et al, 2003), so this is applied as a scale factor of 75, so that $\gamma_M = 9.47\text{E-}8\text{m}^{-1}$. The total lidar return signal, I_{total} , plotted in figure 1-8, is calculated by linearly combining the Rayleigh return I_R , the Mie return I_M , and the backscatter ratio R_β , so that

$$I_{total} = \frac{1}{R_\beta} I_R + \frac{R_\beta - 1}{R_\beta} I_M, \quad (1-27)$$

where

$$R_\beta = \frac{\beta_M + \beta_R}{\beta_R}. \quad (1-28)$$

Using the Bruneau model, the Doppler broadening increases proportional to the wavelength (figure 1-9), as with the simple Gaussian return model. The code used for this analysis is given in Appendix B.

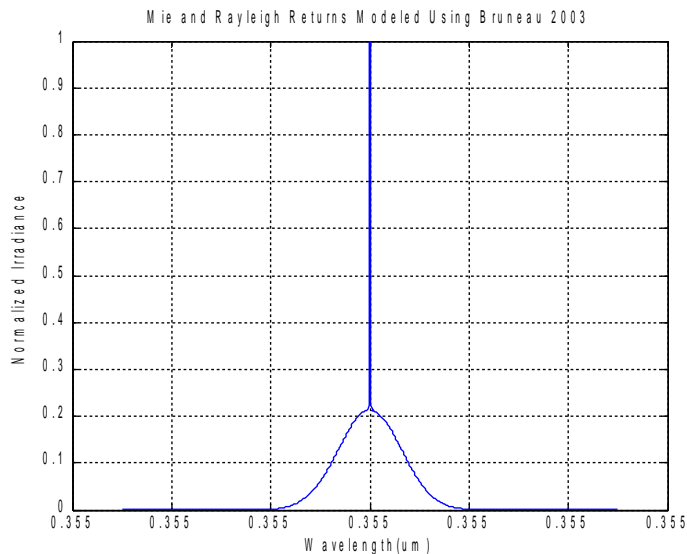


Figure 1-8: The Doppler broadened lidar return incident on the HSRL, modeled using the technique outlined in Bruneau (2003), and a scale factor of 75.

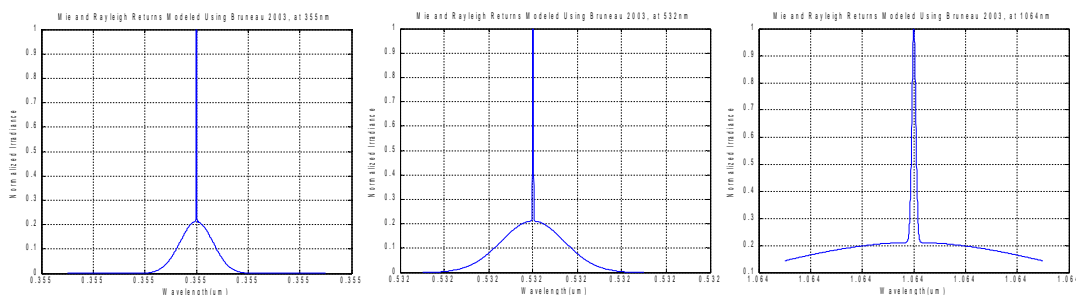


Figure 1-9: The Doppler broadened lidar return modeled using the Bruneau model, at 355nm, 532nm, and 1064nm, going from left to right. The wavelength range is the same scale for each.

1.6 Goals and Contributions

The goal of this dissertation is to develop a generalized methodology for the design and implementation of the narrow band filter necessary for a HSRL. Discussions include the inter-relatedness of the spectral, angular, and transmissive properties of two

interferometers that are currently being used for this purpose.

The research tasks in this work can be broken up into three separate categories. The first and second specific aims are to perform end to end modeling and analysis of 1) the spherical Fabry-Perot interferometer at MSU, and 2) the wide-angle Michelson interferometer at NASA LaRC. The third specific aim is to perform a comprehensive comparative analysis of these two systems for the development of a design methodology.

Novel contributions of this research include:

- (1) A verified non-sequential model of a spherical FPI. This model offers a vehicle for a comprehensive analysis, including diffractive and interferometric effects.
- (2) A verified non-sequential model of a wide-angle Michelson interferometer. This model allows for detailed examination of the diffractive and interferometric effects of the interferometer.
- (3) A discussion of the limitations of Zemax for coherent interferometric ray-tracing.
- (4) An analysis of the spectral requirements and capabilities of each interferometer.
- (5) An analysis of the angular range of each interferometer, including the effect of a range of angular variables.
- (6) An analysis of the efficiency of each interferometer, evaluated using the filter throughput and transmission.

(7) A methodology for the design of a narrow band filter for use in a HSRL.

The following chapters discuss these contributions in more detail. They have been organized by instrument, so that chapter 2 discusses the SFPI in detail, including the modeling process and an analysis of the comparison criteria (spectral, angular, and transmission). Chapter 3 addresses the modeling process of the WAMI, as well as an analysis of the comparison criteria. A comparative analysis of the SFPI and the WAMI are contained in chapter 4, and is used to develop the design methodology for the design of a narrow band filter for use in a HSRL. Chapter 5 closes this dissertation, and offers a brief summary in addition to conclusions drawn from the previous chapters. A table of acronyms can be found in appendix D.

CHAPTER 2:

THE SPHERICAL FABRY-PEROT INTERFEROMETER

2.1 Introduction and Description

A spherical Fabry-Perot interferometer (SFPI) is a stable resonant cavity that is composed of two spherical mirrors separated by a distance approximately equal to their radius of curvature. A ray that enters the SFPI under the proper conditions traverses the cavity four times before repeating the approximate path and intersecting with itself. This intersection produces a multiple beam interference pattern very similar to the ones produced with a planar Fabry-Perot interferometer (Hercher 1968). A high spectral resolving power can be found by precisely controlling the spacing between the mirrors of a SFPI.

This high resolving power is obtained at Montana State University (MSU), where a SFPI has been designed and built for use as a narrow band filter in a HSRL. This has been done as a part of a larger effort to improve our understanding of atmospheric aerosols (Neal 2009, Hoffman 2012). For this research, the SFPI and an appropriate source have been modeled in ray-tracing software, and verified using data obtained by MSU. These models are detailed in this chapter, along with the detailed results of the specular, angular, and transmission/throughput analysis.

A HSRL has been designed and constructed at MSU whose novel feature is the inclusion of a SFPI to spectrally separate the Rayleigh and Mie backscattered signal.

This HSRL joins instrumentation at MSU dedicated to studying the direct and indirect effects of aerosol radiative forcing. This instrumentation includes a two-color lidar to provide information on the aerosol composition based on a constrained ratio aerosol model (CRAM) (Cattrall, Reagan, Thome, Dubovik, 2005), a water vapor differential absorption Lidar (DIAL) that will provide range-resolved measurements of water vapor density, a scanning solar radiometer that will provide information on the aerosol size distribution and radiative forcing, a ground-based nephelometer to measure the scattering component of the aerosol extinction (Repasky 2011, Nehrir 2011), and the aforementioned HSRL, to provide range-resolved values for the aerosol backscatter coefficient, extinction coefficient, and the lidar ratio.

This HSRL transmits the fundamental and second harmonic output from an injection seeded Nd:YAG laser, and collects the backscattered return using a Schmidt-Cassegrain telescope, as shown in figure 2-1. In the receiver, the 532nm return is optically separated from the 1064nm return with a beam splitter (BS1). The 1064 return is then directed through a filter and onto an avalanche photodiode. The 532nm return is transmitted through BS1 and is then coupled into a multi-mode optical fiber. The fiber output is coupled at BC1 with a modulated 1064nm beam that locks the SFPI to the transmitted frequency. This combined beam is incident on a polarizing beam splitter (Pol-2), where the light rejected from the polarizer is transmitted through an optical filter centered at 532nm and is incident on PMT-1. This is used to monitor the total backscatter at 532nm. The light that is transmitted through Pol-2 is focused onto the center of the

SFPI using a 150mm focal length lens (L1). The light that is reflected from the SFPI is then monitored with PMT-2, and the light that is transmitted through the SFPI is monitored with PMT-3 (Hoffman et al. 2012).

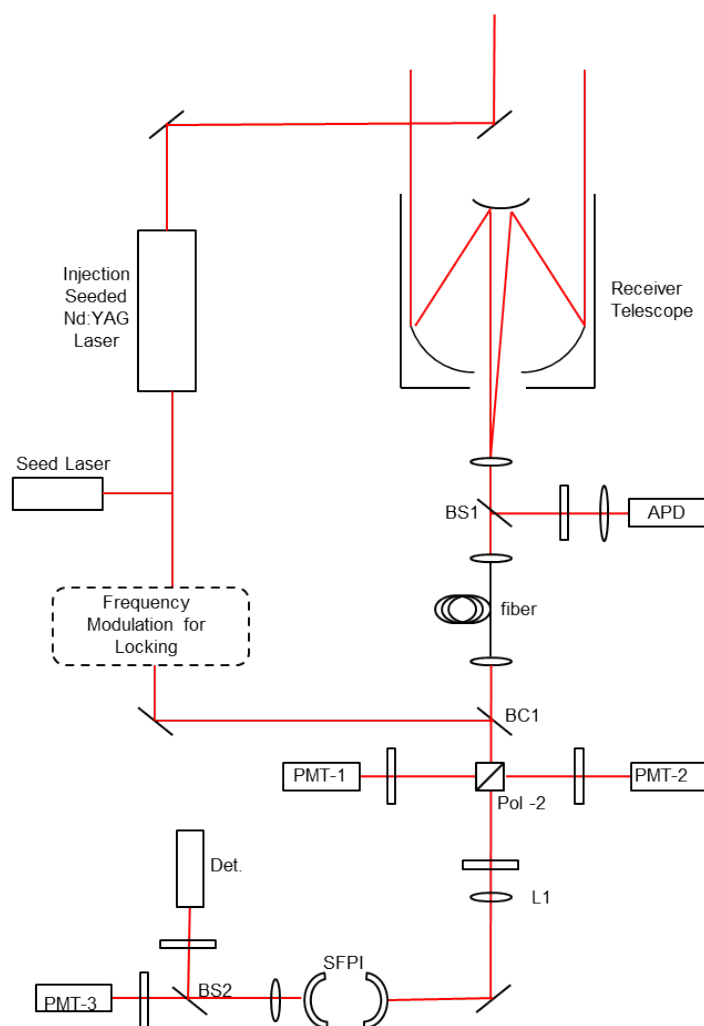


Figure 2-1: Diagram of the HSRL at MSU (Hoffman et al. 2012).

The SFPI has been designed to spectrally separate the Mie and Rayleigh backscattered signals in a HSRL, as described above. It is composed of two identical spherical mirrors with a confocal configuration, so that the vertex of each mirror is

located at the center of the others' radius of curvature. The mirrors are housed in a custom assembly that allows for real time spatial adjustments and alignment (Hoffman et al. 2012, Neal 2009). The resonant condition of the SFPI requires that the cavity spacing be an integer number of half wavelengths, so because the cavity is designed for 1064nm, it is also resonant at the doubled (tripled) wavelength of 532 nm (355 nm). In this HSRL design, only the primary and doubled frequencies are used. The mirrors are made of fused silica, and have a radius of curvature of 1 cm. The inner surfaces have high reflectivity coatings of 94% for the 532nm wavelength, and 99% for the 1064nm wavelength, and the other glass surfaces have an anti-reflection coating. Because the narrower Mie signal is locked and centered on a cavity resonance, the SFPI acts as a narrow band-pass filter, and the Mie signal will be transmitted while the broader Rayleigh signal will be reflected from the cavity.

2.2 Modeling of the SFPI

The SFPI is modeled using ray-tracing software (FRED and Zemax), and the analysis of the comparison criteria is completed using MatLab.

The resolving power of the SFPI is dependent on its interferometric effects, and non-sequential coherent ray-tracing was necessary to accurately reproduce these effects for this analysis. Both the FRED and Zemax software have non-sequential capabilities and were used. A planar Fabry-Perot interferometer was originally modeled in both software packages for verification, and it was found that Zemax could not model the

necessary coherence. This process is detailed in the following section. FRED could model the necessary coherence, and was therefore used for the majority of the SFPI analysis. The beam incident on the SFPI is also modeled in FRED.

2.2.1 Coherent Ray Tracing in Zemax

The analysis of a coherent source in Zemax becomes problematic when energy conservation is considered. Issues arise via the “Normalize Coherent Power” switch, which is applied to each detector. In order to demonstrate these issues, a plane parallel plate (PPP) interferometer is modeled in the non-sequential (NSC) Zemax mode.

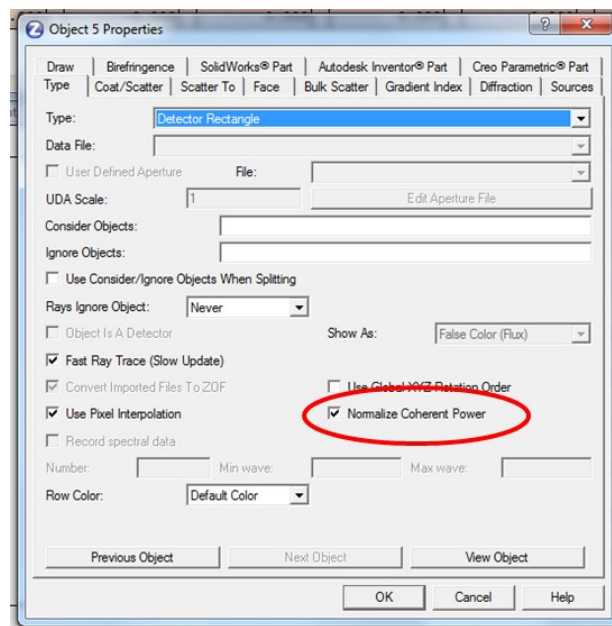


Figure 2-2: Properties for a Detector Rectangle in the NSC Zemax mode. Note the circled "Normalize Coherent Power" switch.

The option to “Normalize Coherent Power” exists for each detector, as shown in figure 2-2. If this switch is turned *on*, then the coherent power is normalized according to the incoherent power incident on the detector. The Zemax Users' Manual advises users

that this option should be used if all of the incoherent power is incident on a single detector. In this situation, the coherent irradiance is computed from the ray data by “squaring and summing the real and imaginary parts of the amplitude pixel by pixel, and then re-normalizing the total coherent irradiance for the entire detector to be equal to the incoherent irradiance incident upon the detector (Zemax 2013).” In a situation where power is split between multiple detectors, it is advised that this option be turned off. This allows the coherent irradiance to be computed for each pixel, which means that the value of the coherent irradiance varies between zero and the incoherent irradiance. However, “it is unknowable where energy lost in this computation would have propagated to (Zemax 2013).”

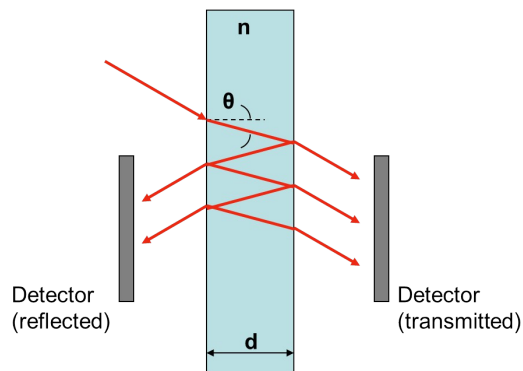


Figure 2-3: The PPP, as modeled in Zemax.

In order to properly analyze a PPP, the energy must be split between two detectors to monitor the transmitted and the reflected energy. According to the Zemax manual, the coherent power should not be normalized for this analysis. A PPP, as shown in figure 2-3, produces constructive interference when

$$m\lambda = 2nd \cos(\theta) \quad , \quad (2-1)$$

and deconstructive interference occurs when

$$\left(m + \frac{1}{2}\right) \lambda = 2nd \cos(\theta) \quad . \quad (2-2)$$

Symbol	Quantity	Value in Model
λ	Wavelength	variable
m	Integer	50
n	Index of refraction	1.5168 (N-BK7)
d	Physical thickness of plate	11.0992 um
θ	Incident angle	20 degrees

Table 2-1: Specifications for the modeled plane parallel plate.

A PPP is modeled using the specifications in table 2-1. In this model, one million rays are traced from an circular source with a radius of 0.2mm and 1Watt of power. The rays are collimated and linearly polarized in the x-direction. The glass used for the PPP model is uncoated N-BK7, so there is a standard 4% reflectance. It is designed using equation 2-1 to produce constructive interference in transmittance. Each detector is 0.4mm in radius, and has 100x100 pixels. For this analysis, the wavelength is scanned between 0.5 to 0.7 microns using 2.5nm steps, with the coherent irradiance on the detector measured at each wavelength. The PPP was designed for a HeNe source at $\lambda = 632.8 \text{ nm}$, which was used to calculate the free spectral range (FSR) for verification:

$$FSR = \frac{\lambda^2}{2nd \cos(\theta)} \quad (2-3)$$

The FSR calculated using equation 2-3 is compared with the results shown in figure 2-4. The peaks found using the ray-tracing software precisely match the theoretical value of $FSR = 0.012$ microns at the peaks ranging from $\lambda = 0.629$ to 0.641 microns, and the dependence of the FSR on the wavelength is apparent. However, there is no conservation of energy. The sum of the energy (the red fringe), closely follows the transmitted energy (green fringe), especially at the lower power values. This is a result of how the coherent irradiance is calculated when the “Normalize Coherent Power” switch is off. At the lower points on the reflected power curve (blue), the power is approximately zero. Because Zemax cannot account for the energy in deconstructive interference, this power is lost instead of being incorporated into the constructive interference. The power sum never reaches 1 watt, and energy is not conserved (absorption is ignored in this analysis).

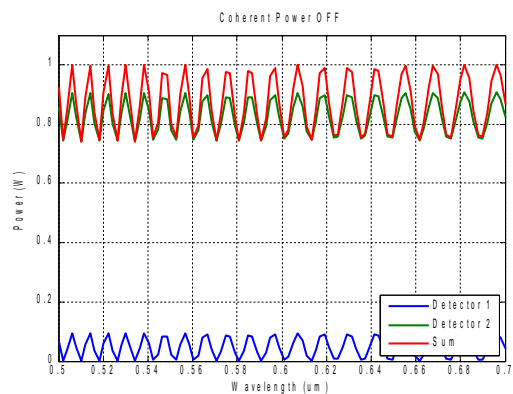


Figure 2-4: Analysis of a plane parallel plate with the “Normalize Coherent Power” switched off.

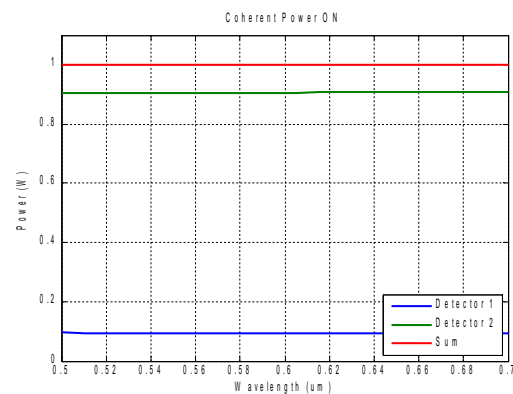


Figure 2-5: Analysis of a PFPI with the “Normalize Coherent Power” switched on.

The result of the same analysis with the “Normalize Coherent Power” switched *on* is shown in figure 2-5. In this case, the coherent power is normalized according to the incoherent power incident on the detector, and because the sum of the energy is constant (1W) across the spectral range, it's apparent that energy is conserved. However, there is none of the expected interference.

From this comparison, it can be concluded that using Zemax as the primary analysis tool for a PPP, and by extension, a SFPI, will be problematic. The expected interferometric interference can be observed, but energy conservation will not be maintained. Additionally, Zemax cannot perform a polychromatic interferometric analysis (Zemax 2013). The analysis of the SFPI at MSU should accurately reflect the interferometric effects as well as the power on each detector, so Zemax is not the primary analysis tool.

2.2.2 SFPI Modeling in FRED

FRED is used for the majority of the SFPI modeling and analysis. To show the capabilities of the FRED software, the PPP previously described in table 2-1 is modeled, and the result is shown in figure 2-6. The presence of the fringes shows that the interferometric effects are adequately modeled. Because one watt is incident on the PPP, and the sum of the transmitted and reflected power is constant at one watt, it can be concluded that energy is conserved in this model. Including the phase shift upon reflection is an important element in ensuring that energy conservation is observed in this FRED model.

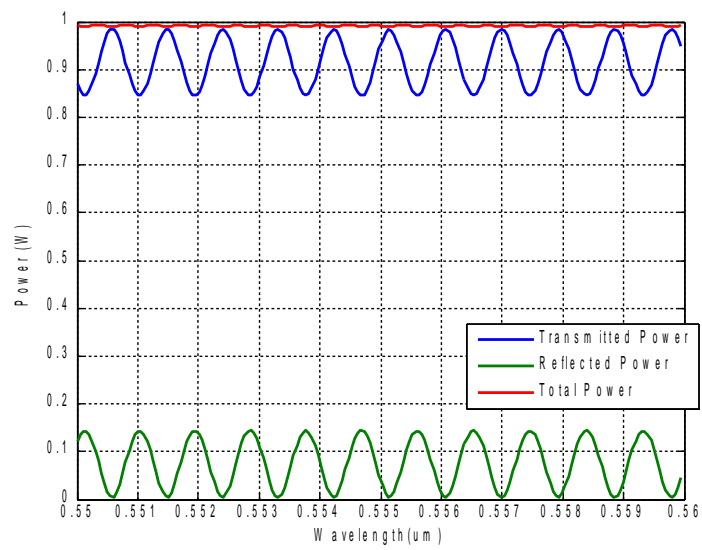


Figure 2-6: The transmitted and reflected power from a PPP, exhibiting the ability of FRED software to model both the interferometric effects and conservation of energy over a range of wavelengths.

The SFPI is fully modeled using FRED software. For this analysis, a 150mm focal length lens is used to focus the collimated source beam onto the center of the SFPI, as shown in figure 2-7 (Neal 2009, Vaughan 1989). The collimated source that is incident on L1 (the 150mm focal length lens) is carefully specified, as discussed in the following section.



Figure 2-7: FRED model of SFPI with source focusing in the center of the cavity.

The SFPI is modeled using a fused silica glass, with user-specified coatings. The reflective coating was set to reflect 94% of the incident light for a 532nm wavelength, with a 90 degree phase shift upon reflection. The other surfaces had an anti-reflection coating. Absorption and scattering were not taken into account in the software.

2.2.3 Source Description

The FRED software models coherent sources using a superposition of Gaussian “beamlets” that take into account the beam's waist and divergence. If these beamlets diverge too far from their primary beam, coherent ray errors occur.

Coherent ray errors are caused by the general structure of coherent ray tracing in FRED. Coherent sources are modeled using an array of beams: a primary beam and secondary beamlets that maintain the divergence and waist of the primary beam, as illustrated by figure 2-8 (FRED Application Note, 2013). The secondary beamlets travel to each surface on which the primary beam is incident, regardless of any physical barriers. This can cause errors when the beamlets are no longer well-correlated with their primary beam.

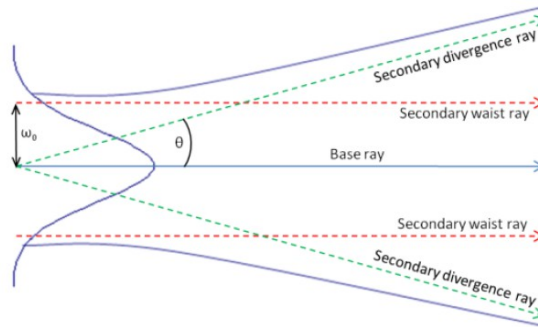


Figure 2-8: The coherent ray structure in FRED. The secondary beamlets keep track of the divergence and the waist of the primary, or base, ray. From the FRED Application Note, "Modeling Coherence" (2013).

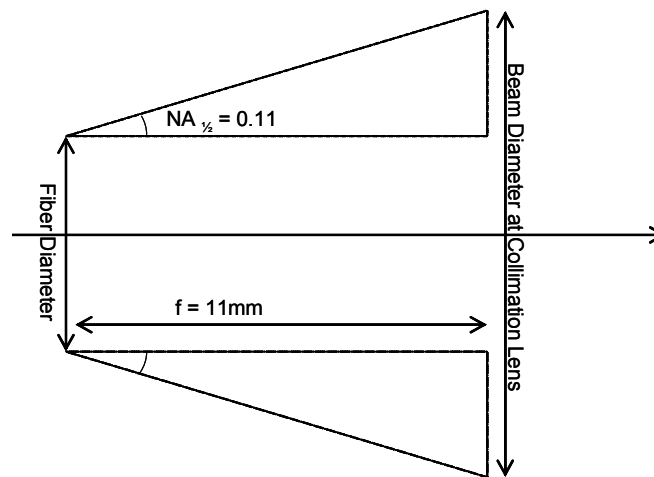


Figure 2-9. Fiber Coupling Lens and Beam Size.

Initially, for the SFPI, the fiber coupling to a collimation lens was modeled in FRED, but the diverging beamlets consistently produced coherent ray errors. To eliminate this source of error, the model was started after the collimation lens, which allowed the coherent beamlets associated with the source to maintain a sufficient distance from their primary beams throughout the analysis. These coherent ray errors are

discussed in additional detail in the angular analysis.

The optical fiber has a diameter of 200 microns, and a numerical aperture of 0.22 radians. A Thorlabs fiber collimator, with a focal length of 11mm, is used on both ends of the fiber. Taking these dimensions into account, the beam diameter at the collimation lens will be 2.629mm, as shown in figure 2-9. Using the FRED standard that the beam diameter is approximately π times the beam waist, and the assumption that this is a multi-mode beam (Hoffman et al. 2012), the beam waist radius is modeled to be 1.314 mm at the collimation lens. Therefore the beam incident on L1 is also 1.314mm, before being focused onto the center of the SFPI. Additionally, this source has a Gaussian power apodization, and is collimated and coherent.

2.3 SFPI Analysis

The spectral analysis of the SFPI is focused on the finesse of this cavity. The two relevant types of finesse are discussed, and a comparison with the experimental results at MSU is shown.

2.3.1 Spectral Analysis: Finesse in the SFPI

Finesse, F , is a measure of the “sharpness” of a fringe, and is a ratio of the width of the fringe at full-width half-maximum (FWHM) and the spacing between resonances in the cavity, commonly called the Free Spectral Range (FSR). Generally a higher finesse allows for more precise spectral selection.

$$F = \frac{FSR}{FWHM} \quad (2-4)$$

There are several different factors that contribute to finesse in a SFPI; the two most significant being the reflectivity of the mirrors' surfaces and the spherical aberration from the mirrors' curvature. The finesse values from each of these sources are added in quadrature to find the total finesse (Neal 2009), so that

$$\frac{1}{F_{total}^2} = \frac{1}{F_{refl}^2} + \frac{1}{F_{SA}^2} \quad (2-5)$$

2.3.1.1 Finesse from Reflectivity

In a precisely confocal cavity illuminated by a single, off-axis, monochromatic point source, for each entrant ray, there are four emergent rays, as seen in figure 2-10, so that 50% of the initial energy is transmitted (B+D), and 50% is reflected from the cavity (A+C).

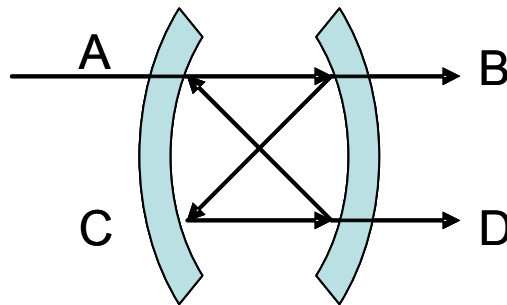


Figure 2-10. For each entrant ray A, there are four emergent rays, at A, B, C and D.

If the cavity mirrors are loss-less with a high reflectivity, the maximum intensity at each point of emergence is approximately equal, and is less than a quarter of the initial intensity. Additionally, the full width at half maximum (FWHM) of the emergent

intensity is given by equation 2-6 below, where L is the cavity spacing (and the radius of curvature), and r is the reflectivity of the mirrors (Johnson 1968).

$$FWHM = \frac{c}{4L} \frac{(1-r^2)}{\pi r} \quad (2-6)$$

The FWHM is the product of the Free Spectral Range (FSR) and the inverse of the finesse. It should be noted that the finesse used here, shown in equation 2-7, is generally used for a confocal cavity (Vaughan 1989, Hercher 1968).

$$F = \frac{\pi r}{(1-r^2)} \quad (2-7)$$

To portray these properties of the SFPI using FRED, an off-axis single-mode source is used, and figure 2-11 shows the transmitted power plotted with respect to the

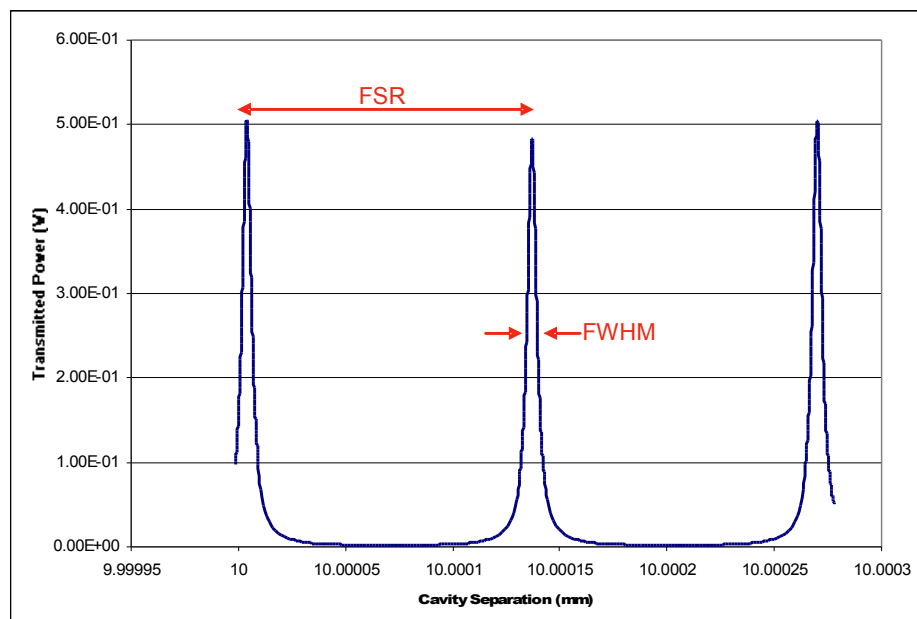


Figure 2-11. The transmitted power versus the cavity separation for a confocal cavity with an off-axis, single-mode source. The finesse of these fringes is 25.

cavity length. The cavity mirrors have a reflectivity of 94% at 532nm, and the finesse of this system matches the expected value of 25.

However, if ideal illumination is incident on the same confocal cavity, a different result can be obtained. In this case, “ideal illumination” is axially symmetric, and is a form of mode matching. The FWHM of the emergent intensity from a cavity with this type of illumination is shown in equation 2-8 (Johnson 1968).

$$FWHM = \frac{c}{2L} \frac{(1-r)}{\pi \sqrt{r}} \quad (2-8)$$

Again, the FWHM is a product of the FSR and the finesse, but the differences between equation 2-7 and equation 2-9, which stem from the illumination and mode-matching (Hoffman et al. 2012), should be noted. In equation 2-9, the frequency of the resonances (FSR) has been doubled, and the square-root of the reflectivity value has been taken in the finesse. The value for the finesse is the same as that found in plane parallel Fabry-Perot interferometers (Johnson 1968, Vaughan 1989):

$$F = \frac{\pi \sqrt{r}}{(1-r)} \quad (2-9)$$

With the same cavity that was previously modeled, an on-axis, single-mode source was used. With a 94% reflectivity, this cavity should have a finesse of 50 according to equation 2-9, which was confirmed in the FRED model. Figure 2-12 shows the transmitted power plotted as a function of the cavity separation (which has the same scale as figure 2-11).

It should be noted that while the finesse has doubled as a result of ideal

illumination, the resolving power (in the form of the FWHM of each fringe) does not change. The power of two is from a change in the free spectral range, and is due to the optical path length traveled by each ray through the cavity.

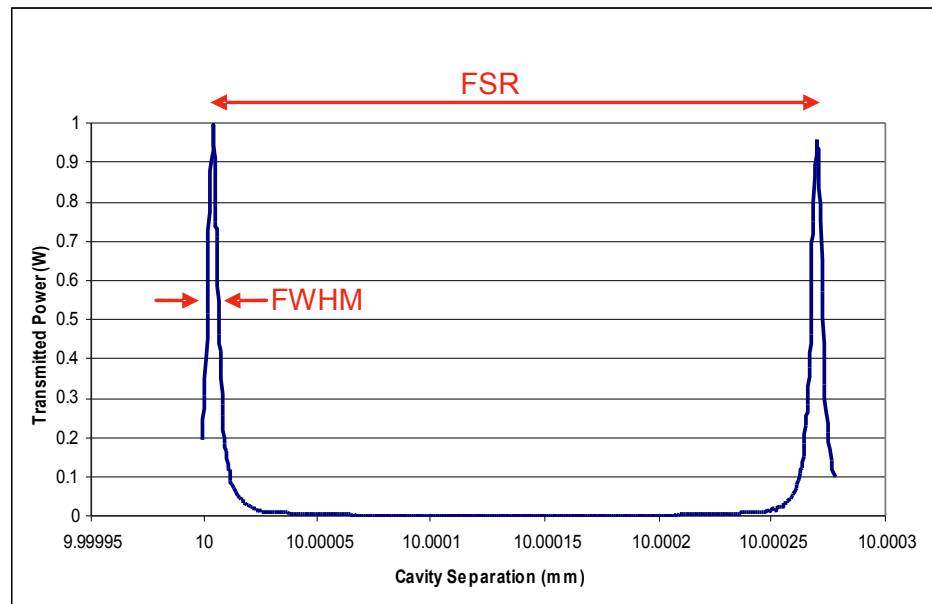


Figure 2-12. The transmitted power versus the cavity separation for a confocal cavity with an on-axis, single-mode source. The finesse of these fringes is 50.

The adjacent resonances in a cavity with ideal illumination are not equally intense, with the result that even resonances are discriminated against, odd resonances are enhanced, and transmissions up to 100% are possible (Johnson 1968), as seen in figure 2-12. This is consistent with results from the FRED models where, unless otherwise mentioned, a single mode source is modeled.

When an on-axis, multi-mode source is included in the FRED model, there are obvious changes in the transmission fringes. In a confocal cavity, with a multi-mode

source, there is a defined relationship between the modes and the peaks, so that the resonant condition occurs only for integer values of $4L/\lambda$, which affects the modes as shown (Boyd & Gordon 1961):

$$\frac{4L}{\lambda} = 2q + (1 + m + n), \quad (2-10)$$

where L is the cavity separation (equal to the radius of curvature of the mirrors in a confocal system), q is the transverse mode, and m and n are the longitudinal modes, so that if $4L/\lambda$ is even, $m+n$ must be odd, and vice versa. In the cavity in use at MSU, the cavity spacing is set to 10.000004 mm with a 532nm source, making the integer even so that $m+n$ must be odd to fulfill the resonance condition. The fringes for an odd sum are shown in figure 2-13, where the central fringe is resonant. In figure 2-14, the fringes for an even sum are shown, where the central fringe is not resonant.

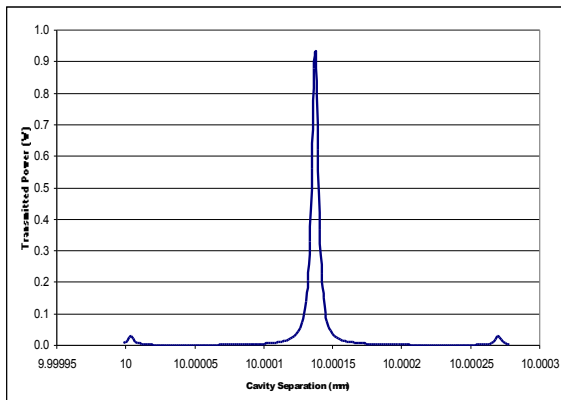


Figure 2-13: The transmitted power versus the cavity separation for an on-axis source with mode 1,0.

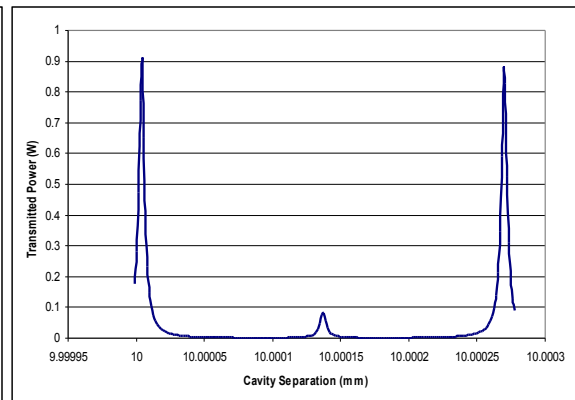


Figure 2-14: The transmitted power versus the cavity separation for an on-axis source with mode 1,1.

In the case of a single-mode source (Vaughan 1989), m and n are zero, and the resonance condition becomes

$$\frac{2L}{\lambda} = q + \frac{1}{2} \quad (2-11)$$

and the separation between resonances, or FSR, is defined by the wavelength so that

$$\Delta L = \frac{\lambda}{2} \quad (2-12)$$

and

$$\Delta q = 1 \quad (2-13)$$

Given that the reflectivity finesse dominates the total finesse for smaller incident angles, as discussed in the next section, a range of reflectivity values are examined for a specific SA finesse in order to determine the accuracy of the FRED models. The total finesse is calculated using equation 2-9 because the SFPI is illuminated with “ideal” illumination. This theoretical finesse is then compared with the modeled value. The modeled and theoretical values for each reflectivity value are shown in table 2-2, and plotted in figure 2-15. The theoretical finesse from spherical aberration (SA) and from reflectivity (Refl) combine, as discussed in the following section, to calculate the total theoretical finesse. The percent error for each reflectivity value is below 1%, so there is cause for confidence in the FRED models. Additionally, the reflectivity finesse changes exponentially with higher reflective coatings, making it a critical factor for the spectral performance of a SFPI.

Reflectivity	Modeled Finesse	Theoretical SA Finesse	Theoretical Refl. Finesse	Theoretical Finesse	Percent Error
0.7	8.71	396216.17	8.76	8.76	0.59
0.8	13.92	591436.38	14.05	14.05	0.92
0.9	29.76	842103.76	29.8	29.8	0.15
0.94	50.59	959448.43	50.76	50.76	0.34
0.97	102.32	1054273.48	103.14	103.14	0.79
0.99	313.49	1120840.10	312.58	312.58	0.29

Table 2-2: Finesse comparison for a range of reflectivity values, and an incident angle of 0.2 degrees at 1E-3mm above the optical axis.

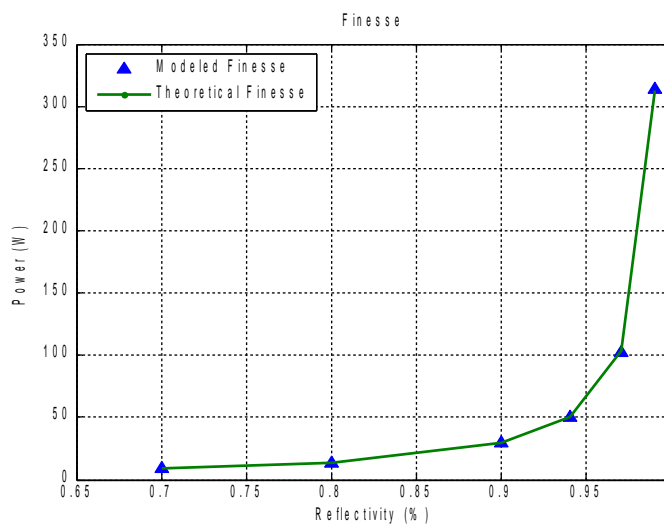


Figure 2-15: A comparison of the modeled and theoretical finesse for a range of reflectivity values.

2.3.1.2 Finesse from Spherical Aberration

The contribution from spherical aberration to the total finesse in a SFPI originates from the difference between the paraxial optical path length and the aberrated optical path length.

Paraxially, the trajectory of an incident beam on a precisely confocal cavity closes after it transits the cavity four times (Johnson 1968, Vaughan 1989, Neal 2009) (following the path ABCDA) as illustrated in figure 2-16a. In this case, the optical path length, L , is equal to four times the cavity length, which is equal to the radius of curvature for a confocal cavity, so that $L=4 R.O.C.$.

When the fourth order spherical aberration is taken into account, the beam trajectory does not close after four passes through the cavity. The optical path length exceeds the paraxial path by Δ , as defined by (Hercher 1968)

$$\Delta = \frac{\rho_1^2 \rho_2^2 \cos(2\theta_0)}{ROC^3} + \text{higher order terms} , \quad (2-14)$$

where θ_0 is the skew angle of the incident ray, ROC is the radius of curvature of the mirror, and ρ_1 and ρ_2 are the height at which the ray strikes the first and second mirrors (the distance from the optical axis), respectively. Additionally the rays no longer follow the original trajectory (figure 2-16a), but instead follow the deviated trajectory shown in figure 2-16b. The higher order terms do not measurably affect the SFPI, so they are ignored.

The fiber aperture and the lens system define the numerical aperture and the $f/\#$ of the beam focusing into the cavity. The SA introduced by the cavity depends strongly on the NA, and therefore on ρ_1 and ρ_2 , which are approximately equal due to the cavity symmetry.

A secondary effect that may influence the finesse is the variation in angle of the

light incident on the lens. This angle θ_i , shown in figure 2-21, acts as the FOV as the fiber has a finite diameter. However, this angle is small and the subsequent off-axis aberrations will also be small. Thus the variation of θ is not a significant contributor to the finesse, and SA would be uniform over the FOV as defined by θ .

For the reasons outlined above, ρ is allowed to equal ρ_1 and ρ_2 , and equation 2-14 is rewritten as

$$\Delta = \frac{\rho^4}{ROC^3} + \text{higher order terms} \quad , \quad (2-15)$$

where ρ is the distance of the beam from the optical axis in the cavity center.

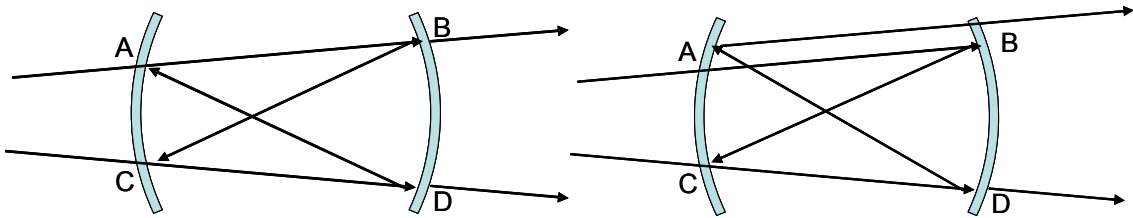


Figure 2-16a. In a paraxial cavity, an incident beam would traverse the path length four times before closing its trajectory.

Figure 2-16b. In a cavity that takes spherical aberration into account, the trajectory does not close, and after four transits, the path length deviates from paraxial by an amount described in equation 2-14.

Taking into account the deviation from spherical aberration, the optical path length through the precisely confocal SFPI becomes $4ROC + \Delta$, or

$$L = 4L + \frac{\rho^4}{ROC^3} \quad . \quad (2-16)$$

The finesse from spherical aberration can then be derived (Neal 2009) to be

$$F_{SA} = \frac{\lambda/2}{(\rho^4) / 4 ROC^3} \quad (2-17)$$

When added in quadrature with the finesse from reflectivity in equation 2-9 (assuming ideal illumination), the total finesse is:

$$F_{total} = \left[\left(\frac{1-r}{\pi \sqrt{r}} \right)^2 + \left(\frac{\rho^4}{2\lambda ROC^3} \right)^2 \right]^{-1/2} \quad (2-18)$$

However, using the finesse from reflectivity in equation 2-7, which is better suited for confocal cavities, the total finesse is:

$$F_{total} = \left[\left(\frac{1-r^2}{\pi r} \right)^2 + \left(\frac{\rho^4}{2\lambda ROC^3} \right)^2 \right]^{-1/2} \quad (2-19)$$

The effect of ρ_1 on the three finesse values (reflectivity, spherical aberration, and the total finesse), is plotted in figure 2-17, where equation 2-19 is used for the total finesse and ρ_1 is assumed equal to ρ . It is apparent that for heights smaller than 0.25 mm incident on the lens, there is minimal impact on the total finesse from the SA finesse. As the finesse from SA becomes more significant, the total finesse is eventually dominated by the contribution from the SA finesse. These values are for a SFPI with a 1 cm radius of curvature and a reflectivity coating of 94% at 532nm, where the beam is focused into the cavity center by a 150mm focal length lens (these are the MSU SFPI specifications). The derived finesse values were verified using the SFPI models.

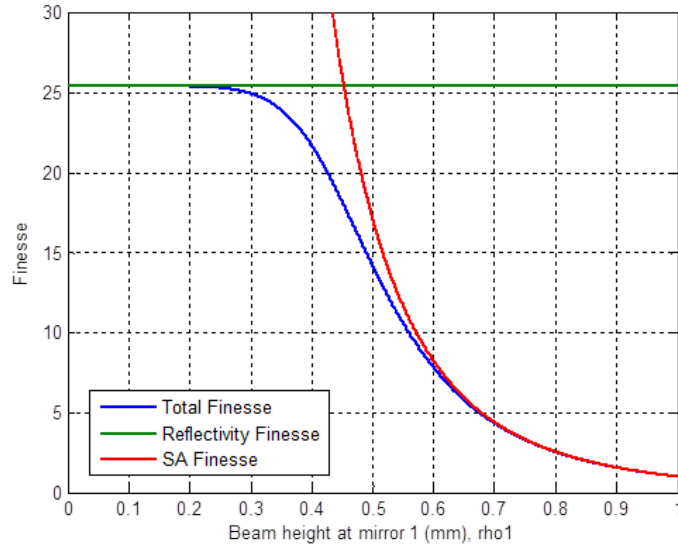


Figure 2-17: The effect of the beam height at mirror 1 on the reflectivity finesse, spherical aberration finesse, and the total finesse for the MSU SFPI.

To eliminate the effect the SA finesse, the beam height can be decreased, but a small beam radius can degrade the signal past the point of usefulness, so a balance is generally reached. This balance is discussed in further detail in the throughput section, but is generally accepted to allow 70% of the original resolving power.

2.3.1.3 Resolving Power in a SFPI

The resolving power (RP) is often referred to as the resolution, and is a metric of the filtering ability of an instrument. The universal definition for RP is the ratio between the incident wavelength λ (or frequency, ν), and the minimum spectral width

$\Delta\lambda$ ($\Delta\nu$):

$$RP = \frac{\lambda}{\Delta\lambda} = \frac{\nu}{\Delta\nu} \quad (2-20)$$

To find the RP for a SFPI, an assumption is made that the minimum spectral

width, $\Delta \nu$, is the spectral width for a monochromatic line in the instrument, so that

$$\Delta \nu = FWHM = \frac{c}{4 ROC} \frac{(1-r^2)}{\pi r} . \quad (2-21)$$

It's been established that the finesse for a SFPI is

$$F = \frac{FSR}{FWHM} = \frac{\pi r}{1-r^2} , \quad (2-22)$$

and when equations 2-20 and 2-21 are combined, it's found that

$$RP_{SFPI} = \frac{4 ROC \pi r \nu}{c(1-r^2)} . \quad (2-23)$$

By using the definition for finesse, and substituting wavelength for frequency

($\lambda=c/\nu$), the simplified RP for a SFPI is found to be (Hercher 1968)

$$RP_{SFPI} = \frac{4 ROC F}{\lambda} , \quad (2-24)$$

where ROC is the radius of curvature, F is the finesse, and λ is the design wavelength.

The finesse in the SFPI at MSU was found to be 313.49, for a radius of curvature of 10mm and a wavelength of 532nm, so the RP for the SFPI as built is 2.35E7.

2.3.1.4 Spectral Comparison of FRED model to MSU Experiment

The resonances occur at intervals of half wavelengths, so the 532nm fringes should occur twice as often as the fringes for 1064nm. To verify this aspect of the FRED model, the cavity separation was set at 10mm, and then scanned through a distance of 1 micron using both wavelengths. This was done both in FRED, and using the SFPI at MSU (Hoffman et al. 2012). The result of this scan using the FRED model is shown in

figure 2-18, and the experimental result from MSU is shown in figure 2-19.

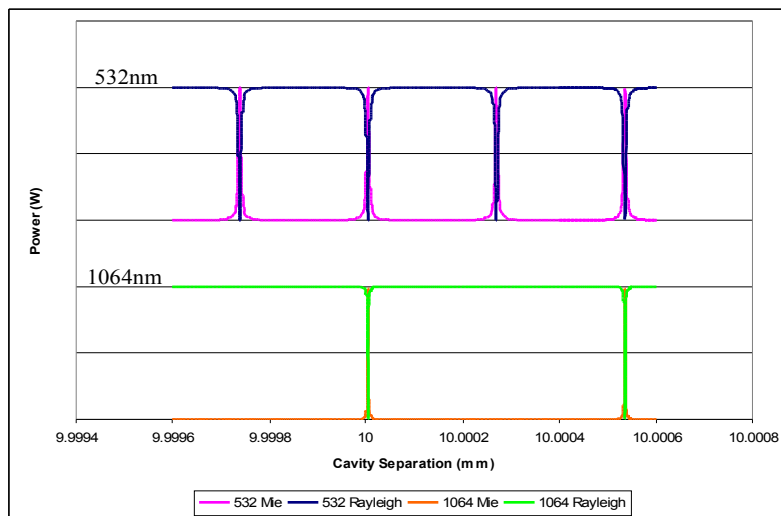


Figure 2-18. The resonances for a 532 nm source compared with a 1064 nm source, as determined by FRED model.

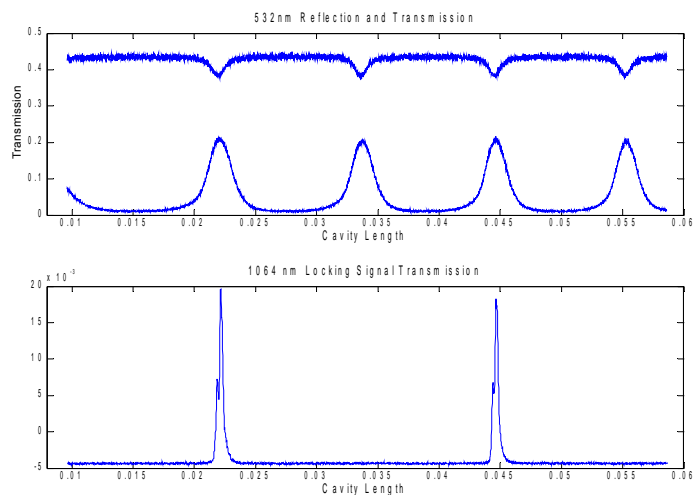


Figure 2-19. The measured cavity transmission and reflection as a function of cavity separation for 532 nm (top) and the transmission for 1064 nm (bottom), from the HSRL at MSU (Hoffman et al. 2012).

The modeled resonances occur as expected, matching the observed resonances at MSU. The 1064 source has an observably higher finesse because the coating for this

wavelength has a higher reflectivity. Scattering and absorption are not taken into account in the modeled plots, which likely accounts for the differences in the shape, and the additional noise in the experimental results.

2.3.2 Angular Analysis of the SFPI

A planar FPI (PFPI) has been used as the narrow band filter in HSRL systems (Shipley 1983), but a limiting factor for a PFPI is the small acceptance angle. Ideally only one FSR is incident on the image plane at any time. The angle to one FSR is defined by h , the distance from the PFPI to the image plane, and the incident wavelength, as shown in equation 2-25 and figure 2-20 (Kovalev 2004). The small acceptance angle can limit the size of the primary collection optics of a lidar because of etendue requirements.

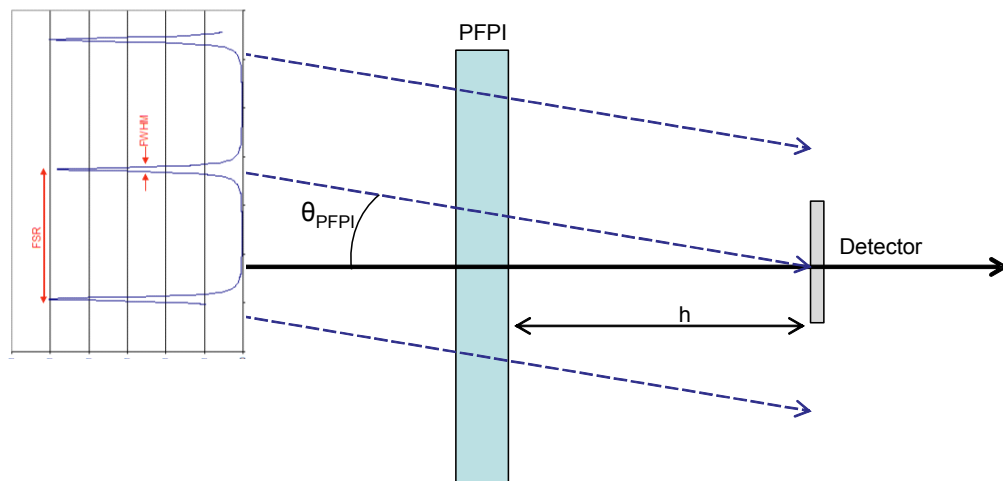


Figure 2-20: Illustration of the acceptance angle limitations for a PFPI.

$$\theta_{PFPI} = \left[\frac{\lambda}{h} \right]^{1/4} \quad (2-25)$$

Alternatively, a perfectly aligned paraxial SFPI, as discussed elsewhere in detail (Johnson 1968, Hercher 1968), is resistant to changes in the entrance angle because the optical axis is merely redefined with these changes. In general, its insensitivity to misalignment is an advantage of the SFPI over the PFPI, but there are limits. “Ideal illumination” theoretically allows for 100% transmission, but the conditions for “ideal illumination” can be impractical. With a more practical “non-ideal illumination,” the maximum transmission rate is 50%. For the HSRL at MSU, the SFPI was chosen for use as the narrow band filter partially because of its insensitivity to angular misalignment (Hoffman et al. 2012).

If a fiber is used to couple the received photons onto the SFPI, its parameters will determine the incident angle. At MSU, a multi-mode fiber is used to couple the receiver telescope to the receiver optics because a single-mode fiber allows an insufficient throughput. In this case, the angle of the beam incident on the SFPI depends primarily on the fiber parameters, because the multi-mode fiber will emit rays over an angular range that is dependent on its numerical aperture (NA). This angular range will typically be small enough to fall within the acceptance angle of the SFPI. For this analysis, the total SFPI acceptance angle is examined, not simply the range determined by the fiber. However, the $f/\#$ of the beam incident on the cavity is determined by the NA of the fiber and the lenses that are in place, and are considered in the design methodology.

In the previous section, the effect of spherical aberration on the finesse was discussed. The beam height, fiber NA (if applicable), and the radius of curvature

determine the finesse from spherical aberration, F_{SA} , and if the beam height is large enough, F_{SA} becomes the limiting factor in the total finesse. Because a lens is used to focus the beam onto the cavity center, a change in the angle of the beam incident on the system will result in a change in the beam height incident on the SFPI, and of the beam height in the cavity center, as illustrated in figure 2-21.

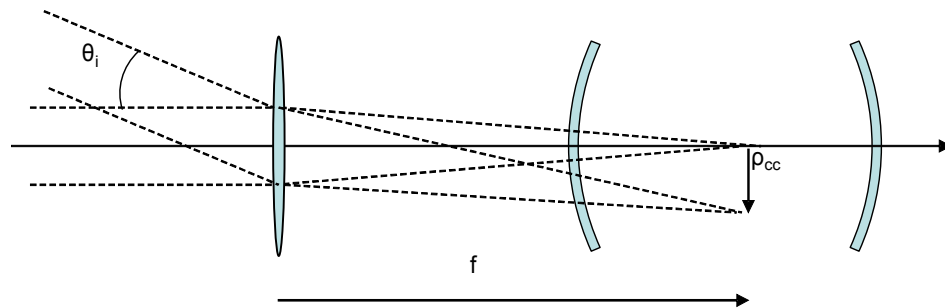


Figure 2-21: Illustration of the effect that a change in the incident angle will have on the beam height at the center of the SFPI.

The incident angle, θ_i , is related to the beam height in the cavity center, ρ_{cc} , by the focal length of the lens, f , so that $\tan(\theta_i) = \frac{\rho_{cc}}{f}$.

Although a SFPI is less susceptible to changes in the incident angle than the PFPI, a SFPI does see an impact from the entrance angle. This is illustrated with two experiments; the first measures the transmitted and reflected power from the SFPI as an on-axis source is scanned through an angular range. The second experiment measures the transmitted and reflected power from the SFPI as an off-axis source is scanned through an angular range. For both experiments, the source is incident on a lens that focuses the beam onto the center of the SFPI.

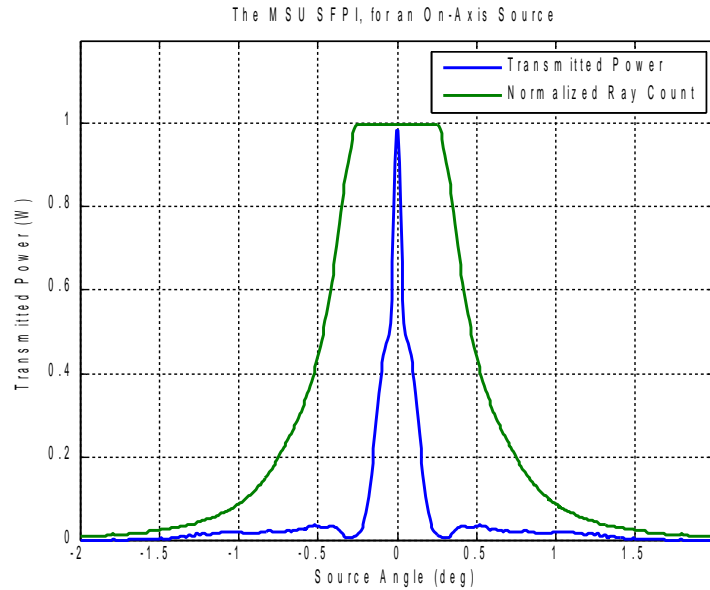


Figure 2-22: The transmission for an on-axis SFPI source, for a range of incident angles.

To portray the on-axis case using FRED, the angle of the source incident on the focal lens was scanned across a range of values, with the transmitted and reflected power measured at each angle. The power is normalized to one, and the number of rays incident on the detector is also accounted for. As seen in figure 2-22, as the angle causes the optical path traveled through the SFPI to move away from resonance, the power quickly drops to approximately half of the initial transmitted power. This quick drop off in transmission occurs at approximately 0.03 degrees, and is attributable to the change in illumination as the incident angle moves it away from the ideal case. As the incident angle (and corresponding beam radius) increases, the expected transmission shifts from the expected 100% for ideal illumination to the expected 50% for non-ideal illumination. At 0.25 degrees the ray count on the detector begins to drop off, and there is a slower

drop-off in transmission from 50% to zero. This slower drop-off has several causes, including rays walking off the detector (figure 2-23), coherent ray errors (as previously discussed), and moving off-resonance due to changes in the optical path length from the incident angle (equation 2-10). In this case, the coherent ray errors are caused by secondary beamlets that have become too divergent, and deviated too far from a Gaussian.

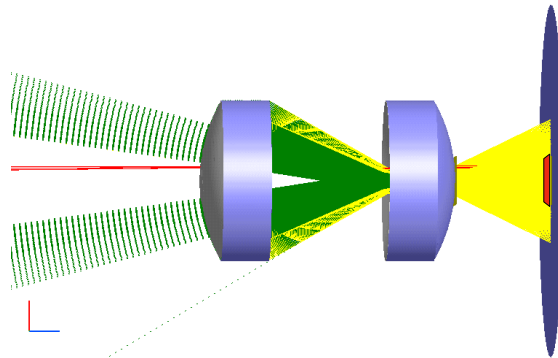


Figure 2-23: The FRED model of the SFPI at a resonant cavity length, with the source angle tilted at 0.33 degrees in the y-axis. The transmission detector is on the right, highlighted in red. It's apparent that some transmitted rays (yellow) are not incident on the detector.

To portray the off-axis case using FRED, the source was off-set from the optical axis by 0.5 mm, and the angle of the source was scanned across a range of values, with the transmitted and reflected power measured at each angle. The result of this analysis is shown in figure 2-24, where it's apparent that the majority of the transmission is below 50%, and the maximum transmission is 56%. The decrease in the maximum peak is caused by the departure of the illumination from the ideal situation. Because of the

departure from the optical axis, the beam is no longer focused in the center of the SFPI for the larger source angles.

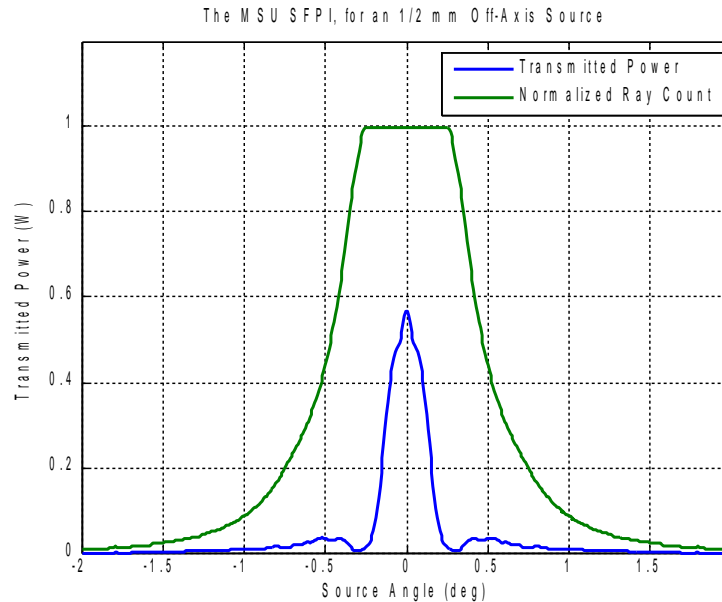


Figure 2-24: The transmission for a SFPI source that is offset from the optical axis by 1/2mm, for a range of incident angles.

When figure 2-22 and 2-24 are compared, the effect of shifting the source off-axis is seen. When the source goes off-axis, the maximum transmission drops dramatically, although the angular window for 50% transmission is maintained for small departures from the optical axis. Because the MSU HSRL uses the more practical non-ideal illumination, their SFPI has a maximum transmission of 50%. Therefore the interferometer is somewhat impervious to changes in the incident angle, and the acceptance angle is approximately ± 0.25 degrees.

2.3.3 Analysis of the SFPI Efficiency

In this section, the efficiency of the SFPI as a narrow band filter in a HSRL is

evaluated using its throughput and maximum transmission. The throughput is derived, and the modeled MSU SFPI transmission is discussed.

Generally, the throughput of a spectrometer can be represented by the memorable equation (Hercher 1968)

$$P = NUT_0 \quad , \quad (2-26)$$

where P is the radiant power per unit bandwidth, T_0 is the transmission of the spectrometer at the center of the bandpass, N is the spectral radiance of the source, and U is the throughput of the spectrometer. In terms of Ω , the solid angle subtended from the aperture, and A , the aperture area, the throughput U is given by

$$U = A\Omega \quad . \quad (2-27)$$

In the case of a PFPI with an on-axis aperture the throughput is dependent on the area of the aperture and its spectral properties, so that $\Omega = (2\pi\Delta\lambda)/(\lambda_0)$, and

$$U_{PFPI} = \frac{2\pi A_{FP}\Delta\lambda}{\lambda_0} \quad , \quad (2-28)$$

where A_{FP} is the aperture area of the planar FPI, $\Delta\lambda$ is the FPI bandpass, λ_0 is the central wavelength, and the solid angle subtended by the telescope is

$\Omega_T = (2\pi[1 - \cos(\theta_T)])$, where θ_T is the angular field-of-view of the telescope (Measures 1984).

Previously it was discussed that the highest finesse can only be found with perfect illumination due to spherical aberration. The imperfection decreases with the smaller aperture size, so that with an infinitely small aperture, the finesse is perfect, but quickly

moves to 50% efficiency with an increase in aperture. However, an infinitely small aperture means an infinitely small throughput, so a practical balance between finesse and throughput must be found.

The throughput of a SFPI is given by

$$U_{SFPI} = A_{SPI} \Omega_{SFPI} = (\pi \rho_s^2) \left(\frac{\pi \rho_s^2}{L^2} \right) , \quad (2-29)$$

where ρ_s is the mirror radius whose resonant frequency is displaced from the axial resonant frequency by the free spectral range (Hercher 1968). As the aperture becomes larger, the resolving power begins to decrease proportional to the deceleration in the increase of throughput. A value of 70% of the initial resolving power has been suggested to have an acceptable balance between finesse and throughput (Connes 1956, Vaughn 1989). This allows the maximum value of the change in optical path length due to spherical aberration (Δ_{SA}) to be

$$\Delta_{SA}(max) = \pm \frac{2\lambda}{F_{SA}} , \quad (2-30)$$

which corresponds to $\cos(2\theta) = \pm 1$, and is obtained when

$$\rho_s = \left(\frac{L^3 \lambda}{F} \right)^{1/4} . \quad (2-31)$$

Combining equations 2-29 and 2-31, it is seen that the ideal throughput of a SFPI is dependent on the finesse, F , so that

$$U_{SFPI} = \frac{\pi^2 L \lambda}{F} \quad (2-32)$$

Where L is the separation of the mirrors, which, in a confocal system, is equal to the

radius of curvature of the mirrors (Hercher 1968, Vaughan 1989). Thus, the throughput of a SFPI is limited by its finesse. The maximum throughput of the SFPI at MSU is calculated to be $1.036\text{E-}09\text{ m}^2$.

The transmission of the MSU SFPI is evaluated using the FRED model of the system. Throughout this analysis, a single-watt source is used, and the resulting power on the detectors is given as a percentage of that initial watt. Because of the multi-mode source, the maximum transmission through the MSU SFPI is 50% (Hoffman 2012), as previously discussed. This is illustrated in the FRED model when the imperfect illumination is taken into account. The ideal illumination would give a theoretical transmission of 100% through the SFPI, but this would require an axially symmetric, single-mode source with an infinitely small aperture, which would reduce the throughput to an unusable value. For these reasons, the maximum realistic transmission of the SFPI is 50%, which has proven to be sufficient for HSRL operation at 532 nm (Hoffman et al. 2012).

2.4 Summary of the SFPI Analysis

This chapter discussed the viability of the SFPI for use as the narrow band filter in a HSRL in terms of a spectral, angular, and throughput/transmission analysis. The resolving power (RP) of the SFPI, a critical element of a spectral filter, was derived using the finesse. The variables that affect the acceptance angle of the SFPI were discussed,

and the practicality of obtaining a satisfactory acceptance angle for this interferometer was determined. The transmission and throughput were discussed in terms of the efficiency of the SFPI. The throughput was derived and found to depend on the finesse, and, therefore, on the geometry of the interferometer. In the next chapter, the RP for a wide-angle Michelson interferometer (WAMI) (another multi-spectral option for the narrow band filter in a HSRL) is derived and discussed. Additionally the acceptance angle necessary for an acceptable efficiency is found. The WAMI efficiency is discussed, and a value for the throughput of a WAMI is derived. These values are compared with this analysis of the SFPI for the purpose of creating a general design methodology for a narrow band filter in a multi-spectral HSRL.

CHAPTER 3:

THE WIDE ANGLE MICHELSON INTERFEROMETER

3.1 Introduction and Description

This chapter discusses the principles of operation of a WAMI as the narrow band filter in a HSRL, how it has been modeled and implemented, and presents an analysis of the WAMI. A wide-angle Michelson interferometer (WAMI) is a modified Michelson interferometer, used as a narrow band spectral filter in this application. The modifications to the standard Michelson interferometer include replacing one arm of the interferometer with a glass slab in order to widen the acceptance angle. By aligning the transmission fringes of the interferometer with the Doppler broadened backscattered lidar signal, the WAMI can serve as a narrow band filter.

The lidar team at NASA LaRC has implemented the WAMI as the narrow band filter in their second generation Airborne HSRL. The first generation Airborne HSRL-I at NASA LaRC is a successful system that uses an iodine vapor absorption filter to spectrally separate the Doppler broadened lidar return (Hair 2006). It provides measurements of aerosol backscatter and extinction coefficients at two wavelengths, and has been deployed for over 1,000 flight hours (Hair et al. 2008). In 2004, a second generation HSRL was proposed by NASA LaRC, and as of this writing, field tests of the Airborne HSRL-II are being conducted. The second generation Airborne HSRL-II uses a WAMI that was developed and tested at LaRC (Liu et al. 2012) for use at 355nm. There

is a second elastic scatter lidar at 1064nm that has no spectral separation of the Mie and Rayleigh backscatter, so it cannot extract the aerosol backscatter and extinction as is done with the 355nm HSRL. An etalon and a field-widened Mach-Zehnder interferometer were also considered for the HSRL narrow band filter, and ultimately rejected in favor of the WAMI, which was implemented using a technique similar to that used by Bruneau and Pelon (2003). This technique is described in Section 3.2.3.2, where it is used to model the system.

A WAMI can be used as a narrow band spectral filter by inducing complementary fringes in the two beam paths and centering the phase on the Mie signal. The WAMI is tilted to allow two output signals to be measured: the standard Michelson output (the “forward channel”), and the output initially reflected back towards the source (the “reverse channel”). At NASA LaRC, the forward channel is used for the Mie signal, and the reverse channel is used for the Rayleigh signal, but depending on the geometry of the WAMI, either channel can be used for each return. In this case, the Mie channel uses the constructive interference centered on the Mie frequency to enhance the Mie signal, while the destructive interference eliminates the broader Doppler broadened Rayleigh return. In the same manner, the Rayleigh channel uses the destructive interference centered on the Mie frequency to eliminate the Mie signal from the Rayleigh channel, while the “wings” are positioned in the region of constructive interference (Bruneau & Pelon 2003). A schematic of the spectral filtering (Liu et al. 2012) is given in figure 3-1, where the output spectra in the upper position is the Mie channel, and the spectra in the lower

right position is the Rayleigh channel.

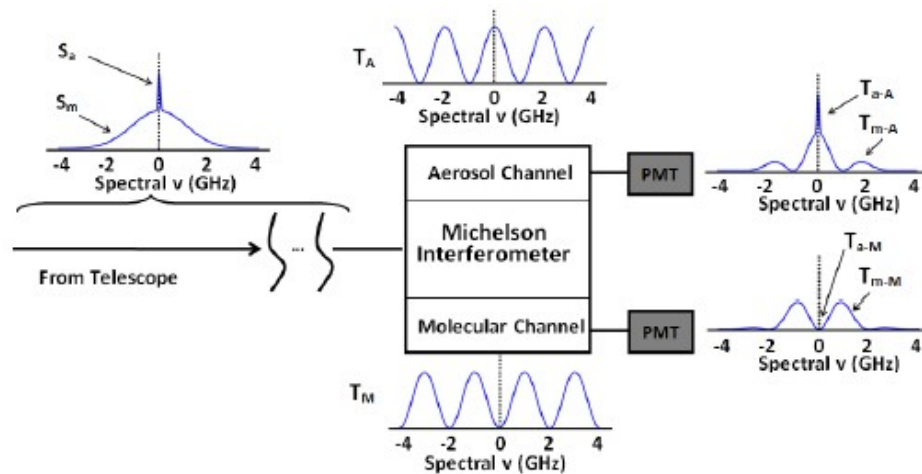


Figure 3-1: A schematic diagram of a WAMI, from Liu et al. (2012) at NASA LaRC.

The research presented in this chapter details the WAMI at NASA LaRC and the process of accurately modeling and analyzing it. The models presented here are used to obtain a transmission function for this WAMI. To determine the signal through a WAMI, the transmission function is convolved with the modeled lidar returns (the Simple Gaussian and Bruneau Method, discussed in chapter 1). This modeled signal is used to perform an in-depth analysis of the efficiency and spectral and angular qualities of the WAMI as a narrow band filter.

3.1.1 Standard Michelson Interferometer

In a Michelson interferometer (MI), a source is incident on a beam splitter, as seen in figure 3-2, and divided into two beam paths, each of which is incident on a mirror (M_1 or M_2), and then reflected back toward the beam-splitter. The two beams are recombined and emerge from the interferometer perpendicular to the path direction of the

source beam. M_1 is coplanar with the image of M_2 when it is in Position 1, and is displaced from the image of M_2 when in Position 2, but is still parallel. The rays that were initially divided at the beam-splitter emerge co-linearly when M_1 is in Position 1, because there is no difference in the path length of the two arms (this is evident by observing that the two beam paths form identical triangles). It is clear that the path length difference is independent of the incident angle of the source. However, if M_1 is shifted into Position 2, the path length difference is no longer zero, and becomes a function of the incident angle. The rays that emerge when M_1 is in Position 2 have a relative displacement, depending on their beam path, so that the path length difference is a function of the incident angle of the source.

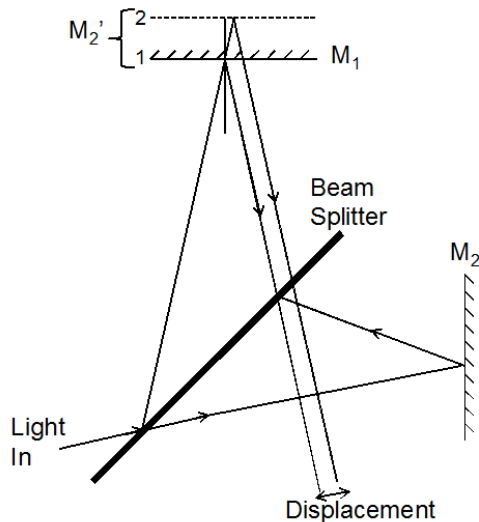


Figure 3-2: A standard Michelson interferometer (Hilliard 1966).

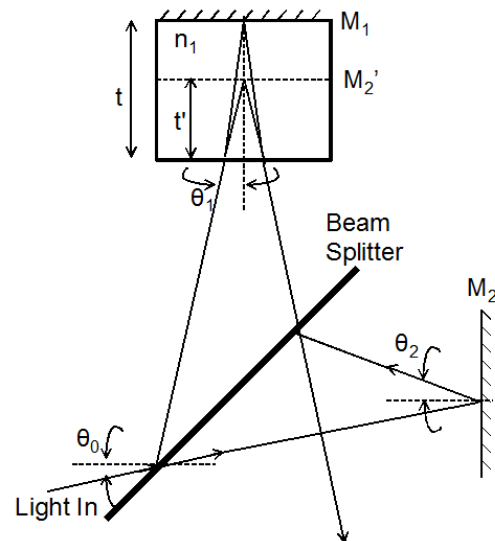


Figure 3-3: A wide-angle Michelson interferometer (Hilliard 1966).

3.1.2 Wide-Angle Michelson Interferometer (WAMI)

A Wide-angle Michelson Interferometer (WAMI) is a Michelson interferometer

that has been modified, or “field-compensated,” to allow for a larger acceptance angle. One arm in a WAMI is replaced by a glass slab with an aluminized rear surface that acts as the mirror for this arm (figure 3-3). The second arm remains the same: the beam passes through air and reflects from a mirror to the beam-splitter where it recombines with the beam from the glass arm. The glass arm is placed so that the image of the mirror (M_2') aligns with the virtual image of its reflecting face (M_1) as seen in figure 3-3 (Hilliard, 1966). The result is that the beams from the glass and air arm of the interferometer emerge collinearly, despite a non-zero optical path difference (OPD). This condition is referred to as the “Quasi-Zero Position” or QZP, and occurs when $t' = t/n$, where t is the physical length of the glass arm, n is the index of refraction, and t' is the optical length of the glass arm. By adding this glass arm, the OPD between the two arms of the WAMI becomes a function of the incident angle of the source, in addition to depending on the materials and lengths of both arms.

If the beam-splitter has a perfect 50/50 coating, and the two arm lengths are d_1 and d_2 , then the OPD between the two WAMI arms is

$$OPD = 2n_1d_1\cos(\theta_1) - 2n_2d_2\cos(\theta_2) \quad (3-1)$$

where Snell's Law tells us that $n_0\sin\theta_0 = n_{1,2}\sin(\theta_{1,2})$, so that

$$OPD_{MI} = 2 \left[n_1d_1 \left(1 - \frac{\sin^2(\theta_0)}{n_1^2} \right)^{1/2} - n_2d_2 \left(1 - \frac{\sin^2(\theta_0)}{n_2^2} \right)^{1/2} \right]. \quad (3-2)$$

When $\sin(\theta_0)$ is expanded, and the QZP is set on the WAMI so that

$$\frac{d_1}{n_1} = \frac{d_2}{n_2} , \quad (3-3)$$

then the OPD of the WAMI is

$$OPD_{WAMI} = 2(n_1 d_1 - n_2 d_2) - \frac{\sin^4(\theta_0)}{4} \left(\frac{d_1}{n_1^3} - \frac{d_2}{n_2^3} \right) - \frac{\sin^6(\theta_0)}{8} \left(\frac{d_1}{n_1^5} - \frac{d_2}{n_2^5} \right) \dots \quad (3-4)$$

where the higher order terms can be ignored for small angles.

3.1.3 The WAMI at NASA LaRC

At NASA LaRC, the WAMI was designed to transmit the Mie backscatter at a central wavelength of 355nm, and includes a tilt of 1.5 degrees that is necessary to separate the forward and reverse channels (Liu et al. 2012). As shown in figure 4, the beam that is reflected from the WAMI is incident on a small mirror that redirects this light into the reverse channel. The solid arm is made of fused silica, and is 87.576mm in length. The air arm has an index of refraction of 1.00027 and is 59.318mm long. The solid arm is optically connected with the cubic polarizing beam splitter, but is not cemented (the end of section 3.2.1 discusses how this is handled in the model). The beam splitter is 50mm x 50mm x 50mm. Both WAMI mirrors have a highly reflective coating, and other than the splitter surface, all other glass surfaces have an anti-reflection (AR) coating.

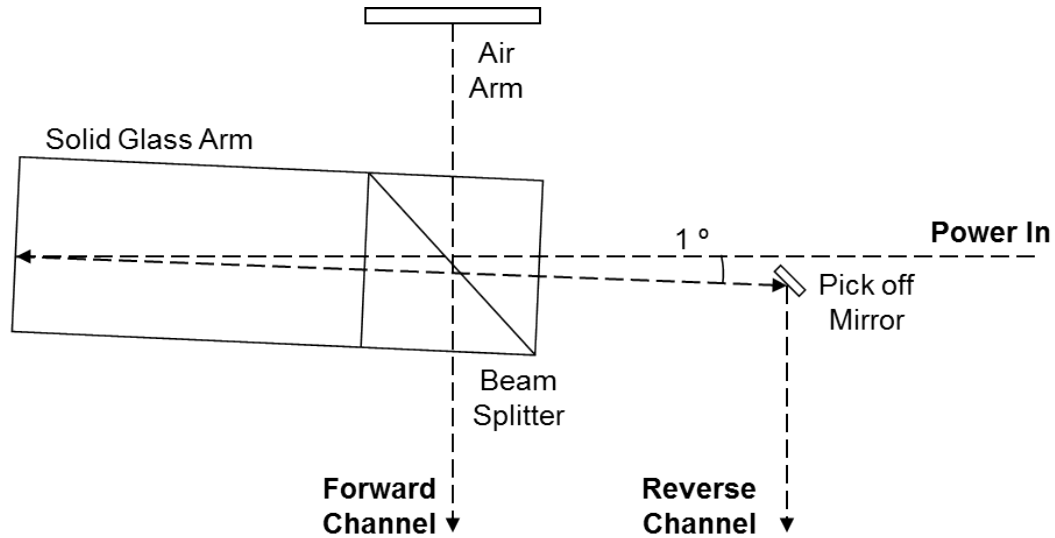


Figure 3-4: A schematic of the WAMI, and the tilt necessary to separate the forward and reverse channels (Liu et al. 2012).

There are three coatings on the optics in the WAMI: an AR coating, a high-reflection (HR) coating, and a 50/50 splitter coating. The standard CVI-Melles Griot coating profiles were digitized and used for the WAMI model in this research. Figure 3-5 shows the VSI triple-V AR coating (Antireflection 2013) that is designed for the Nd:YAG frequencies. Figure 3-6 shows the standard HR coating (Optical Coatings 2013) used by CVI-Melles Griot, with a relative wavelength. The splitter coating has a 50/50 division for s-polarized light, and a low reflectance (3% to 8%) for p-polarized light.

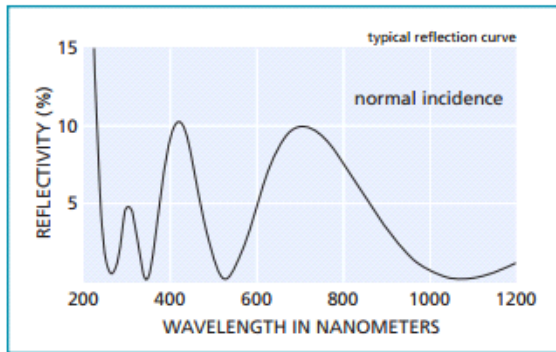


Figure 3-5: Triple-V AR coating designed for 355, 532, and 1064 nm, from CVI-Melles Griot (*Antireflection 2013*).

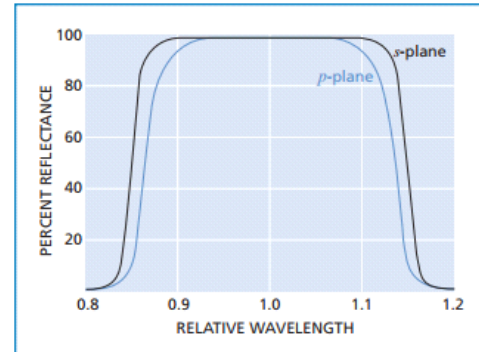


Figure 3-6: High Reflective coating, from CVI-Melles Griot (*Optical Coatings 2013*).

3.2 WAMI Modeling

3.2.1 Modeling the WAMI in Ray-Tracing Software

The WAMI was modeled in Zemax by the lidar team at LaRC; using those files (which were generously provided by NASA LaRC), an accurate model of the WAMI was constructed using FRED ray-tracing software. The dimensions, materials, and coatings of the WAMI were addressed in Section 3.1.3, and the ray-tracing software met those specifications. A graphic of this model is shown in figure 3-7, where the glass arm reflective surface is labeled as Mirror 1, and the air arm mirror is labeled as Mirror 2. A large part of creating a useful FRED model is ensuring that the source is correctly modeled.

Using the Zemax models provided by LaRC, the beam size at the entrance of the WAMI was found to be 10mm in RMS radius. This is the maximum spot size, from nine

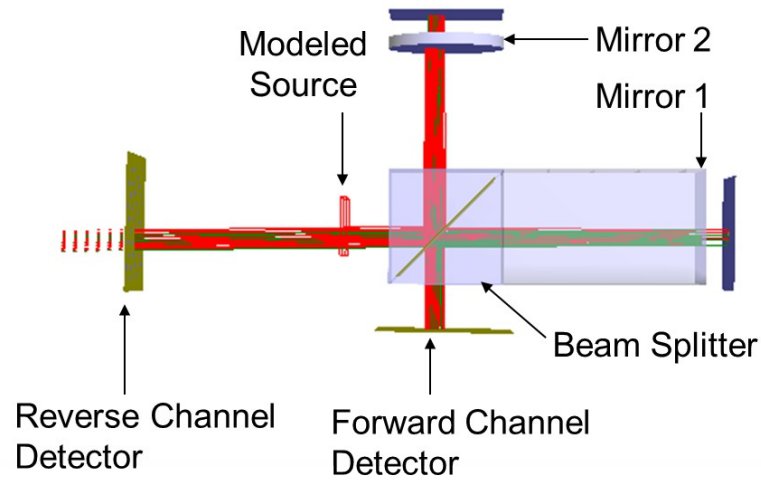


Figure 3-7: A schematic of the WAMI modeled in FRED.

different field locations with $(x=0, y=3.088\text{mm})$ being the furthest from the optical axis.

The spot diagrams at the WAMI entrance aperture are shown in figure 3-8. All of the fields are collimated before incidence on the interferometer. Additionally, the source has a central wavelength of 355nm, and is coherent, single-mode, randomly linearly polarized with a Gaussian power distribution and a full-field divergence of 16 mrad (0.92 degrees).

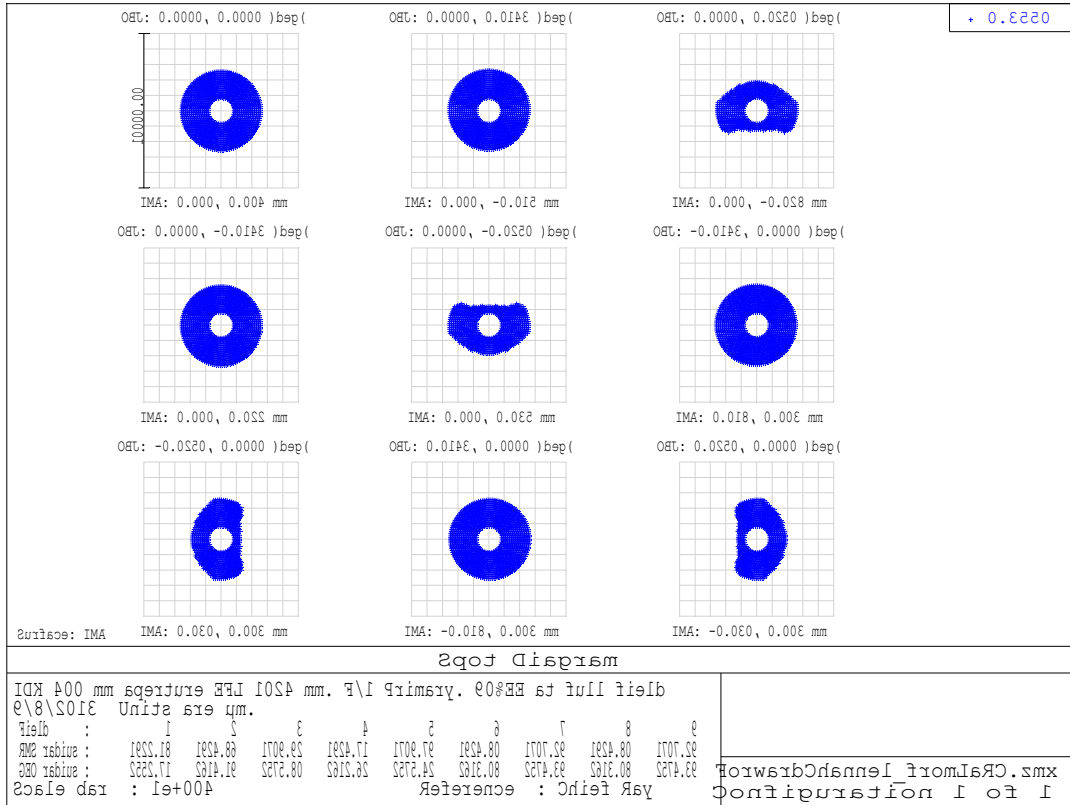


Figure 3-8: Spot diagrams shown for 9 different field angles, at the entrance face of the WAMI. These diagrams were produced using a Zemax file provided by NASA LaRC.

When a coherent source is used in FRED, the detector (or analysis plane) must be defined using the specifications of the source. The defining relationship is

$$\omega_0 = \sqrt{\frac{4}{\pi}} \left(\frac{W(OF)}{2N} \right) \quad (3-5)$$

where ω_0 is the beam waist radius at the $1/e^2$ point, W is the source grid size, OF is the beam overlap factor for a coherent source (the default value is 1.5), and N is the number of rays in each dimension. OF has a default value of 1.5. For example, if the beam radius is 12.7mm, the beam waist is $12.7/\pi = 4.044\text{mm}$, and the

number of rays traced in each dimension should be 2.65, so 3 rays will be traced in each dimension. This relationship also applies when determining the size and pixels in an analysis plane, except in that case, N refers to the number of pixels across the grid. The analysis grid is set to 51x51, with 111 pixels across each dimension. This set up allows for distinct delineation of the fringes without oversampling.

As previously mentioned, the WAMI beam splitter and the glass arm are optically connected, but are not cemented together. In the FRED model, if these materials are in contact, there is a “Material Ambiguity” error present, which causes several ray tracing problems; the most significant of these is incorrect power values, by half, on each detector. To solve this, the correct parameters for the WAMI tilt, the separation of Mirror 2, the wavelength, and the source tilt are set, while the distance between Mirror 1 and the beam splitter is allowed to vary, shown in figure 3-9. The variable “S” labels the distance that is varied: refer to figure 3-7 for the labeled WAMI layout. This distance was scanned through a reasonable range while the power on each detector was recorded. The result, shown in figure 3-10, shows that the errors caused by the material ambiguity error are iterative. Because there is a 50/50 coating on the beam splitter surface, 50% of the incident light is expected on each detector in an ideal situation. The shortest distance between Mirror 1 and the beam splitter that accommodates this, 174.26nm, is used, and the material ambiguity errors are eliminated.

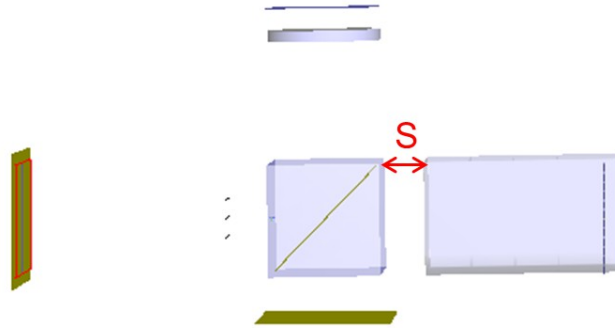


Figure 3-9: The distance "S" is varied to find the optimal spacing between Mirror 1 (the glass arm) and the beam splitter, in order to eliminate material ambiguity errors in FRED.

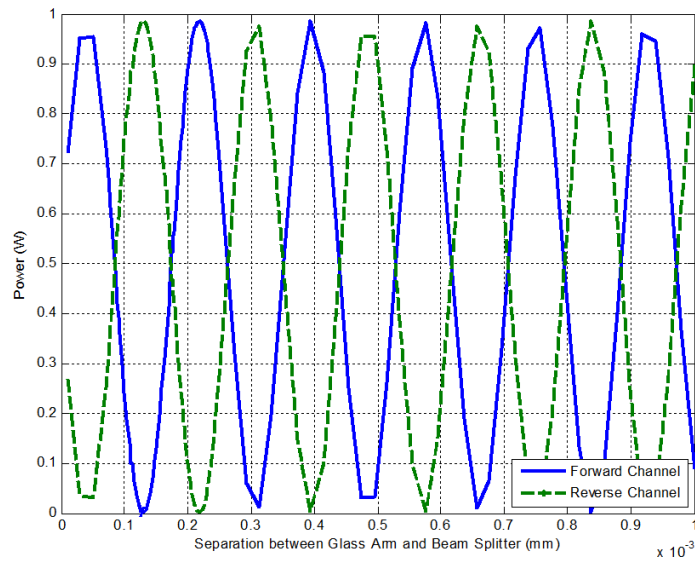


Figure 3-10: The power on each detector for a range of separations between the beam splitter and the glass arm (Mirror 1), labeled "S" in figure 3-9.

3.2.2 FRED Model Verification

To confirm that FRED is correctly modeling the WAMI, tilt is added to the Air Arm Mirror, and the number of fringes is confirmed using the following equations:

$$2 n d \cos(\theta) = m \lambda \quad (3-6)$$

and

$$\sin(\phi) = \frac{d}{D_{MI}} \quad (3-7)$$

When equations 3-6 and 3-7 are combined, it's found that the input tilt angle for Mirror 2 (the air arm) is

$$\phi = \sin^{-1}\left(\frac{m\lambda}{2D_{MI}}\right) \quad (3-8)$$

where

n = index of refraction,

d = path difference due to tilt,

θ = incident angle of source,

m = order number (number of predicted fringes),

λ = source wavelength,

ϕ = tilt angle of mirror, and

D_{MI} = diameter of beam on tilted mirror.

With these specifications in the WAMI model, three fringes are expected for a tilt of 8.475E-4 degrees, and seven fringes are expected when the mirror has 1.978E-3 degrees of tilt. The expected results are shown in figure 3-11, confirming the ability of FRED to

correctly model interference.

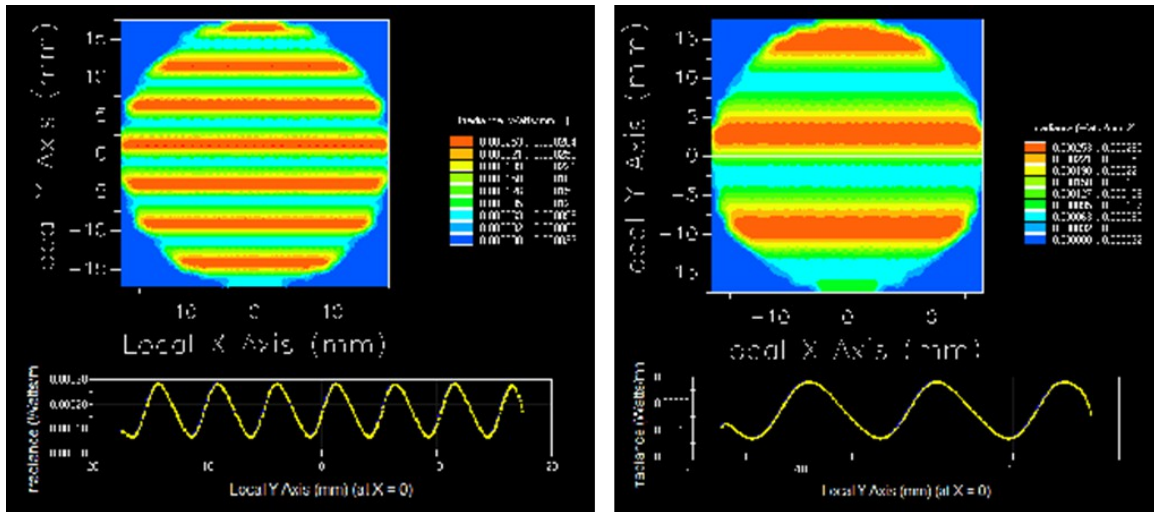


Figure 3-11: The irradiance profile at the forward detector for a WAMI with 1.978×10^{-3} degrees of tilt on the left, and for a WAMI with 8.475×10^{-4} degrees of tilt on the right. Note the expected 7 fringes on the left and the 3 fringes on the right.

3.2.3 WAMI Transmission Functions

The transmission function of each channel is a critical element of the interferometer. It determines how the light is transmitted, and therefore which channel can act as the narrow band filter, as well as its spectral characteristics. In this section, two methods of determining the WAMI transmission function are discussed, as well as the method to derive the signal on the detector via convolution with the lidar backscatter return. The first method to derive the transmission function involves using the model created with the ray-tracing software package FRED. The second method, done for verification purposes, derives the transmission function mathematically using a method described by Bruneau (2001). Lastly, these transmission functions are convolved with the two models for the lidar backscattered return (discussed in Chapter 1), and the results

are compared.

3.2.3.1 Modeled Transmission Function

A transmission function for the WAMI is found using the model created using Zemax and FRED ray-tracing software. The Zemax model, provided by the LaRC lidar team, was used to generate the FRED model and analysis. To create this wavelength dependent transmission function, the incident wavelength was varied while the power on the detectors was monitored. The spectral dependence of the transmission through the two paths in the WAMI is shown in figure 3-12.

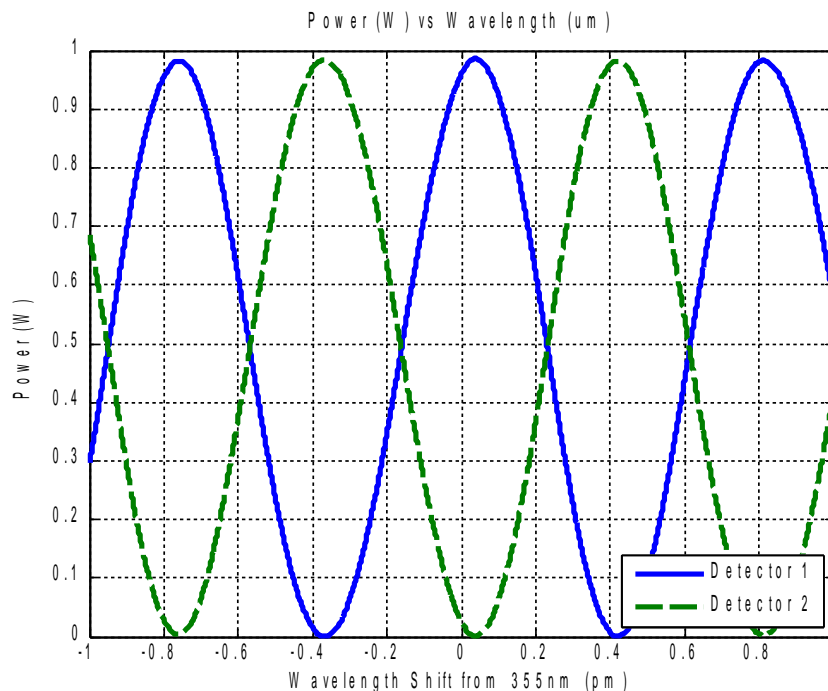


Figure 3-12: Transmission through two paths in the WAMI, using the FRED model.

3.2.3.2 Bruneau Transmission Function

To calculate a transmission function for comparison with the FRED model, the

method followed by the NASA LaRC HSRL team (Bruneau et al. 2003 and Liu et al. 2012) was followed. The index of refraction for the glass arm of a WAMI is found using the Sellmeier coefficients for fused silica, so that

$$n(\lambda)^2 - 1 = \frac{B_1 \lambda^2}{\lambda^2 - C_1} + \frac{B_2 \lambda^2}{\lambda^2 - C_2} + \frac{B_3 \lambda^2}{\lambda^2 - C_3} , \quad (3-9)$$

where

$$B_1 = 0.6961663 ,$$

$$B_2 = 0.4079426 ,$$

$$B_3 = 0.8974794 ,$$

$$C_1 = 0.00467914826 ,$$

$$C_2 = 0.0135120631 ,$$

$$C_3 = 97.9340025 .$$

This wavelength dependent index is used to calculate the OPD for the WAMI at LaRC, as shown earlier in equation 3-4. The transmission function for each WAMI channel (forward and reverse) produces complementary fringes, shown in figure 3-13, so that

$$T_1(\lambda) = \sin^2\left(\frac{\pi OPD}{\lambda}\right) \quad T_2(\lambda) = \cos^2\left(\frac{\pi OPD}{\lambda}\right) . \quad (3-10)$$

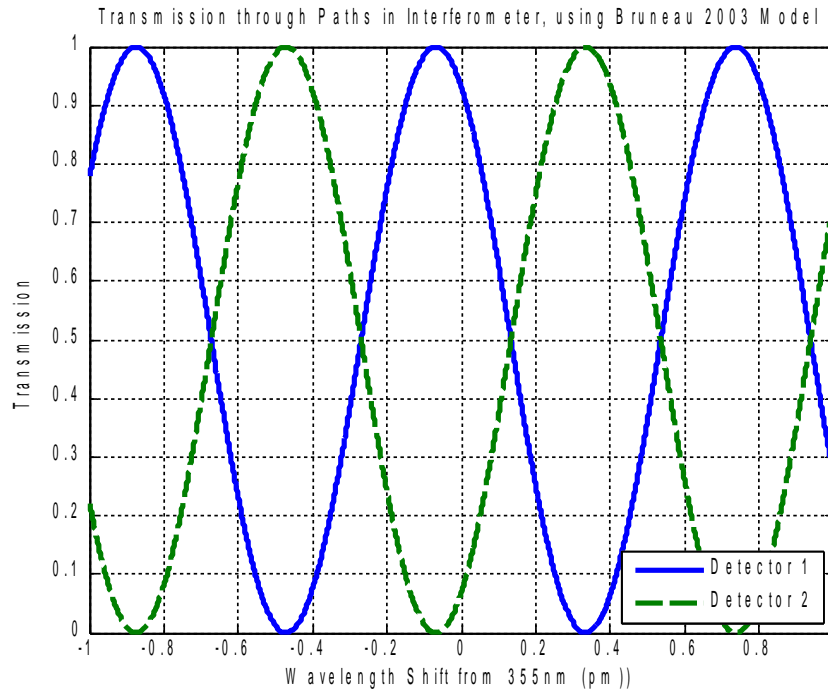


Figure 3-13: Transmission through two paths in the WAMI, using the Bruneau transmission function.

The assumption is made that the incident irradiance is divided between the two channels by a perfect 50/50 beam splitter coating, and no light is absorbed by the glass (Bruneau 2001). The code that was written and used for these calculations is given in Appendix C.

When figure 3-12 and 3-13 are compared, it's notable that there is a phase shift of 95 femtometers from the FRED modeled transmission function to the theoretical Bruneau transmission function. The period is approximately 0.8pm, therefore the modeled phase (figure 3-12) is 11.8% higher than the theoretical version (figure 3-13). However, the period and amplitude are consistent from the model to the theoretical calculations.

3.2.3.3 Modeling the Signal on the Detector

The signal observed at the detectors, $S_i(\lambda)$, is calculated using the convolution

of a lidar return and a transmission function (Bruneau 2001). In these calculations, the detectors are assumed to have equal and perfect sensitivity, but this can be taken into account in the models, where q is the sensitivity of each detector (seen in Appendix C), $I(\lambda)$ is the lidar return, and $T_i(\lambda)$ is the transmission function, and \times indicates a convolution:

$$S_1(\lambda) = qI(\lambda) \times T_1(\lambda) \qquad S_2(\lambda) = qI(\lambda) \times T_2(\lambda) \quad . \quad (3-11)$$

Using a combination of the two modeled lidar returns (the Simple Gaussian and Bruneau), and the two calculated transmission functions (FRED and Bruneau), Signal 1 and Signal 2 were evaluated separately for the four possible combinations of the lidar return and the transmission function (Simple Gaussian return with the Bruneau transmission function, Simple Gaussian return with the FRED transmission function, Bruneau return with the Bruneau transmission function, and the Bruneau return with the FRED transmission function). Using these signals, which are separately incident on the modeled detectors, the plots in figure 3-14 were created. It is apparent that there are slight differences in the models, but they show the same effect, namely, that the two paths in the WAMI effectively separate the Mie and Rayleigh lidar return. The largest difference is observed between the Gaussian and the Bruneau lidar return models. The simplified Gaussian produces a clearer signal on the detector, but the Bruneau return takes some atmospheric criteria into account. The only discernible differences between the effects of the two transmission functions are explained by the phase shift mentioned in the previous section. This provides additional verification of the FRED model as a

virtual experiment.

Each signal, S_1 and S_2 , has both Rayleigh and Mie contributions, because there is not a 100% rejection for either channel. This is taken into account using the method discussed in section 1.3.4. In the model presented here, the assumption of the perfect 50/50 beam splitter coating is continued in the assumption that the Rayleigh backscattered signal is evenly split between the two channels. The Mie signal, however, is spectrally narrower than the period of the transmission function, and therefore can be perfectly filtered in this model. In practice, a number of factors such as glass inhomogeneity, parallelism between the two Michelson arms, and alignment, will detract from the transmission of each channel (Liu 2012).

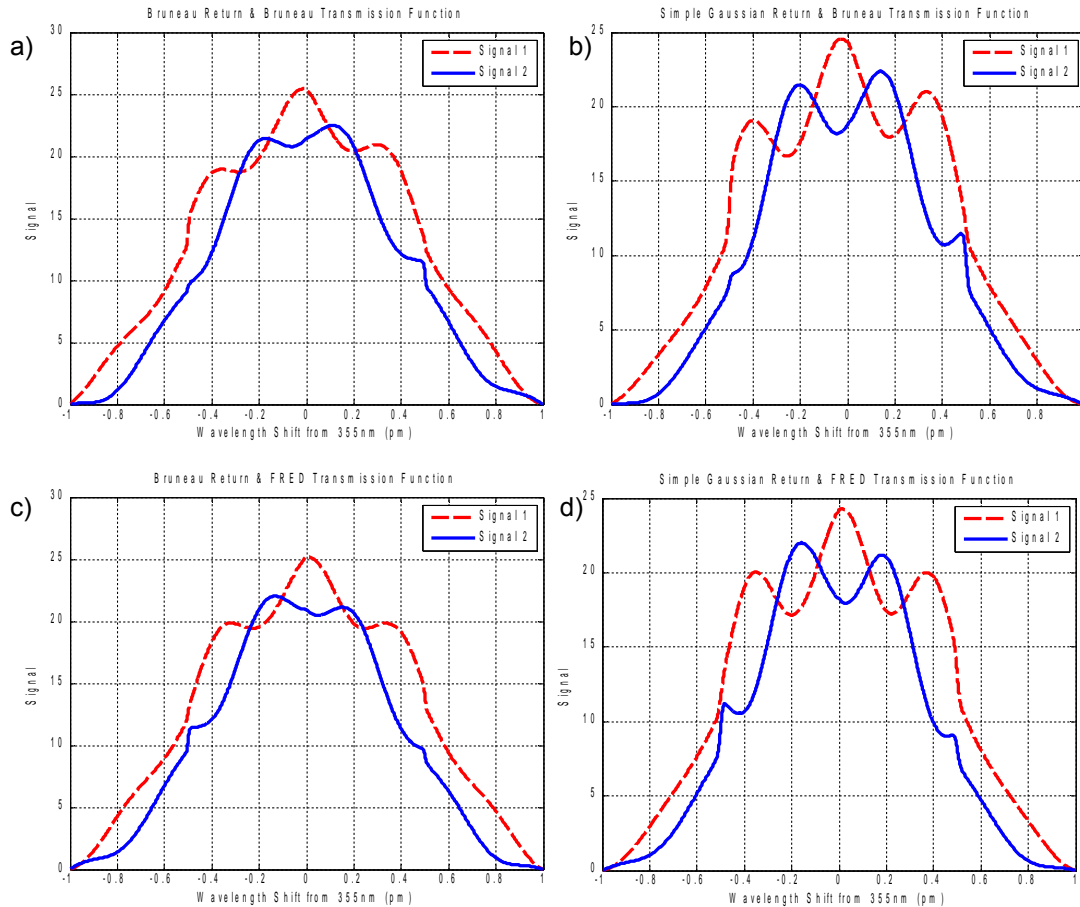


Figure 3-14: Comparisons of the signal on the detector for four scenarios. The signals are evaluated separately. (a) The Bruneau return model with the Bruneau transmission function, (b) the Simple Gaussian return model with the Bruneau transmission function, (c) the Bruneau return model with the FRED transmission function, and (d) the Simple Gaussian return model with the FRED transmission function.

To evaluate the total power incident on each detector, each curve in figure 3-14 is spectrally integrated over 2pm, centered at 355nm, and the results are shown in figure 3-15, along with the average value for the four scenarios. Both the Bruneau lidar return and the Bruneau transmission function return a higher value for the signal on the detector than either the Gaussian return or the FRED transmission function. However, the difference

between the two lidar return models is greater by an order of magnitude than the difference between the two transmission functions. From this result, it's assumed that the Bruneau and the FRED transmission functions are functionally equal; the lidar return model chosen for the analysis has a greater impact on the results. This also serves as a verification of the FRED lidar model, which is used in the following analysis.

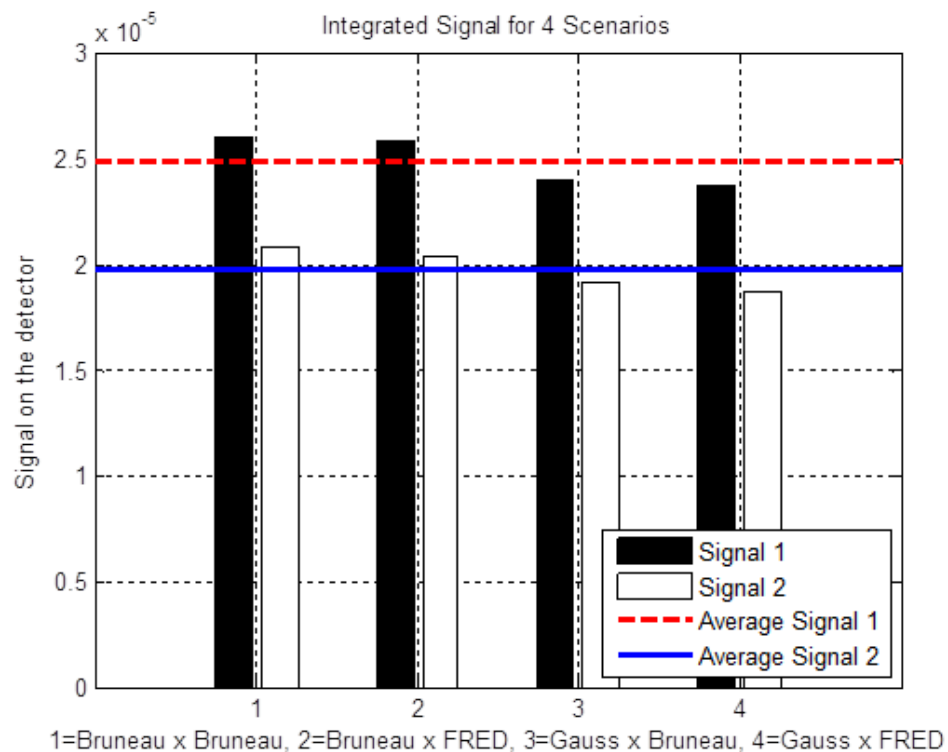


Figure 3-15: The power on each detector (Signal 1 and 2) for the four scenarios shown in Figure 3-14. It is labeled so that where $A \times B$, A = the model for the lidar return, and B = the model for the transmission function.

3.3 Analysis of the WAMI

In this section, the WAMI is analyzed using the FRED model discussed and verified in Section 3.2. The analysis is done in terms of the spectral and angular capabilities, and the WAMI efficiency, and mirrors the analysis of the SFPI in Chapter 2.

3.3.1 Spectral Analysis of the WAMI

The resolving power of the WAMI is found using the OPD, and is used for a comparative analysis with the SFPI for use as the narrow band filter in a HSRL. Additionally, the spectral reaction of the WAMI is analyzed for several possible variables, including changes in the glass arm length and the effect of the index of refraction of the glass arm.

3.3.1.1 The Resolving Power of the WAMI

When used as a narrow band filter in a HSRL, the WAMI is designed to be a fixed element during operation (although there are piezo stacks for tuning purposes). If the WAMI were designed to scan, then theoretically the resolving power (RP) of this interferometer would be defined by the limits of the scan. However, here the RP is limited by the signal-to-noise ratio (SNR) and should be thought of as the best possible spectral width. The optimum RP is found when

$$\omega \Delta_{\omega} = \frac{2\sqrt{\ln 2}}{\pi} , \quad (3-12)$$

where ω is the line width, and Δ_{ω} is the OPD (Hilliard 1966). In the case of the WAMI at LaRC, equations 3-4 and 3-12 are used to find that (at the central wavelength) the OPD is 1.4E5, and the optimal line width, ω , is 3.79 picometers. By defining the

RP to be the wave-number, $\sigma = \lambda^{-1}$, divided by the line-width, ω , and using the optimal line width, the RP of the WAMI is found to be

$$RP_{WAMI} = \frac{\pi OPD_{WAMI}}{2\lambda(\sqrt{\ln(2)})} \quad (3-13)$$

If equation 3-13 is assumed to be approximately equal to $\frac{1}{2}$, then RP_{WAMI} becomes

$2\sigma OPD_{WAMI}$, which, as Hilliard (1966) points out, is the same RP that is found for a standard Michelson interferometer.

3.3.1.2 Effect of the Glass Arm on WAMI Signal

The glass arm of the WAMI is obviously a large part of the design process. The speed of the selected wavelength through the material, or the index of refraction, must be balanced with the length of the arm to produce the OPD necessary for the desired RP. The goal is to maximize the signal from one type of scatterer (e.g. the Mie signal) in one channel, while minimizing it in the other channel.

To examine the effect of the glass arm length on the signal, the integrated power of the signal through each channel is found for a range of arm lengths. As expected, the signal has a cyclical dependence on the glass arm length, as shown in figure 3-16. The length of the glass arm in the LaRC WAMI is marked with the red vertical line, and produces a modeled signal that is close to the maximum (minimum) possible for Signal 1 (Signal 2). If the length were decreased by 8 nanometers, it would be precisely at the modeled ideal. Between the maximum and minimum signal value, there is approximately 0.2 microns of difference in length in the glass arm, and between the optimal and sub-

optimal signal strengths, there is 0.09 microns difference in the length. The LaRC WAMI could potentially be optimized with an alternative length for the glass arm, but the tolerances necessary for this exceed what is practical. Instead, sensitivity of the glass arm length to factors that affect its stability, such as temperature, are key to maintaining the stability of the signal. It should be noted that in this model, the Bruneau lidar return and the Bruneau transmission function are used for ease of calculation.

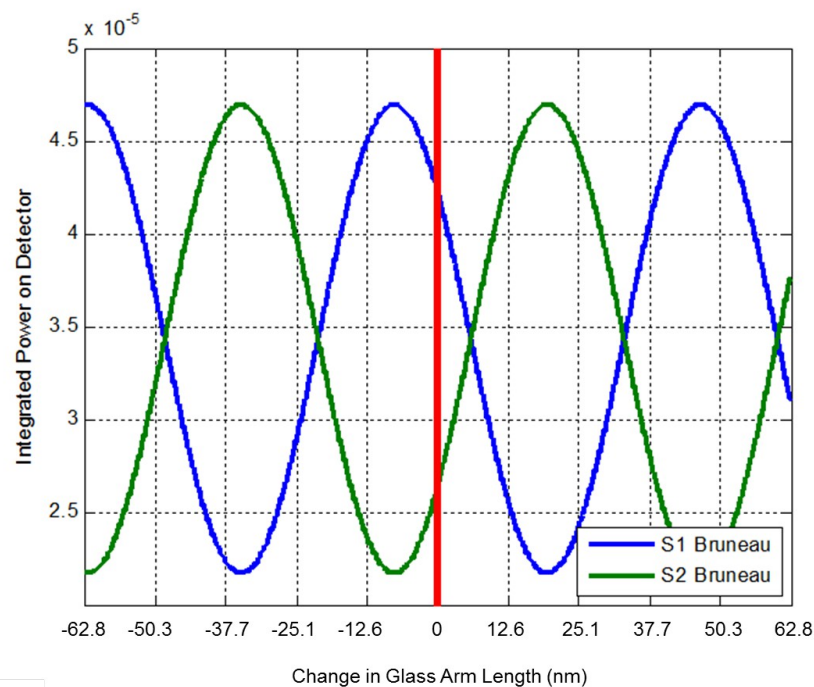


Figure 3-16: The effect of the glass arm length on the signal, for the WAMI at LaRC. The x-axis is the shift away from the LaRC WAMI glass arm length of 87.578um, indicated by the red vertical line.

To examine the effect of the index of refraction on the signal, the index is varied across a reasonable range for known glasses, and the integrated power on the detector is recorded for each channel (Signal 1 and Signal 2). Figure 3-17 shows the \sin^2

transmission function with an enveloping cosine function incident on the detectors as the index is scanned through a range of values. Because most optical glass has an index that falls between 1.2 and 2.5, this range is examined in more depth in figure 3-18. Again, the vertical lines in represent the solution used at NASA LaRC, where fused silica was used for the glass arm. This glass has a very low CTE, which contributes to the stability of this WAMI.

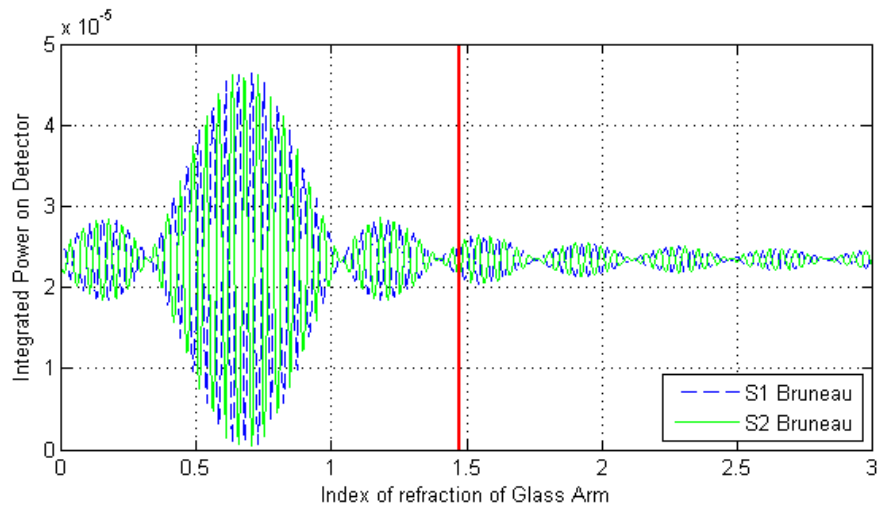


Figure 3-17: The effect of the index of refraction on the WAMI signal. The red vertical line indicates the index for the LaRC WAMI.

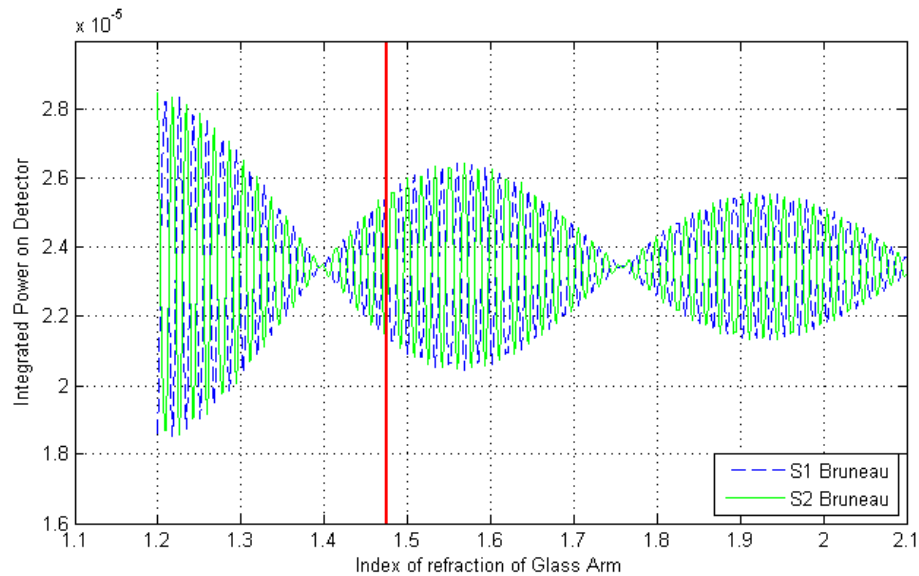


Figure 3-18: The effect of the WAMI's index on the signal. This plot is a close-up of figure 3-17. The red vertical line indicates the index for the LaRC WAMI.

As these figures show, a small deviation from the design (such as ± 0.1 index or 16nm difference in the glass arm length) could quickly escalate into the reversal of the WAMI channels. While the instrument could function in this situation, it would have to be accounted for in the data analysis, so the index and arm length must be accurately monitored. Temperature changes could affect the WAMI operation by causing small changes in the glass arm length or temperature induced index fluctuations; although the LaRC WAMI uses fused silica (which has a very low coefficient of thermal expansion), the WAMI is operated within a thermally controlled box. The design of the LaRC WAMI called for a fused silica glass arm of 87.576mm in length, and the system has been optimized (Liu et al. 2011), analyzed (Liu et al. 2012), and determined to be sufficient for the purpose of serving as the narrow band HSRL filter.

3.3.2 Angular Analysis of WAMI

The angular analysis of the LaRC WAMI includes discussions of the effects of two angular variables on the signal level. The first is the WAMI tilt necessary to separate the forward and reverse channels, and the second is the analysis of the WAMI acceptance angle.

3.3.2.1 WAMI Tilt Angle

The WAMI has a tilt angle in order to separate the reverse channel from the incident beam. A pick-off mirror is inserted into the beam path, and redirects the beam into the reverse channel as it exits the interferometer, as illustrated in figure 3-4. This tilt angle changes the effectiveness of the WAMI as a narrow band filter. The LaRC WAMI was originally designed to have a tilt with respect to the incident light of 1.5 degrees, but after additional analysis, LaRC oriented the WAMI to have 1 degree of tilt with respect to the incident beam.

The optimal OPD for this model, 139mm, was found using the index of refraction at the central wavelength, 355nm, with zero degrees of tilt. It favorably compares to the value of 150mm that NASA LaRC found using different models (Liu et al. 2012). The OPD for a standard Michelson, OPD_{MI} , and the OPD for a WAMI, OPD_{WAMI} , are calculated using equations 3-2 and 3-4, and compared to the optimal value in figure 3-19. The standard Michelson OPD differs from the optimal OPD value at significantly smaller tilt angles than the WAMI OPD, showing that the WAMI has a wider range of potential tilt angles for this application. The difference between the optimal OPD and OPD_{MI} ,

and the optimal OPD and the OPD_{WAMI} were also found, and are plotted in figure 3-20, and can be verified with a similar plot from the NASA LaRC team found using alternative models (Liu et al 2012, figure 3). At an acceptance angle of 1 degree, the OPD of the WAMI departs approximately 8.6 waves from the optimal performance, while the standard Michelson departs by 76.8 waves.

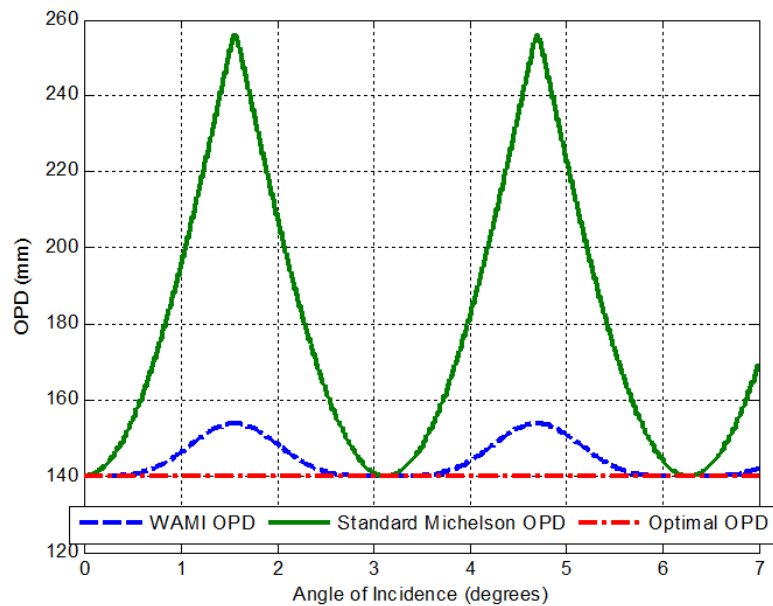


Figure 3-19: The optimal OPD, the OPD for a standard Michelson interferometer, and the OPD for a WAMI, plotted for a range of tilt angles.

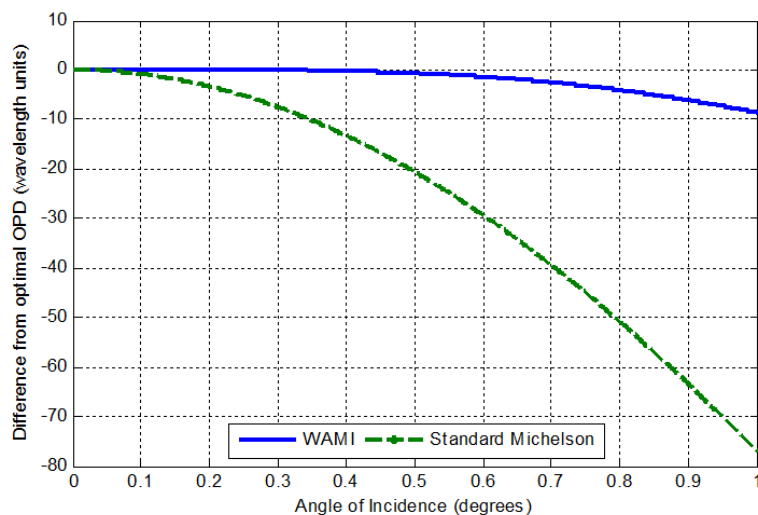


Figure 3-20: The difference between the optimal OPD and the WAMI OPD, plotted with the difference between the optimal OPD and the OPD for a standard Michelson, for a range of tilt angles, plotted in wave units.

A smaller tilt angle would not have been effective, because the pick off mirror would shadow the interferometer. This is shown in figure 3-21, where the power on each detector is plotted for a range of tilt angles from 0 to 3 degrees. The sum of the power on both detectors is tracked, to ensure that the law of conservation of energy is not broken. The number of modeled rays on each detector is also plotted to see exactly when the beam wanders off the detector. The number of rays on the detectors has been normalized to 0.5 so that any deviations can be easily observed. At a tilt angle of 2.5 degrees, the sum of the power on each detector becomes erratic, indicating a breakdown in the conservation of energy. There is also a loss of accuracy in the measurements that occurs at tilt angles over 1 degree due to the falloff of the rays incident on detector 2. Because of the shadow from the pick off mirror, the most efficient tilt angle for this WAMI is 1

degree, which is what is used in the HSRL at LaRC.

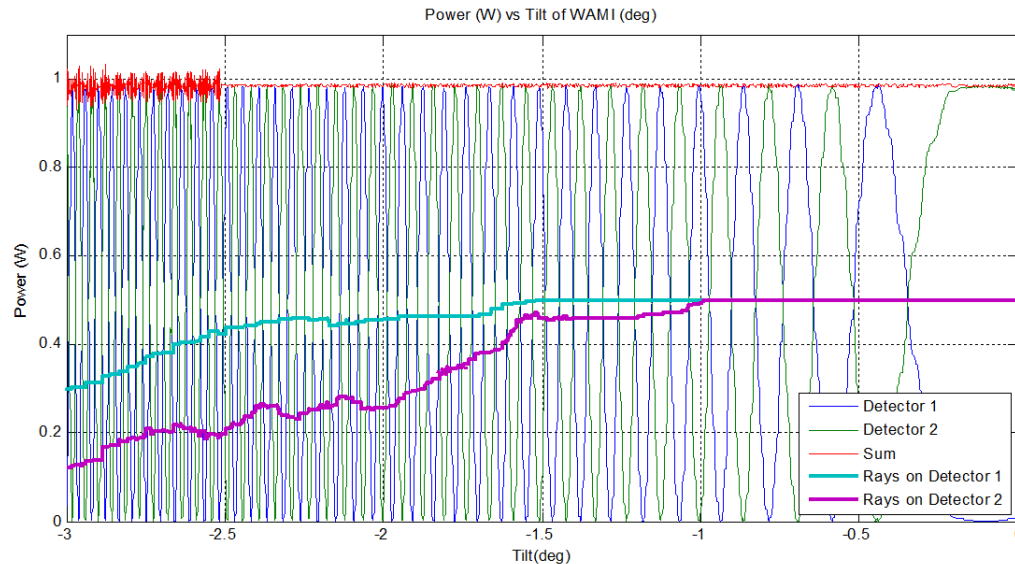


Figure 3-21: The power on each detector for a range of WAMI tilt angles, using the FRED model set at the central wavelength of 355nm. The power sum, and the number of rays on each detector is also plotted. In this plot, the source has no divergence, and is perfectly centered.

3.3.2.2 WAMI Acceptance Angle

The acceptance angle of the WAMI is defined here as the largest incident angle at which a meaningful signal can be obtained. To examine this, the FRED model is used, and the power on each detector is tracked for a range of source angles. The WAMI has a window of 2 degrees (± 1 degree) in which all of the rays are incident on a detector. The photon efficiency decreases as the source goes off axis, and the SNR decreases. The center of this 2 degree window changes according to two factors: the tilt of the WAMI itself, and the divergence of the source. There is a central “peak” around which the source angle response is symmetric. As the source angle differs more from the peak, the frequency increases, meaning that the tolerance for the source angle decreases. In

addition, the divergence of the source angle affects the shift of this central peak from the WAMI tilt angle by the value of the half-field divergence. As the central peak shifts away from the center of the ray count, the beam is walking towards the edge of the detectors, as shown by the decrease in the ray count.

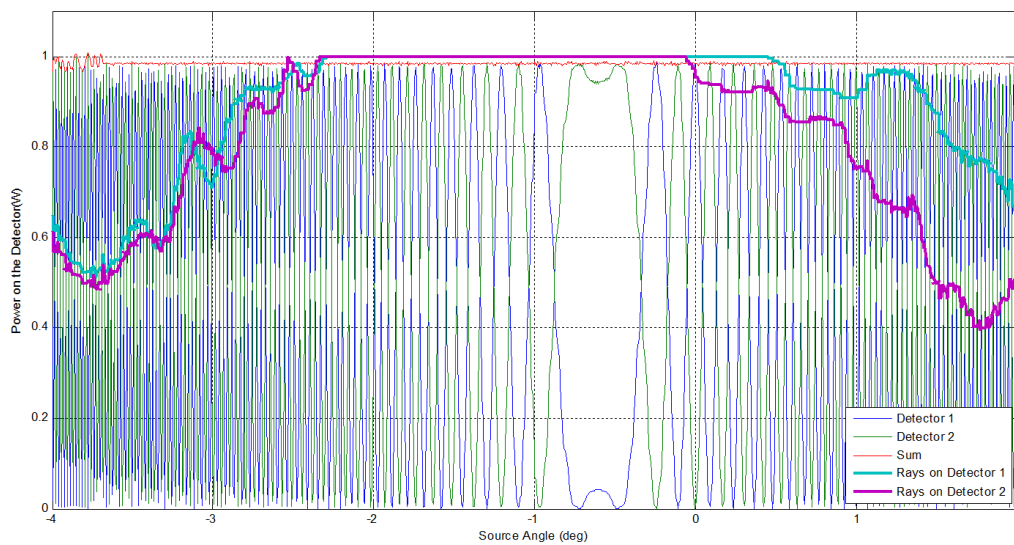


Figure 3-22: The power on each detector for a range of source angles, and the ray count for the respective detectors. For the LaRC WAMI, with a full field source divergence of 0.92 degrees, and a WAMI tilt of -1 degrees.

The reaction of the LaRC WAMI to a change in the source angle is shown in figure 3-22. This WAMI has a -1 degree tilt from the normal, and the source has a divergence of 0.92 degrees. The central peak is shifted from -1 degrees by the half-field divergence. When this figure is compared with figure 3-21, the 2 degree window is apparent in both. Verification of this tolerance was presented by the LaRC lidar team (Liu et al. 2012, figure 6), that found a similar 2 degree half-field range for the source divergence. Similarly, in figure 3-22, the ray count falls off outside of a two degree half-

field divergence range.

The tilt of the WAMI and the divergence of the source must be balanced with each other in order to maximize the photon efficiency of the interferometer.

3.3.3 Analysis of the WAMI Efficiency

In this section, the efficiency of the WAMI as a narrow band filter in a HSRL is evaluated using its throughput and maximum transmission. The throughput is derived, and the modeled transmission of the LaRC WAMI is discussed.

Throughput, or etendue, is essentially the geometric extent of a system, and is invariant throughout. To calculate the throughput of a WAMI, the solid angle of the source and the area of the entrance aperture must be known (Thome 2007). The solid angle of a spectrometer is dependent on its spectral properties so that

$\Omega = (2\pi\Delta\lambda)/(\lambda_0)$, where $\Delta\lambda$ is the bandpass of the spectrometer, and λ is the design wavelength. As previously mentioned in equation 2-20, the resolving power (RP) of a system is defined as $RP = \lambda/\Delta\lambda$, so the solid angle of the WAMI is defined as

$$\Omega_{WAMI} = \frac{2\pi}{RP} \quad (3-14)$$

The entrance aperture is the square face of the WAMI beam splitter, whose area can be defined by its radial height h , squared, so that $A_{WAMI} = \pi h^2$, and the throughput for a WAMI is

$$U_{WAMI} = \frac{2\pi^2 h^2}{RP} . \quad (3-15)$$

Using equations 3-4, 3-13, and 3-15, the maximum throughput of the WAMI at LaRC is calculated to be $4.2826e-09 m^2$.

The maximum WAMI transmission was plotted in figures 3-13 and 3-14. Figure 3-13 was created using the FRED model of the WAMI at LaRC, and shows the maximum transmission being over 95%. Figure 3-14 was created using the Bruneau method previously detailed in section 3.2.3.2, and records a theoretical transmission rate of 100%.

3.4 Summary of the WAMI Analysis

This chapter discusses the viability and use of a WAMI as the narrow band filter in a HSRL in terms of spectral, angular, and throughput analysis. The RP of the WAMI was derived using the OPD, and the spectral effect of the design choices and tolerances for the glass arm were analyzed and discussed. An analysis of the angular changes that effect the WAMI performance is included, including the tilt angle of the WAMI with respect to the incident light and the acceptance angle. The WAMI throughput is derived, and is found to depend on the acceptance angle and the entrance aperture height. In the next chapter, this analysis is compared with the previous SFPI analysis for the purpose of creating a general design methodology for a narrow band filter in a multi-spectral HSRL.

CHAPTER 4:

COMPARATIVE ANALYSIS AND DESIGN METHODOLOGY

4.1 Introduction

The WAMI and the SFPI are both capable of being used as the narrow band filter in a HSRL, and a one to one comparison of the two interferometers, as well as a design methodology, are included in this chapter. Both the WAMI and the SFPI have strengths, depending on the application and operational scenario. For this comparison, the interferometers are compared primarily “as-built” by their respective institutions, meaning that no major changes were made to the design before the analysis, unless otherwise stated. This chapter includes a comprehensive comparative analysis of the SFPI and the WAMI, and presents a generalized design methodology for future HSRL systems that is based on that analysis.

The criteria for the comparative analysis include the spectral, angular, and efficiency analyses that are presented in chapters 2 (SFPI) and 3 (WAMI). For the spectral analysis, the resolving power (RP) of the interferometers is used as a metric for comparison. While additional angular considerations were addressed in the previous chapters, the acceptance angle is the angular comparison criteria. Finally, the efficiency of each interferometer is compared using the throughput and the transmission. Moreover, the iodine vapor absorption filter is briefly compared with the SFPI and the WAMI.

In the design methodology, the factors that affect the comparison criteria are addressed, and a method for designing an interferometric narrow band filter for a HSRL

according to the spectral, angular, and efficiency requirements of the system is presented. In section 4.3.1, the science application is considered, and questions are asked regarding the intersection between the science and engineering. Additionally, lists of candidate specifications to consider for the SFPI and the WAMI are included to provide a starting point for a system designer. In sections 4.3.2, 4.3.3, and 4.3.4, design considerations are addressed that affect the spectral, angular, and efficiency performance of the narrow band filter. In each section, specifications that affect the performance are analyzed, and optimization methods are included. In section 4.3.5, the design methodology is summarized, and an abbreviated version is presented.

4.2 Comparative Analysis of a SFPI and a WAMI

In chapters 2 and 3, the spectral and angular qualities, and the efficiency of a particular SFPI and a particular WAMI were analyzed. The metrics used to evaluate these qualities are the RP, the acceptance angle, the throughput, and the transmission. Values were found for these metrics for each interferometer, and the factors causing them were described. In this section, these metrics for evaluation and criteria for comparison are compared and discussed.

4.2.1 Spectral Comparative Analysis

The narrow band filter in a HSRL is used to separate the Mie and Rayleigh backscattered lidar return, as discussed in Chapter 1. The spectral width necessary to spectrally separate these two signals has a spectral dependence, and for visible

wavelengths it is on the order of 3 picometers. A narrow band filter with a very high RP can precisely eliminate the aerosol (Mie) scatter from the total lidar return, with minimal losses to the Rayleigh signal. Therefore, the RP is the chosen spectral comparison metric; it is defined as the ratio of the wavelength to the spectral width. This linear relationship means that the ideal RP must rise proportional to the design wavelength of the interferometer. Given this dependence, the RP for the SFPI and WAMI is plotted in figures 4-1 and 4-2 for the same spectral range. Additionally, the FRED model of each interferometer is evaluated at four common wavelengths, and the RP for each is listed in table 4-1.

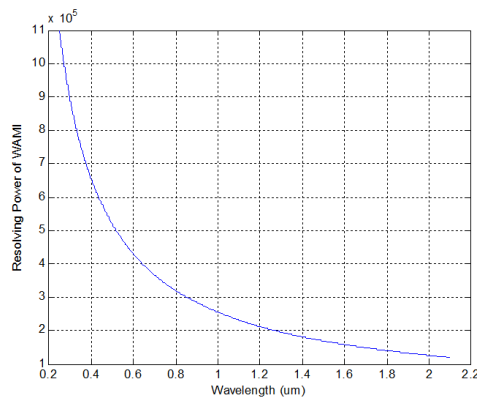


Figure 4-1: The RP of the LaRC WAMI for a range of wavelengths. The maximum RP is $11E5$ at $0.2 \mu\text{m}$.

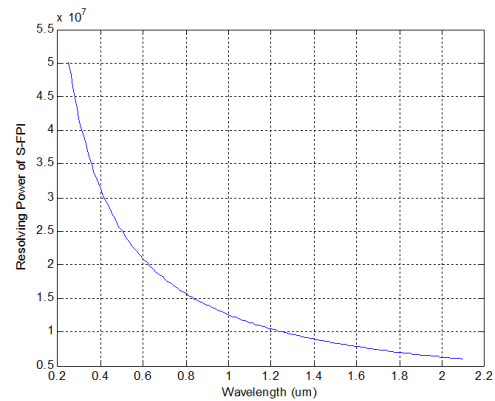


Figure 4-2: The RP of the MSU SFPI for a range of wavelengths. The maximum RP is $5.5E7$ at $0.2 \mu\text{m}$.

	355nm	532nm	1064nm	632nm
WAMI	7.43E+005	4.87E+005	2.40E+005	4.08E+005
SFPI	3.53E+007	2.36E+007	1.18E+007	1.98E+007

Table 4-1: The RP for the WAMI and SFPI at four common wavelengths.

In all cases, the SFPI has a higher RP by two orders of magnitude. In an application where there are other factors detracting from the RP, or where a narrower spectral width is necessary, this should be considered.

4.2.2 Angular Comparative Analysis

The acceptance angle is a critical design consideration, especially in a long-range lidar application, such as a space-based or airborne HSRL. To evaluate the acceptance angle of each interferometer, a source was scanned through a range of angles while the power on each detector was monitored.

The acceptance angle of the MSU SFPI was analyzed in chapter 2; a larger range of acceptance angle (± 10 degrees) is examined in more detail here with the assumption that a fiber may not always be used in a HSRL receiver. In figure 4-3, the source is incident on the cavity itself, and there is no lens to focus the beam into the center of the SFPI. The power that is transmitted and reflected from the cavity is plotted along with the ray count, which is normalized to 1 in this figure, and is identical for both the transmitted and the reflected detector. The ray count declines rapidly outside of ± 5 degrees, which is a function of the aperture of the next optical element (the active area of the detector in this case). Within that range of ± 5 degrees, the transmitted power declines rapidly from 100% to 50% as the source angle causes a departure from the ideal illumination. For a minimum of 75% (90%) transmission, the acceptance angle is ± 0.04 (± 0.024) degrees. Assuming that a 50% rate of transmission is acceptable (which it is for the MSU HSRL), the acceptance angle becomes ± 1 degree. The reflected power

has a complementary curve when the SFPI is examined on its own, as it is in figure 4-3, but when its examined in the context of an entire HSRL system, additional space is needed in order to separate the incident beam from the reflected beam with a pick off mirror (as discussed in chapter 2). The longer beam path can cause the beam in the reflected channel to exceed the diameter of the detector. The transmitted channel can face the same limitations, but there are no additional optics on that side of the cavity, so a relay lens could potentially be used to collect the escaping rays if the beam exceeds the transmitted detector's diameter.

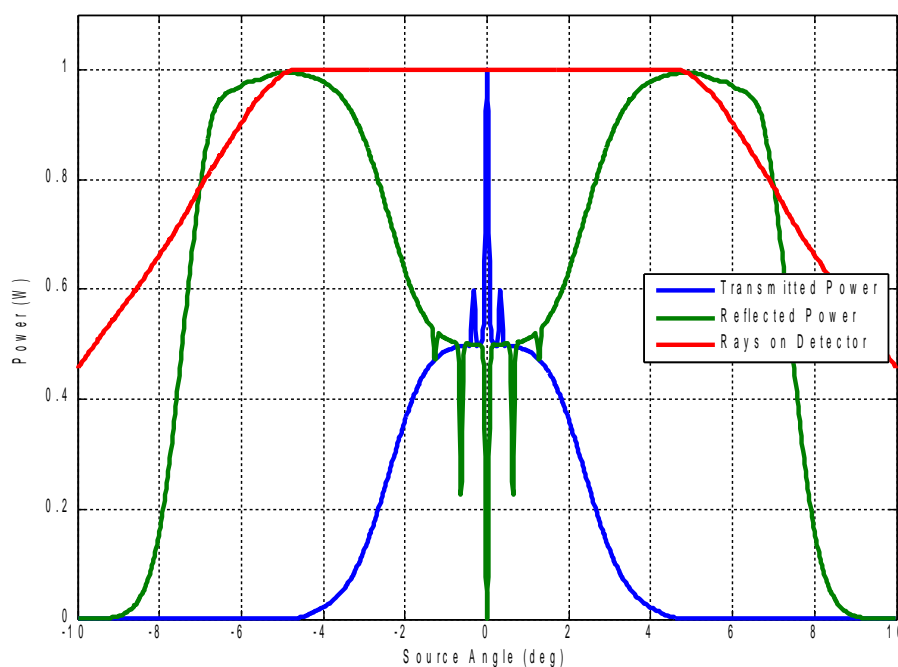


Figure 4-3: The normalized power for the transmitted and reflected channels in the SFPI, for a range of source angles. The ray count is also plotted, and it should be noted that this is identical for both the transmitted and reflected channels.

In figure 4-4, the source is focused onto the SFPI center with a 150mm focal length lens, as described in chapter 2. The central transmitted peak is again indicative of “perfect illumination,” but the range for possible HSRL data is much smaller in this scenario, because the rays on the detector and the transmitted signal drop to zero at approximately ± 0.25 degrees, and 50% of the power is transmitted at an angle of ± 0.05 degrees. This means that in an operational situation, because of the need to focus the source onto the cavity center, the acceptance angle is twenty times smaller than the acceptance angle of the SFPI alone.

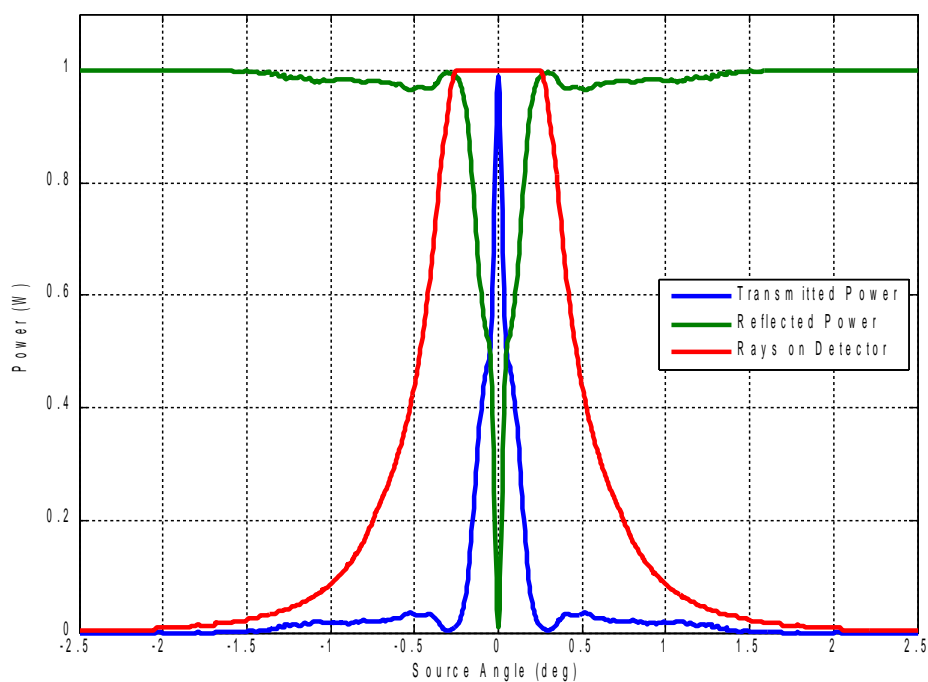


Figure 4-4: The angular dependent normalized power for the transmitted and reflected channels in the SFPI when the beam is focused onto the cavity center. The ray count is also plotted.

The acceptance angle of the WAMI at LaRC was discussed in chapter 3, where it

was found that at an acceptance angle of ± 1 degree, the OPD departs almost 9 waves from the optimal performance, and reaches a maximum departure of 19 waves at an incident angle of ± 1.5 degrees, as shown in figure 4-5. In figure 4-6, the power on each detector for a range of source angles is plotted with the normalized ray count for each detector. When the ray count is 1, 100% of the rays are incident on the detector, and it can be seen that the ray count starts to fall off at ± 1 degree from the center angle. As previously discussed in chapter 3, the center angle marked in this plot is determined by the sum of the WAMI tilt angle of -1 degree (the center of the ray count), and the half-field divergence of the source (0.46 degrees).

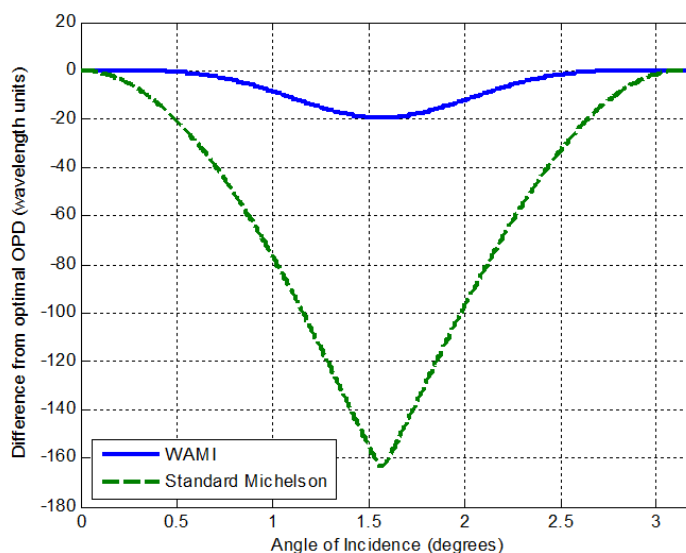


Figure 4-5: The departure from the optimal OPD (in wavelength units) for both a standard Michelson and for the LaRC WAMI.

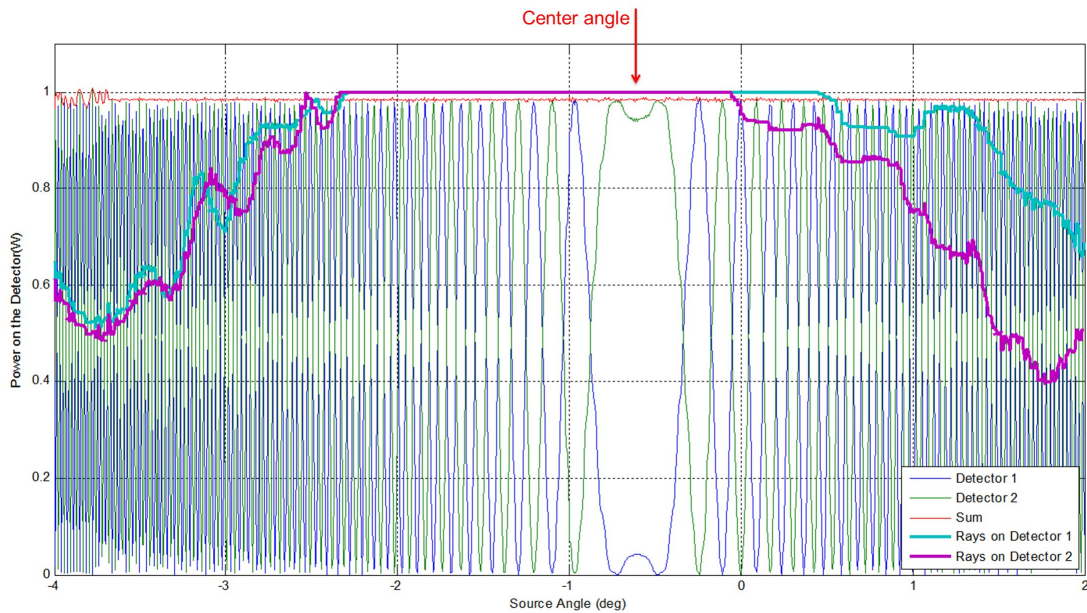


Figure 4-6: The power on each detector for a range of source angles, and the ray count for each detector. The plot is centered on the WAMI tilt angle of -1 degree, and then offset by the half-field divergence of 0.46 degrees.

Both the LaRC WAMI and the MSU SFPI have an acceptance angle of 1 degree. However, when a focal lens is used in conjunction with the SFPI, the acceptance angle drops significantly, and the illumination dramatically affects this value. In contrast, the WAMI will maintain a relatively high transmission for the entire range of acceptance angles, and can be designed to have an even larger acceptance angle, if required.

4.2.3 Efficiency Comparative Analysis

The efficiency of the interferometers was evaluated as a function of the throughput and transmission. The throughput, or etendue, is a measure of the geometric extent of a radiometric system, and can be used in a one-to-one comparison to determine which narrow band filter will theoretically collect more energy. The transmission is a

measure of how much of the incident light passes through the interferometer, and is calculated by taking a ratio of the power before and after the system.

4.2.3.1 Throughput

For a maximally efficient optical system, a lidar should adhere to the “etendue matching condition” (Measures 1984, Abreu 1980) which states that the throughput of the telescope should match the throughput of the narrow band filter, or

$$U = A_T \Omega_T = A_{Filter} \Omega_{Filter} . \quad (4-1)$$

To design a photon efficient HSRL, using a SFPI as a narrow band filter, the specifications should follow the relationship derived in chapter 2:

$$A_T \Omega_T = \frac{\pi^2 L \lambda}{F} , \quad (4-2)$$

where L is the cavity length, λ is the design wavelength, and F is the total finesse of the cavity. For a photon efficient HSRL using a WAMI as a narrow band filter, the specifications should be designed so that

$$A_T \Omega_T = \frac{2\pi^2 h^2}{RP_{WAMI}} , \quad (4-3)$$

as discussed in chapter 3.

The throughput of the SFPI and the WAMI was calculated using equations 4-2 and 4-3, and the WAMI was determined to have a higher throughput. For the MSU SFPI, the throughput is $1.036\text{E-}09 \text{ m}^2$, and for the LaRC WAMI, the throughput is $4.2826\text{e-}09 \text{ m}^2$, meaning that in a one-to-one comparison, the WAMI will theoretically collect more energy than the SFPI.

4.2.3.2 Transmission

The transmission of the interferometers over a range of typical lidar wavelengths is also examined. The comparison of four channels is discussed: the transmitted and reflected channels of the SFPI, and the forward and reverse channels of the WAMI. To obtain the transmission values, the transmission function of each interferometer channel is convolved with the Bruneau model of the backscattered lidar return, as previously described in chapter 3. The transmission functions for both the SFPI and the WAMI are obtained from their respective FRED models. The convolution takes place using the script in Appendix C, modified for the SFPI and then for the WAMI. Four common lidar wavelengths are examined for each of the four channels, and the results are given in table 4-2.

	355 nm	532 nm	1064 nm	632 nm
WAMI Forward Channel	0.98	0.73	0.67	0.014
WAMI Reverse Channel	0.0034	0.26	0.34	1.00
SFPI Transmitted Channel	0.85	0.86	0.29	0.80
SFPI Reflected Channel	0.101	0.11	0.71	0.19

Table 4-2: The transmission of each interferometer channel over a range of wavelengths.

In these calculations, the instruments are “as built” by MSU and NASA LaRC.

For the transmission values in table 4-2, the interferometers are not modified from their “as built” status, meaning that the SFPI was designed for operation at 532nm, and the WAMI designed for operation at 355nm. However, if the interferometers are optimized for the alternative wavelengths before the transmission functions were

measured, a more accurate representation of their operational capabilities at these wavelengths is seen. For this one-to-one comparison of the transmission, both interferometers were modified at a basic level to accommodate the change in design wavelength.

The OPD of the WAMI was adjusted by adapting the length of the glass arm and the wavelength dependent glass index, $n_{1\lambda}$. As derived in chapter 3, the OPD of a WAMI is dependent on the indices and lengths of each interferometer arm, and the incident angle. Assuming an incident angle of zero, the wavelength dependent glass arm length, $d_{1\lambda}$ compensates for the changes in the index, $n_{1\lambda}$, so that

$$d_{1\lambda} = \frac{n_1 d_1}{n_{1\lambda}} \quad (4-4)$$

For each of the four wavelengths selected, the index was adjusted, and the value of

$d_{1\lambda}$ was varied according to equation 4-4. This method was used to adapt the FRED model of the WAMI for use with the alternate wavelengths.

In order to adapt to the alternate wavelengths, the SFPI model was modified so that the finesse was maintained. To do this, the radius of curvature was varied so that it remained equal to an integer number of half-wavelengths, as seen in table 4-3. Because of the confocality of the SFPI, the cavity spacing was also adjusted to be equal with the radius of curvature. The coatings on the mirror were also adjusted so that the reflectivity for each wavelength was 94%. This method was used to adapt the FRED model of the SFPI for use with the alternate wavelengths.

Wavelength (um)	Spacing/ROC (mm)
0.355	9.999995
0.532	10.000004
0.632	10.000136
1.064	10.000004

Table 4-3: Values used to adjust the SFPI model for alternate wavelengths.

The transmissions for the wavelength adjusted interferometers are recorded in table 4-4. For the WAMI, 355nm is still the optimal wavelength with 99% transmission, but the 632nm and 532nm wavelengths also perform well. The WAMI forward and reverse channels are interchangeable with the appropriate system configuration, so having the maximum transmission in the reverse channel for two wavelengths (1064nm and 632nm) is not considered to be an issue. The SFPI maintains a high transmission across this spectral range, but this is assuming ideal illumination, which is impractical, because of the infinitely small aperture necessary for the ideal illumination. Therefore, the realistic maximum transmission for the SFPI is 50%, which is half of the theoretical maximum transmission of 100% for the WAMI.

	355 nm	532 nm	1064 nm	632 nm
WAMI Forward Channel	0.9914	0.9517	0.1145	0.046
WAMI Reverse Channel	0.0069	0.0423	0.8973	0.9868
SFPI Transmitted Channel	0.9959	0.9984	1.0002	0.9988
SFPI Reflected Channel	0.0018	0.0009	0.0002	0.0009

Table 4-4: The transmission of each filter channel over a range of wavelengths. The instruments are wavelength adjusted, and ideal illumination is assumed for the SFPI.

4.2.4 Comparison with the Iodine Vapor Filter

The iodine vapor absorption filter is the current standard for narrow band HSRL filters, and was a significant improvement over the etalons that preceded it (Piironen and Eloranta, 1994). The bandwidth allowed by the 1109 line is approximately 1.8pm at a wavelength of 532nm, so the RP is approximately $2.95E5$ (Piironen and Eloranta, 1994). This is on par with the RP allowed by the WAMI, and less than the RP of the SFPI by two orders of magnitude. By changing the temperature of the absorption cell, the transmission of the iodine vapor filter varies from 0.08% to 60%, which can be compared with the theoretical maximum transmission values of 100% (50%) for the WAMI (SFPI) (Piironen and Eloranta, 1994). The acceptance angle of the iodine vapor filter would depend on the construction of the absorption cell, and that comparison is outside of the scope of this research. Ultimately, while the iodine vapor filter has performed well at 532nm, there is a desire for HSRL data at additional wavelengths. The iodine vapor filter is limited by the absorption line locations, and cannot be adjusted for a multi-spectral HSRL.

4.3. Design Methodology for a Narrow Band Filter in a HSRL

In order to select and design the optimal narrow band filter for a HSRL, three criteria are considered: the spectral performance, the angular performance, and the efficiency. Two interferometers were analyzed for this application; at the time of this writing, both are operating successfully in two separate HSRL systems. The SFPI at MSU is part of a ground based HSRL, which is itself part of a larger deployment of

aerosol detection instrumentation in Montana (Repasky 2011, Nehrir 2011). The WAMI at NASA LaRC is incorporated into a second generation airborne HSRL, with an ultimate goal of implementing a space-based HSRL for global monitoring of aerosols. The fact that these two instruments are both successfully using an interferometric narrow band filter demonstrates that these interferometers can be used in a wide variety of measurement situations if they are properly designed and implemented.

This research has narrowed the design criteria down to three critical specifications: the spectral RP, the acceptance angle, and the efficiency. In order to select the optimal interferometer for use as the narrow band filter in a HSRL, several design questions are asked and answered in this section with respect to the two interferometers that have been analyzed.

4.3.1 Specifying the Narrow Band Filter

In order to select a narrow band filter for a HSRL, the following questions should be considered:

- a) Over what spectral range will the system operate, and what RP is necessary? Is the science best served by removing the Mie or the Rayleigh signal from the lidar back-scattered return? The science goal of the HSRL will decide this question. This is further discussed in section 4.3.2.
- b) What platform and range will the HSRL require? Is this a ground based system, airborne, or space-based? Will a low overlap be necessary, or is long range data more desirable for the science goals? The necessary acceptance angle is

determined by these questions. This is further discussed in section 4.3.3.

- c) What are the operating conditions? The background light levels will determine the possible SNR, which will decide the throughput specifications. This is further discussed in section 4.3.4.

By answering these questions about the ultimate application, a designer can narrow down the options for an interferometric filter for a HSRL, using the comparison criteria laid out in this research: the spectral, angular, and throughput requirements. A list of specifications for consideration is presented below for both the SFPI and the WAMI in tables 4-5 and 4-6. These specifications can determine the operational capabilities of a SFPI or a WAMI, and should be carefully considered at the outset of a multi-spectral HSRL design.

SFPI Candidate List of Specifications
Spectral Parameters:
Central Wavelength
Wavelength Band
Source Parameters:
Beam size at entrance pupil
Beam location at entrance pupil
Beam divergence at entrance pupil
Multi-mode or single-mode
Coating Parameters:
Reflectivity/Absorption/Transmission
Polarization
Spectral bandwidth
SFPI Geometrical Parameters:
Radius of Curvature
Mirror Spacing
Mirror material (index)
Mirror Thickness
System Parameters:
Aperture of following optical surface on transmission side
Location of following optical surface on transmission side
Quantum Efficiency of detector

Table 4-5: A list of candidate specifications for the design of a SFPI.

WAMI Candidate List of Specifications
Spectral Parameters:
Central Wavelength
Wavelength Band
Source Parameters:
Beam size at entrance pupil
Beam location at entrance pupil
Beam divergence at entrance pupil
Multi-mode or single-mode
Coating Parameters:
Reflectivity/Absorption/Transmission
Polarization
Spectral bandwidth
WAMI Geometrical Parameters:
Glass Arm Material
Glass Arm Length
Air Arm Material
Air Arm Length
System Parameters:
Incident angle of source on the WAMI
Separation of the reverse channel from the incident beam
Detector Quantum Efficiency
Source Divergence

Table 4-6: A list of candidate specifications for the design of a WAMI.

4.3.2 Spectral Design Methodology

The primary function of a narrow band filter in a HSRL is to spectrally separate the Mie and Rayleigh backscattered lidar signal. There are two methods of accomplishing this. First, the Mie signal can be removed from the total return, and this filtered result can be used in conjunction with the total return to obtain the spectrally separate result inherent in HSRL data. This is illustrated in figure 4-21-A below, and is

the current favored method for practical reasons, one of which is that the Rayleigh lidar return is well understood and easily modeled, so that the notch in the signal can be easily modeled. The Mie return is not as well understood. The second option is to remove the Rayleigh signal from the total lidar return using a bandpass filter centered on the Mie signal. This filtered result can be used with the total return to obtain the spectrally separate HSRL data. This second option is illustrated in figure 4-21-B. Both the MSU SFPI and the LaRC WAMI eliminate the Mie return from the total lidar return (option A), but either filtering option is theoretically possible, and the decision is a primary spectral design decision for a HSRL.

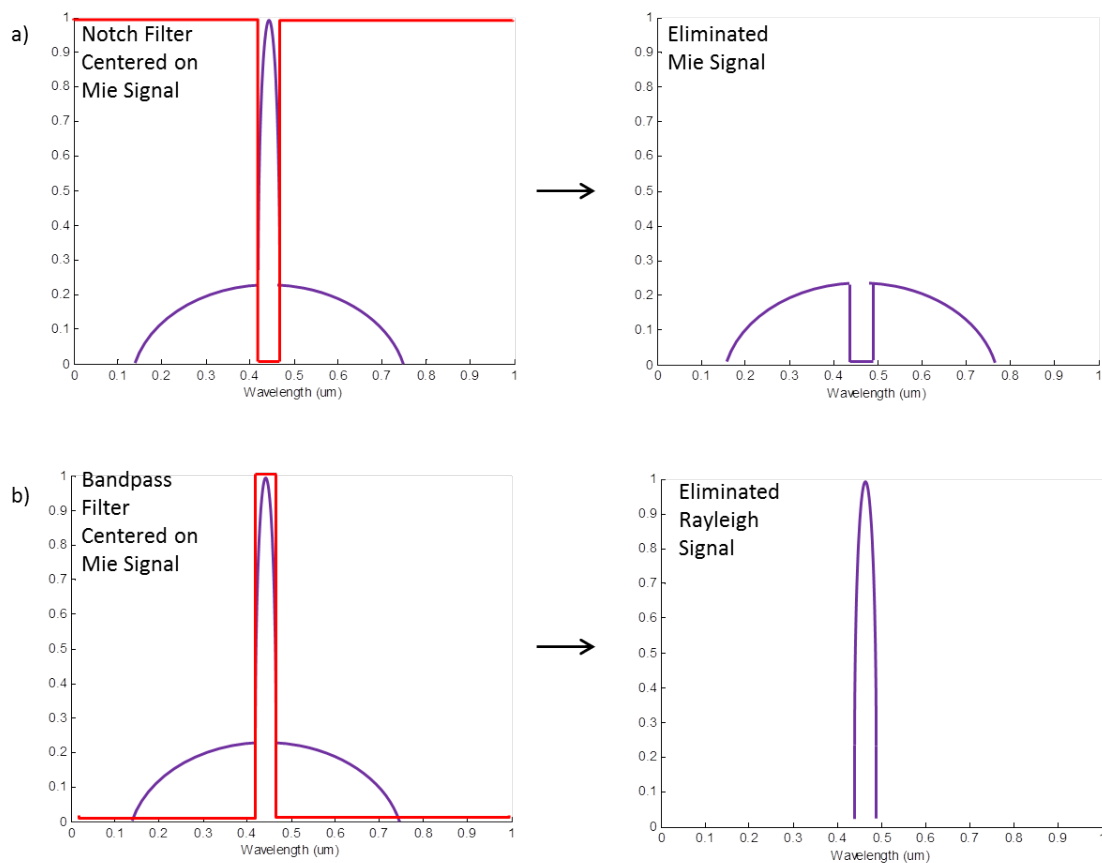


Figure 4-7: Illustration of the two possible directions for the narrow band HSRL filter to take. Figure A shows the elimination of the Mie signal from the total lidar return using a notch filter, and figure A shows the elimination of the Rayleigh signal from the total lidar return using a bandpass filter. Both the MSU SFPI and the LaRC WAMI use the method in figure A.

Once it is determined which signal (Mie or Rayleigh) will be removed from the total filtered lidar return, the central design wavelength and the necessary RP must be determined. For the purposes of this analysis, it is assumed that the Mie signal is removed from the total lidar return, because the Rayleigh curves are well understood and that allows for more straightforward lidar algorithms. Additionally, this is how both the SFPI and the WAMI are used in the MSU and LaRC HSRL systems. The level at which

the signal is removed from the system must also be considered, because no method will completely remove the Mie signal from the lidar return. Generally a $1/e^2$ filtering level is assumed, but other options can be considered, and the necessary bandwidth to remove the Mie signal at a specified level for a range of wavelengths is illustrated in figure 4-8. To remove all but 1% of the Mie signal, at the largest considered wavelength, a 3.5pm bandwidth is necessary. A range of these values for several common lidar wavelengths is shown in table 4-7.

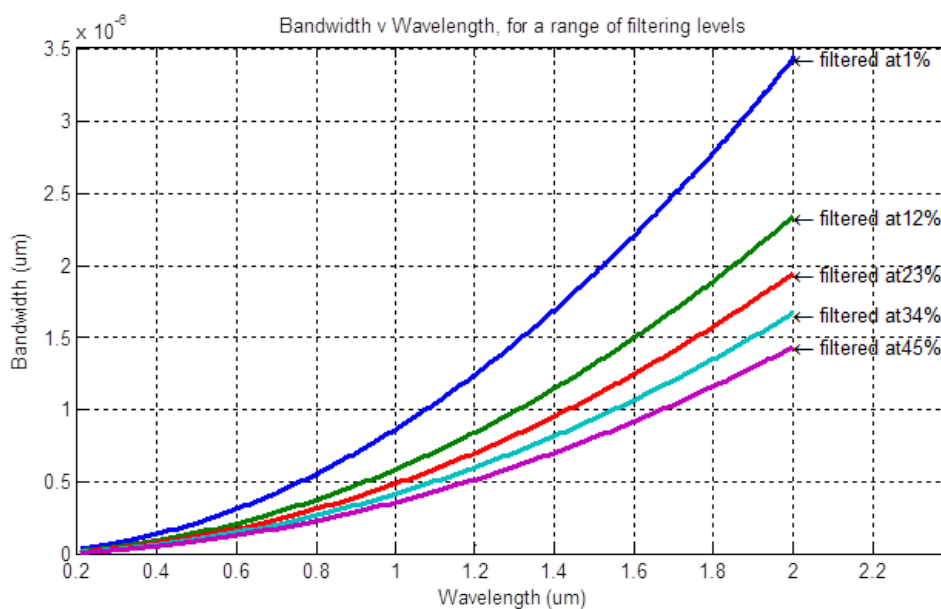


Figure 4-8: The wavelength dependent bandwidth necessary to remove the Mie signal from a HSRL return, for a range of filtering levels.

Wavelength	Bandwidth (um)
355 nm	1.08 e-07 @ 1%
	7.2 e-08 @ 12%
	4.4 e-08 @45%
532 nm	2.4 e-07 @1%
	1.6 e-07 @ 12%
	1.0 e-07 @45%
633 nm	3.4 e-07 @1%
	2.3 e-07 @ 12%
	1.4 e-07 @45%
1064 nm	9.7 e-07 @1%
	6.6 e-07 @ 12%
	4.04 e-07 @45%

Table 4-7: The bandwidth at certain filtering levels for common lidar wavelengths.

4.3.2.1 SFPI Spectral Design Methodology

In order to design a SFPI for a specified RP, which is the ratio of the wavelength and bandwidth, certain factors must be considered. Primarily, the radius of curvature, the cavity spacing and the reflectivity of the inner cavity surfaces will determine the operational capabilities of a SFPI. The RP for a SFPI directly depends on the total finesse of the cavity, the radius of curvature, and the design wavelength, as shown in equation 2-23. The total finesse is derived in chapter 2, and is found in equation 2-18. The RP of a SFPI has a quadratic dependence on the reflectivity of the mirror, and there is a multiplicative effect from the radius of curvature (ROC) of the mirrors (which is also the cavity separation in these confocal interferometers). Figure 4-9 shows the effect of the reflectivity on the RP for a range of mirror radii at a design wavelength of 355nm.

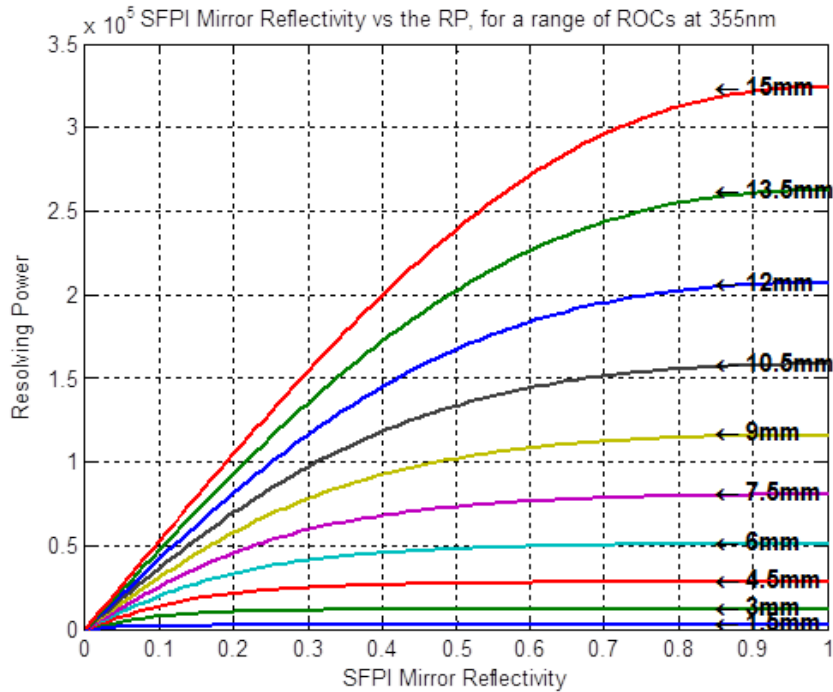


Figure 4-9: The reflectivity dependent RP, for a SFPI operating at 355nm, for a range of mirror radius of curvatures.

The RP has an inverse dependence on the central wavelength. The reflectivity dependent RP is plotted for a range of design wavelengths in figure 4-10, where an ROC of 1cm is used.

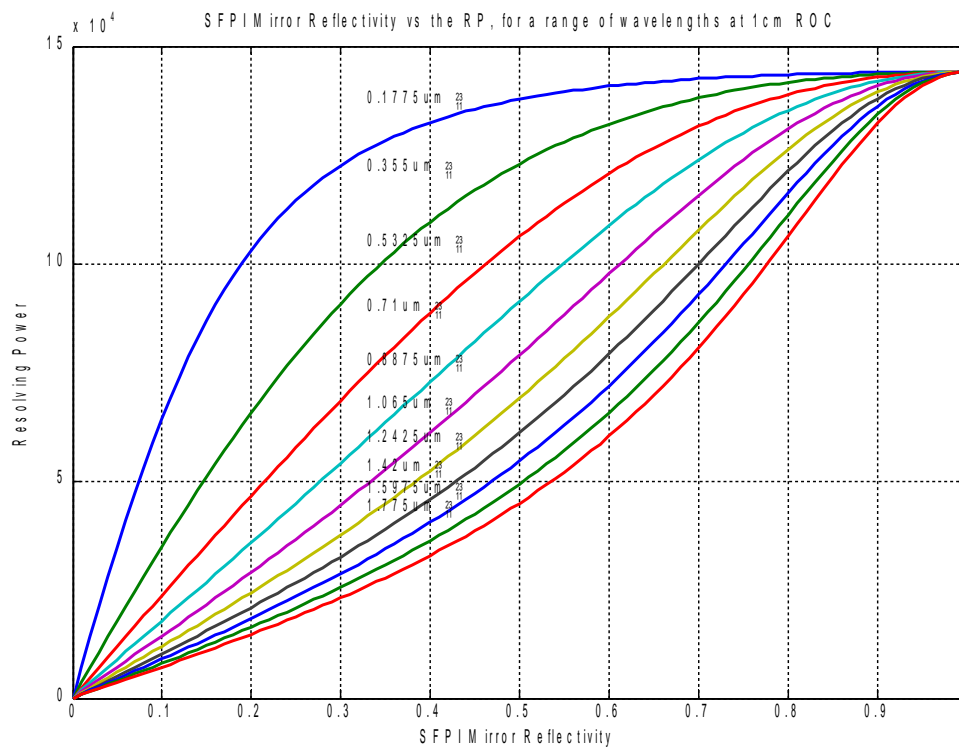


Figure 4-10: The SFPI RP for a range of wavelengths and mirror reflectivity values.

4.3.2.2 WAMI Spectral Design Methodology

The RP of a WAMI is dependent on the design wavelength, and the OPD of the interferometer, as seen in equation 3-13. The OPD for a WAMI, found in equation 3-4, shows the dependence of the RP on several geometrical factors, including the indices and lengths of each interferometer arm. The incident angle also affects the RP, but if it is a smaller angle, it is a minor factor. The dependence of the RP on the design wavelength for a range of glass arm lengths, is shown in figure 4-11. If the length of the air arm length is varied, a similar trend is seen.

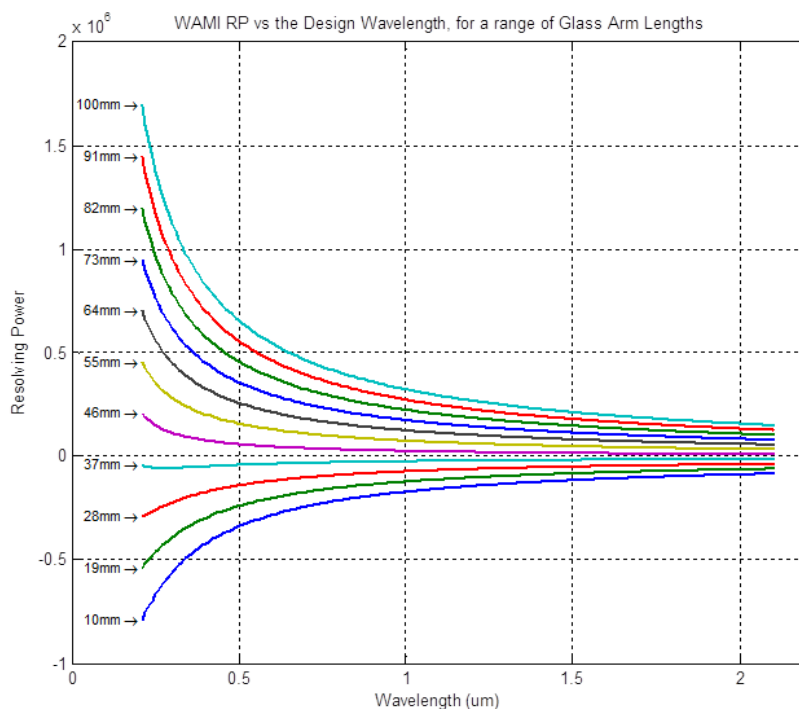


Figure 4-11: The wavelength dependent WAMI RP for a range of glass arm lengths.

The indices of refraction of the two WAMI arms are another critical design decision. The air arm of the WAMI can be filled with air, or a glass with a lower index of refraction can be used, depending on the needs of the system. For example, the LaRC WAMI is contained in a cell with a monitored index of refraction of 1.00027. An alternative gas could be used in this cell to change the spectral performance of the WAMI. To investigate this, the wavelength dependent RP of a WAMI is shown in figure 4-12, for a range of indices in the air arm.

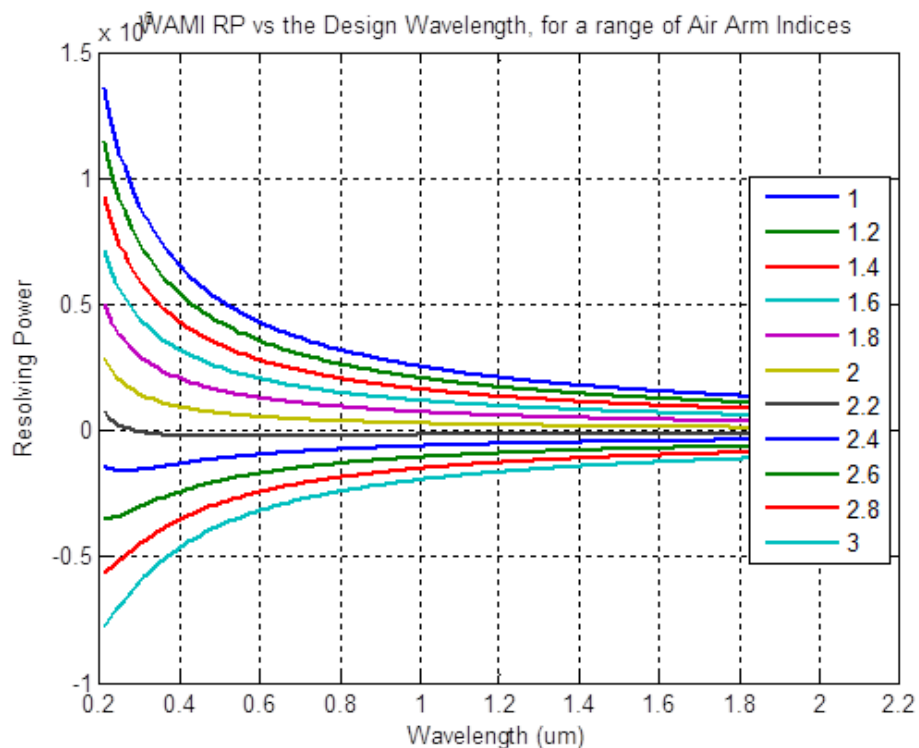


Figure 4-12: The wavelength dependent WAMI RP for a range of air arm indices of refraction.

As seen in equation 3-4, the incident angle does not greatly affect the OPD, or the RP, because it is generally more practical to have a smaller angle of incidence on the WAMI.

4.3.2.3 Summary of Spectral Design Methodology

In order to determine which interferometer will have a better spectral performance as the narrow band filter in a HSRL, several critical factors should be considered. Primarily, the necessary bandwidth and design wavelength, which determine the necessary RP, must be determined. Once that is decided upon, the specifications of the specific interferometer can be considered. For a SFPI, the ROC, the cavity spacing, and

the reflectivity of the mirror coatings are primary factors. For a WAMI, the indices and length of each arm are the primary considerations, and the incident angle can also have an effect. Figure 4-13 illustrates this design method, and tables 4-8 and 4-9 indicate the general optimization trends of the design specifications for each interferometer.

Spectral Design

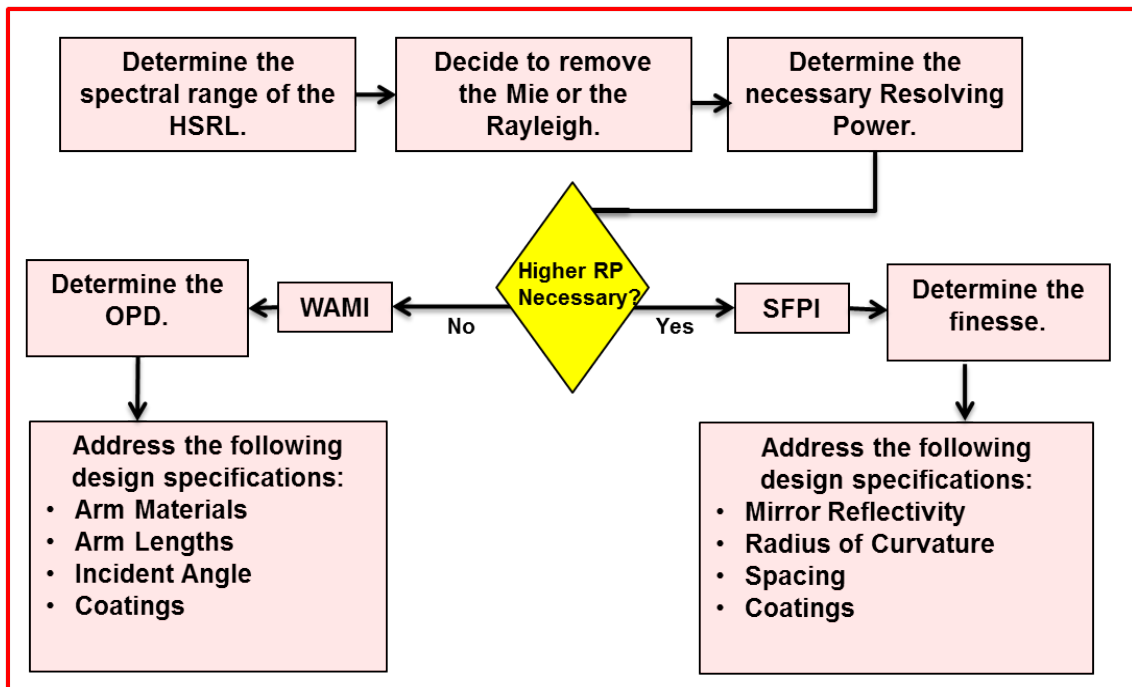


Figure 4-13: Flow chart showing the spectral design methodology discussed in section 4.3.2.

SFPI Specification	Action to increase RP
Finesse	Increase
ROC	Increase
Wavelength	Decrease
Incident Angle	Decrease
Source height	Decrease
Mirror Reflectivity	Increase

Table 4-8: The trend of optimization for an increase RP using a SFPI.

WAMI Specification	Action to increase RP
OPD	Increase
Wavelength	Decrease
Air Arm Length, $d1^*$	Decrease
Air Arm Index, $n1^*$	Decrease
Glass Arm Length, $d2^*$	Increase
Glass Arm Index, $n2^*$	Increase
Incident Angle	Decrease

Table 4-9: The trend of optimization for an increase RP using a WAMI. The starred () specifications have the caveat that the aforementioned QZP be maintained.*

4.3.3 Angular Design Methodology

The lidar range required for the science application of a HSRL plays a critical role in the necessary acceptance angle of the narrow band filter, and should be carefully considered. Because of the large range, the acceptance angle for a space based HSRL must be larger than that intended for a ground based system. This is why the lidar team at NASA LaRC placed a large importance on the acceptance angle of their narrow band filter, and is one reason that they ultimately used a WAMI after considering a standard

Michelson interferometer. Another possibility for consideration is the need for shorter range HSRL data, which would require full overlap to occur at a shorter range, which also requires a wider acceptance angle.

4.3.3.1 SFPI Angular Design Methodology

The acceptance angle of the SFPI depends on the science purposes of the HSRL; to design for a specific acceptance angle will require consideration of several factors. This analysis examined the total acceptance angle, not simply the angular range as determined by fiber parameters. The SFPI maintains a high transmission for a small window of acceptance angles. One factor in the acceptance angle of the SFPI is the use of a lens to place the beam's focal point in the cavity center. The focal length of this lens will affect the cone of light that is incident on the SFPI, which in turn affects the transmission levels. As illustrated in figure 4-14, with a shorter focal length, the SFPI will accept a larger angle. The shorter focal length allows the lens to be closer to the SFPI, creating a smaller f-number. The longer focal length creates a system that operates with a small window of acceptance angles.

The “angular window,” or the full field acceptance angle, for each focal length at several transmission levels is shown in table 4-10. If it assumed that a 50% transmission rate is effective for a SFPI operating in a HSRL, the acceptance angles then range from 0.04 degrees to 0.6 degrees (using focal lengths from 200mm to 50mm, respectively).

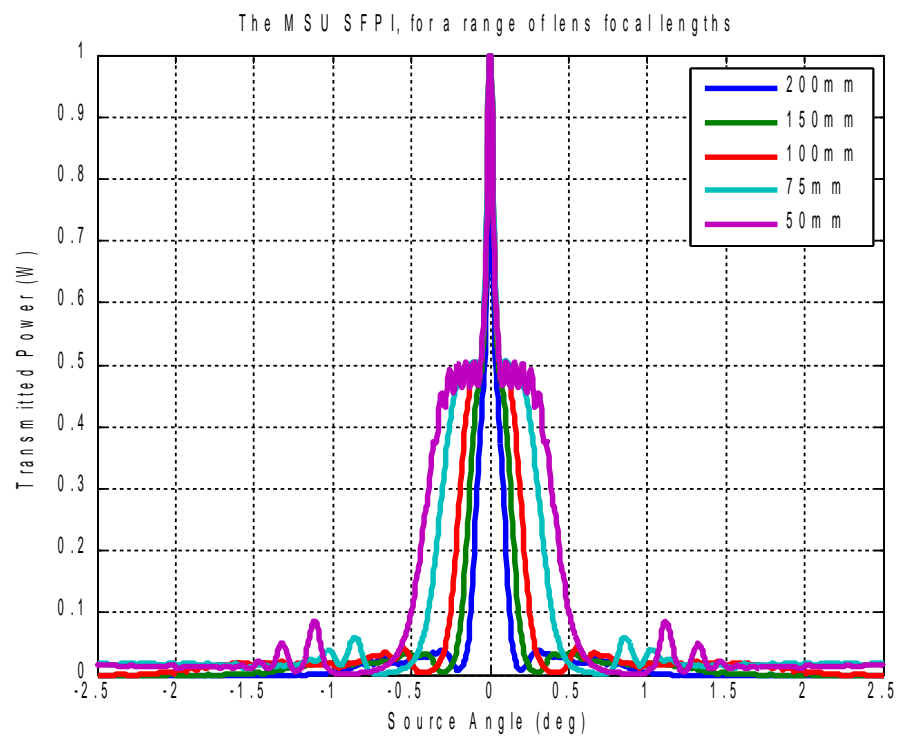


Figure 4-14: The angle dependent, normalized power transmitted through a SFPI. The beam is focused into the center of the SFPI with a lens, and plots are included for a range of focal lengths.

Focal Length (mm)	Angular Window at 50% Transmission
50	+/- 0.3 degrees
75	+/- 0.13 degrees
100	+/- 0.06 degrees
150	+/- 0.05 degrees
200	+/- 0.02 degrees
	Angular Window at 75% Transmission
50	+/- 0.03 degrees
75	+/- 0.02 degrees
100	+/- 0.02 degrees
150	+/- 0.02 degrees
200	+/- 0.0125 degrees
	Angular Window at 90% Transmission
50	+/- 0.0175 degrees
75	+/- 0.0125 degrees
100	+/- 0.0125 degrees
150	+/- 0.0125 degrees
200	+/- 0.0025 degrees

Table 4-10: The angular window for transmission levels of a SFPI , for a range of focal lengths.

The location of the source with respect to the optical axis of the lens and SFPI is also an important design consideration. As discussed in chapter 2, an off-axis source causes the beam to be incident with the SFPI at a larger distance from the optical axis, which affects the transmission. For a reasonable angle, the maximum transmission will drop to 50%, and the “angular window” will become smaller. This is illustrated in figure 4-15, where the trend can be observed as the source is moved further off axis. The influence of the incident angle on the SFPI transmission is shown for a) a source that is on-axis, b) a source that 1/2mm off axis, and c) a source that is 5mm off axis.

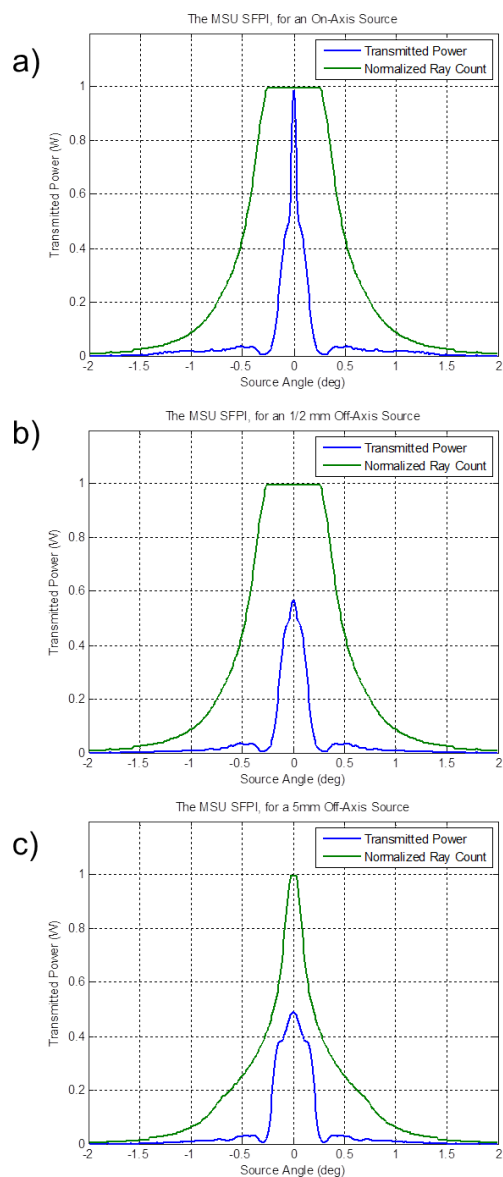


Figure 4-15: The effect of the incident angle on the SFPI transmission, for a) a source that is on-axis, b) a source that 1/2mm off axis, and c) a source that is 5mm off axis.

Another factor for consideration in the design of a SFPI is the effect of the acceptance angle on the finesse, which directly impacts the RP and is impacted by the wavelength. Figure 4-16 shows the influence of the acceptance angle on the finesse and wavelength. There are certain angles that will produce a larger finesse, which will enhance the spectral performance of the SFPI, but these angles are too large to be practical.

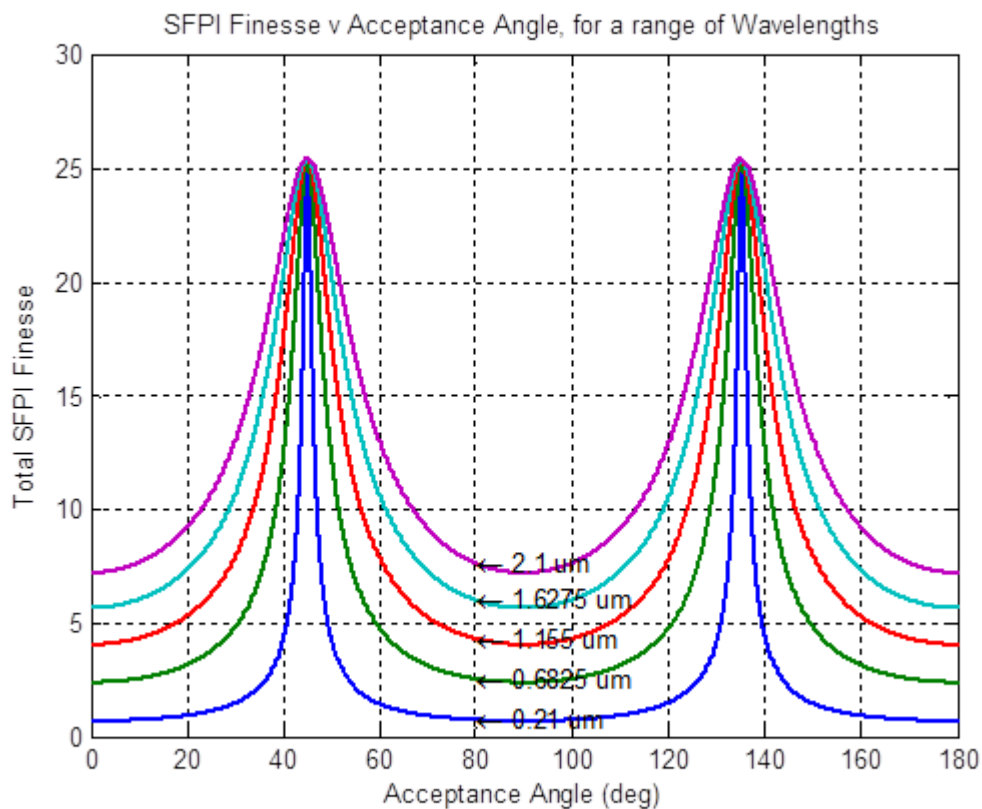


Figure 4-16: The total angular dependent SFPI finesse, for a range of wavelengths.

To design a SFPI for a specific acceptance angle, the focal length of the lens used to focus the beam into the cavity center is a critical factor. The acceptance angle is also affected by the design wavelength, and the departure of the source from the optical axis

when it is incident on the lens.

4.3.3.2 WAMI Angular Design Methodology

The acceptance angle of the WAMI depends on several factors. The construction of the WAMI, including the length and indices of both arms, and the source divergence are considered here.

The dependence of the acceptance angle on the geometric factors of the WAMI is considered. The OPD departs from the optimal values at cyclical locations, as shown in figures 4-17 and 4-18. In these figures, the angular dependent OPD is plotted for a range of WAMI factors. Figure 4-17 and 4-18 show the trend for the arm lengths of the WAMI: the longer glass arm lengths and the shorter air arm lengths cause a larger OPD. Figure 4-19 shows the dependence of the angular dependent OPD on the index of the air arm. The specifications for the LaRC WAMI are used for the unmentioned variables in these figures.

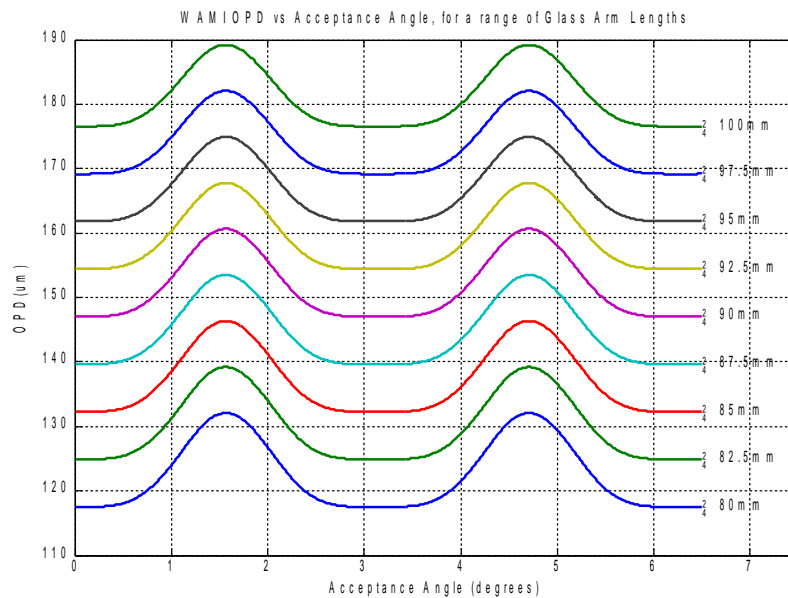


Figure 4-17: The angular dependent WAMI OPD, for a range of glass arm lengths.

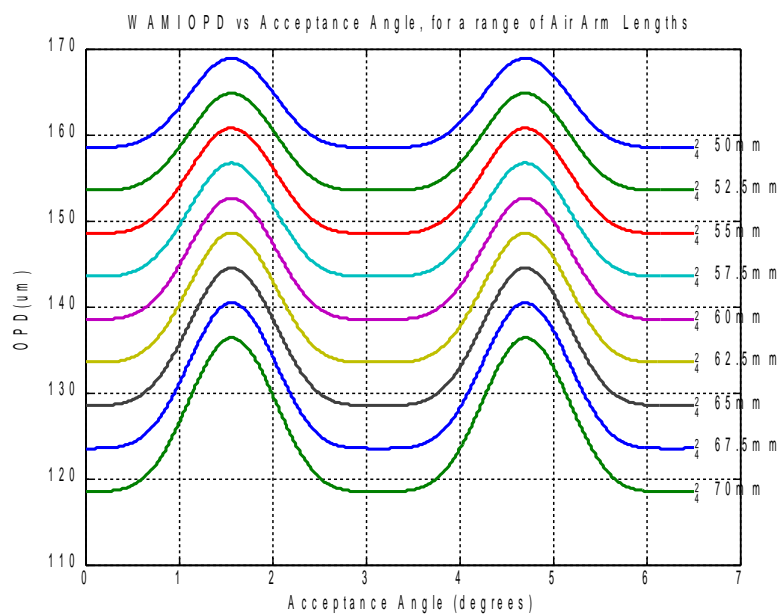


Figure 4-18: The angular dependent WAMI OPD, for a range of air arm lengths.

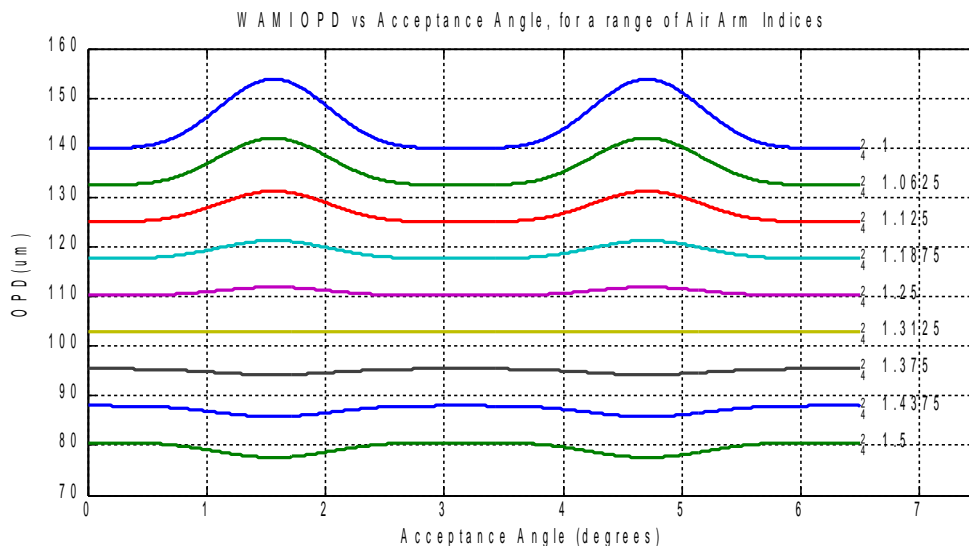


Figure 4-19: The angular dependent WAMI OPD, for a range of air arm indices.

Two factors, the source divergence and the incident angle, must be balanced in order to maintain the efficiency of the WAMI. As originally discussed in chapter 3, the divergence of the source angle effects the shift of this central peak from the WAMI tilt angle by the value of the half-field divergence. As the central peak shifts away from the center of the ray count, the beam is walking towards the edge of the detectors, as shown by the decrease in the ray count. This trend is shown in figures 3-22 and 4-20, where the half-field divergence of the source is 0.46, and 0.9 degrees, respectively, and the central peak is shifted by this amount from the WAMI tilt of -1 degree. The divergence would become a problem as the rays start to walk off the detector, which occurs in figure 4-20, as the divergence exceeds the acceptance angle.

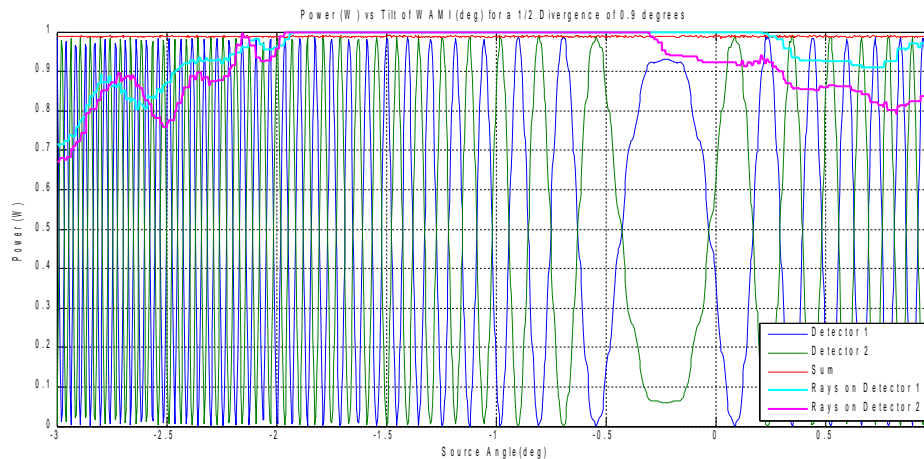


Figure 4-20: The power on each detector for a range of source angles, and the ray count for the respective detectors. For the LaRC WAMI, with a half field source divergence of 0.9 degrees, and a tilt of -1 degrees.

4.3.3.3 Summary of Angular Design Methodology

This section discussed factors that need to be considered when designing a SFPI or a WAMI to have a specific acceptance angle, and figure 4-21 illustrates this process. Tables 4-11 and 4-12 show the general optimization trends for the design specifications. For the SFPI, the focal length of the lens, the design wavelength, and the type of illumination will determine what acceptance angle is possible. The WAMI angular performance depends on the source divergence as well as the arm lengths and indices of the instrument.

Angular Design

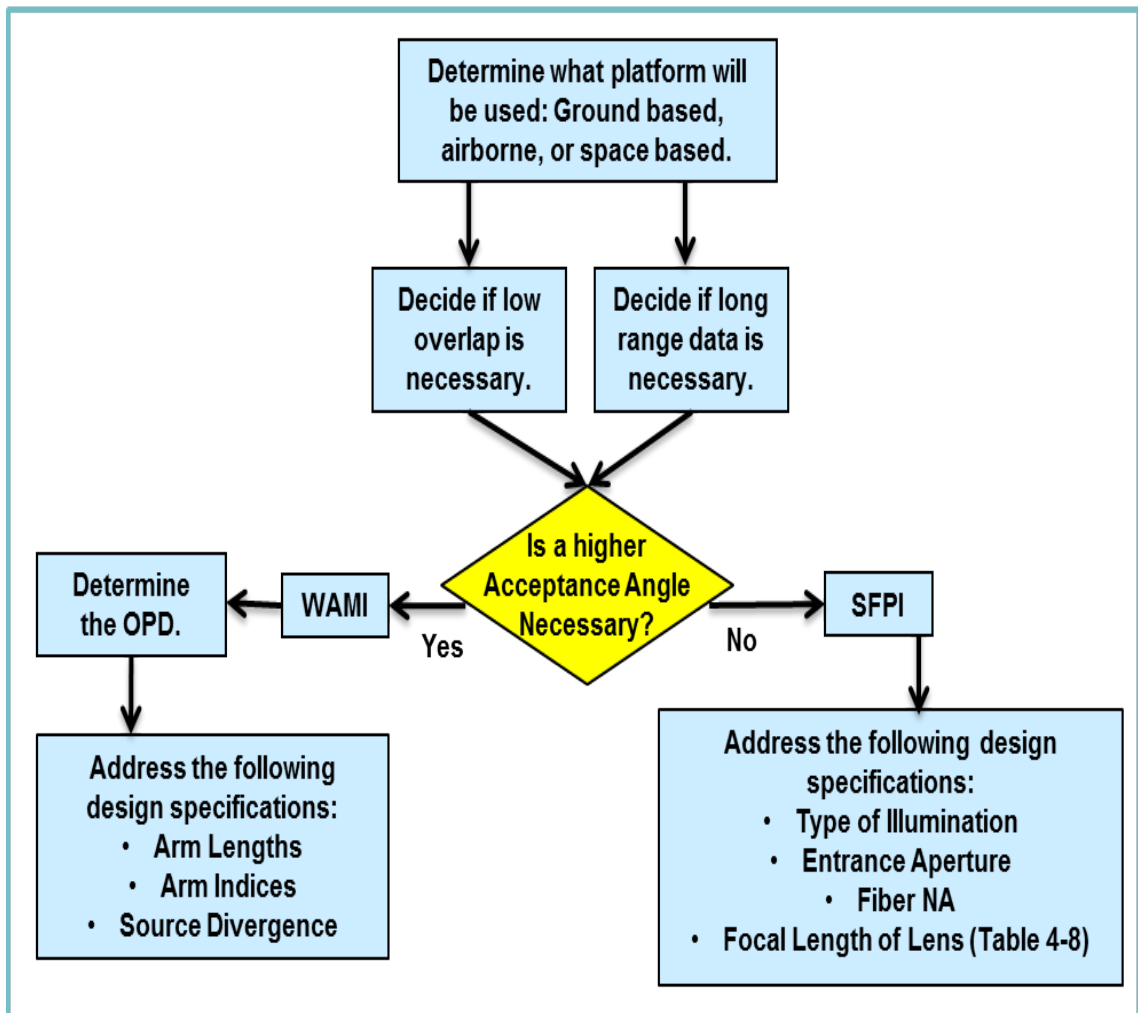


Figure 4-21: Flow chart showing the angular design methodology discussed in section 4.3.3.

SFPI Specification	Action to increase θ
Focal Length	Decrease
Finesse	Increase
ROC	Increase
Wavelength	Increase
Mirror Reflectivity	Increase
Source height	Decrease

Table 4-11: The trend of optimization for an increased acceptance angle using a SFPI.

WAMI Specification	Action to increase θ
Source Divergence	Decrease
OPD	Increase
Wavelength	Decrease
Air Arm Length, $d1^*$	Decrease
Air Arm Index, $n1^*$	Decrease
Glass Arm Length, $d2^*$	Increase
Glass Arm Index, $n2^*$	Increase

Table 4-12: The trend of optimization for an increase in the acceptance angle using a WAMI. The starred () specifications have the caveat that the aforementioned QZP be maintained.*

4.3.4 Efficiency Design Methodology

The efficiency of the narrow band filter in a HSRL is an important consideration because of the low light levels in most lidar systems. To evaluate the necessary efficiency for a particular HSRL, the desired SNR must be considered. There is a proportional relationship between the optical efficiency and the SNR,

$$SNR = \frac{\eta}{h\nu} \int_{c(t-r)/2}^{ct/2} \frac{P(t, R)}{B_N(R) SRF(R)} dR \quad (4-5)$$

where η is the optical efficiency, $h\nu$ is the photon energy, $B_N(R)$ is the filter bandwidth, R is the lidar range, t is the time since the start of the pulse, and SRF is the signal reduction factor (Bilbro et al. 1986).

This section describes how to design a SFPI and a WAMI for maximum efficiency, using the throughput and the transmission as metrics.

4.3.4.1 SFPI Design for Efficiency

The throughput and the transmission of the SFPI should be maximized for the best efficiency, and they both depend on the finesse of the interferometer. The throughput is straightforward to calculate, and was derived in chapter 2 to be

$$U_{SFPI} = \frac{\pi^2 L \lambda}{F}, \quad (4-6)$$

where L is the spacing between the cavity mirrors, F is the total finesse, and λ is the design wavelength. The transmission is dependent on a range of factors, primarily the illumination incident on the cavity. Because the ideal illumination is impractical (because it requires an infinitely small aperture), a transmission of 50% is the best case scenario. This depends on the design wavelength, the source location and the finesse. Following are several plots that illustrate the dependence of the throughput and transmission on the finesse, the design wavelength, the cavity spacing and the reflectivity of the mirror coatings.

Figure 4-22 shows the dependence of the throughput on the total finesse and cavity spacings. There is a trend of a larger cavity spacing producing a higher throughput. For a cavity that is an order of magnitude larger than the value of the MSU

SFPI (from 10mm to 100mm), there is a throughput increase of 0.1899 mm^2 .

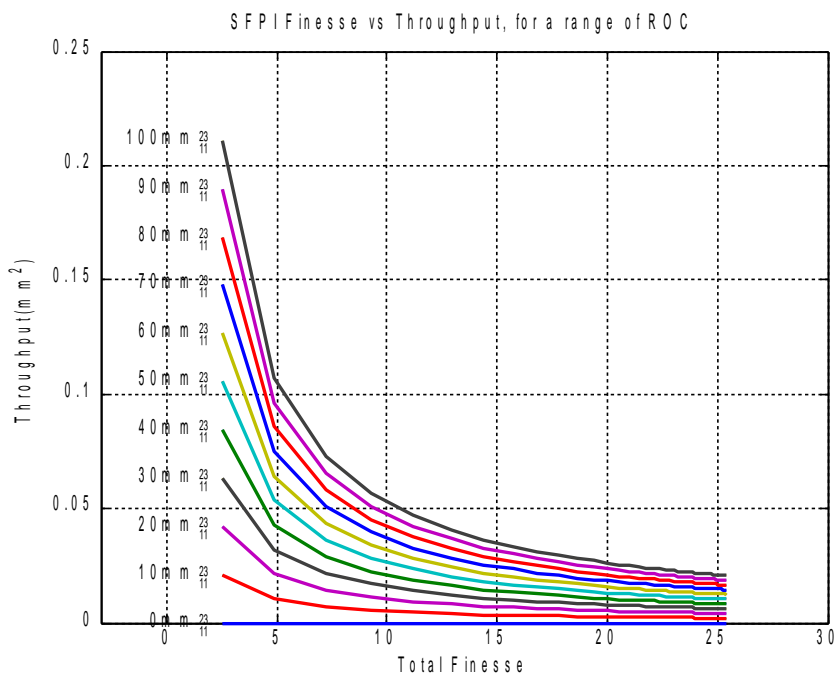


Figure 4-22: The SFPI Throughput vs the finesse, for a range of possible cavity spacings.

As has been previously addressed in chapter 2, the maximum transmission for a realistic SFPI is 50%. Figure 4-23 illustrates the progression that occurs in the angular dependent transmitted power as the source moves off axis. In this case, the off-axis source is serving to create a non-ideal illumination in the FRED model. It can be observed that the transmission doesn't drop below 50% until the ray count also drops off, indicating that the rays are no longer incident on the detector. Therefore the drop-off in power occurs because of geometric limitations, and if these are suitably addressed in a SFPI design, the transmission efficiency can be maintained at 50% for a reasonable window.

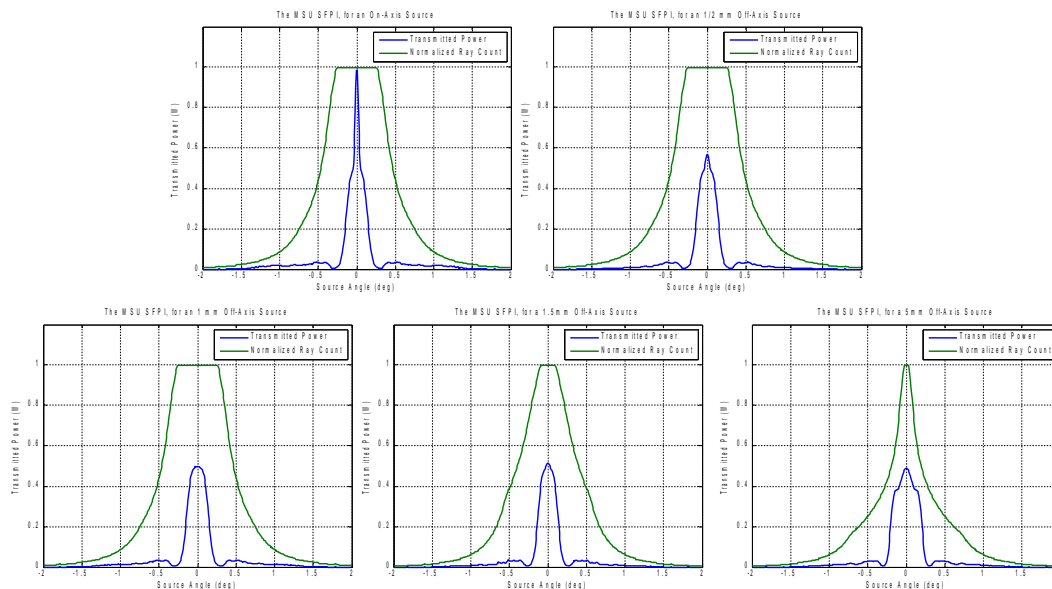


Figure 4-23: The transmitted SFPI power and ray count for a source that is on axis, 0.5mm off axis, 1mm off axis, 1.5mm off axis, and 5mm off axis (from left to right and top to bottom).

4.3.4.2 WAMI Design for Efficiency

The throughput and the transmission of the WAMI should be maximized for the best efficiency, and they both depend on the OPD of the interferometer. The throughput is straightforward to calculate. It is dependent on the OPD (equation 3-4), which is used to calculate the RP (equation 3-13). The RP is then combined with the radius of the WAMI entrance aperture, h , to find the throughput (equation 3-15). The throughput of the WAMI versus the OPD is plotted in figure 4-24, for a range of glass arm lengths, where it's seen that the OPD and the throughput are inversely proportional.

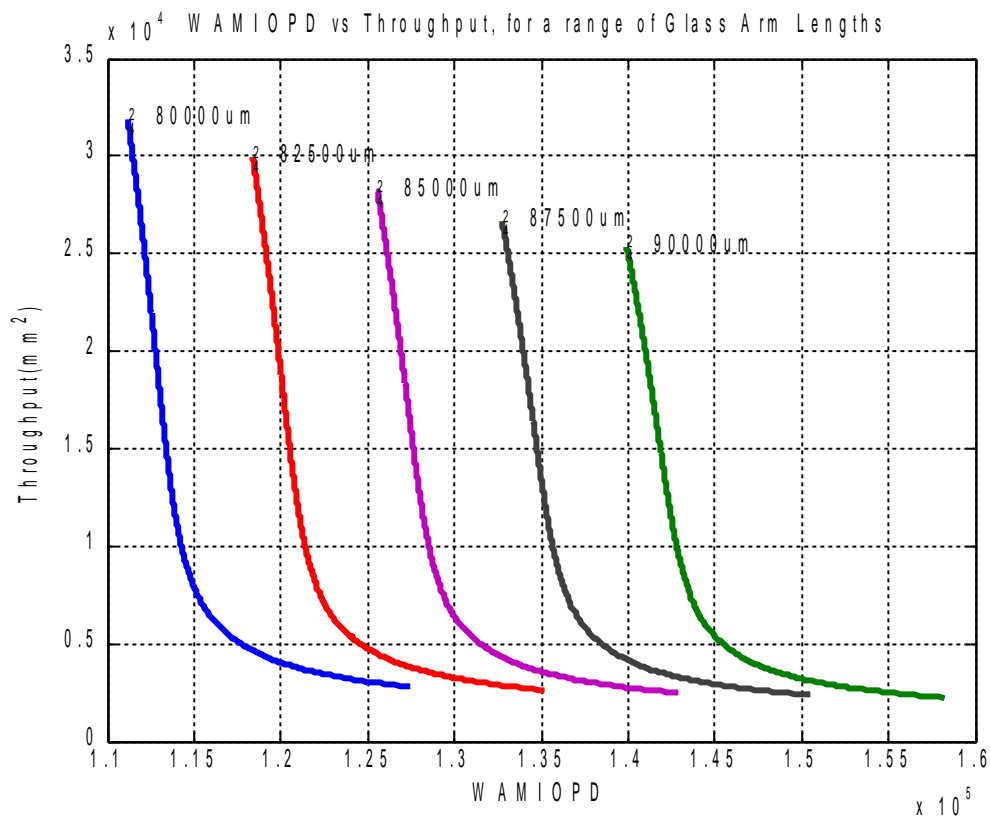


Figure 4-24: The WAMI throughput versus the OPD, for a range of glass arm lengths.

The transmission functions of the WAMI were first discussed in chapter 3, and the equations for the two WAMI channels are seen in equation 3-10. Only the first transmission function, T_1 , is examined here, because T_2 complements it. Figure 4-25 shows the dependence of this transmission on the wavelength and on the length of the glass arm. There are separate curves for each arm length, and they converge at the design wavelength of 355nm. As shown here, the theoretical maximum transmission for each WAMI channel is 100%.

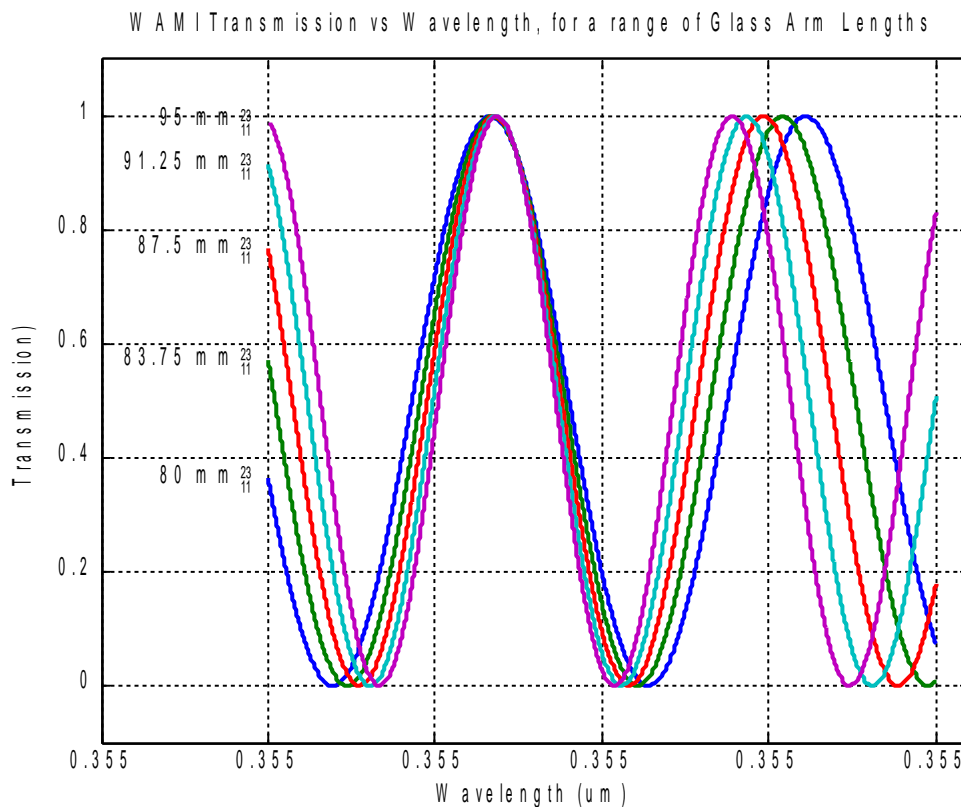


Figure 4-25: The WAMI wavelength dependent transmission function, for a range of glass arm lengths.

4.3.4.3 Summary of Efficiency Design Methodology

Design methods to maximize the efficiency of a SFPI and a WAMI acting as the narrow band filter in a HSRL are discussed in this section. The throughput and the maximum transmission of each interferometer are examined, and the primary factors for consideration include the SFPI finesse and the WAMI OPD. The design process to maximize efficiency is illustrated in figure 4-26, and the optimization trends for the throughput are shown in tables 4-13 and 4-14.

Efficiency Design

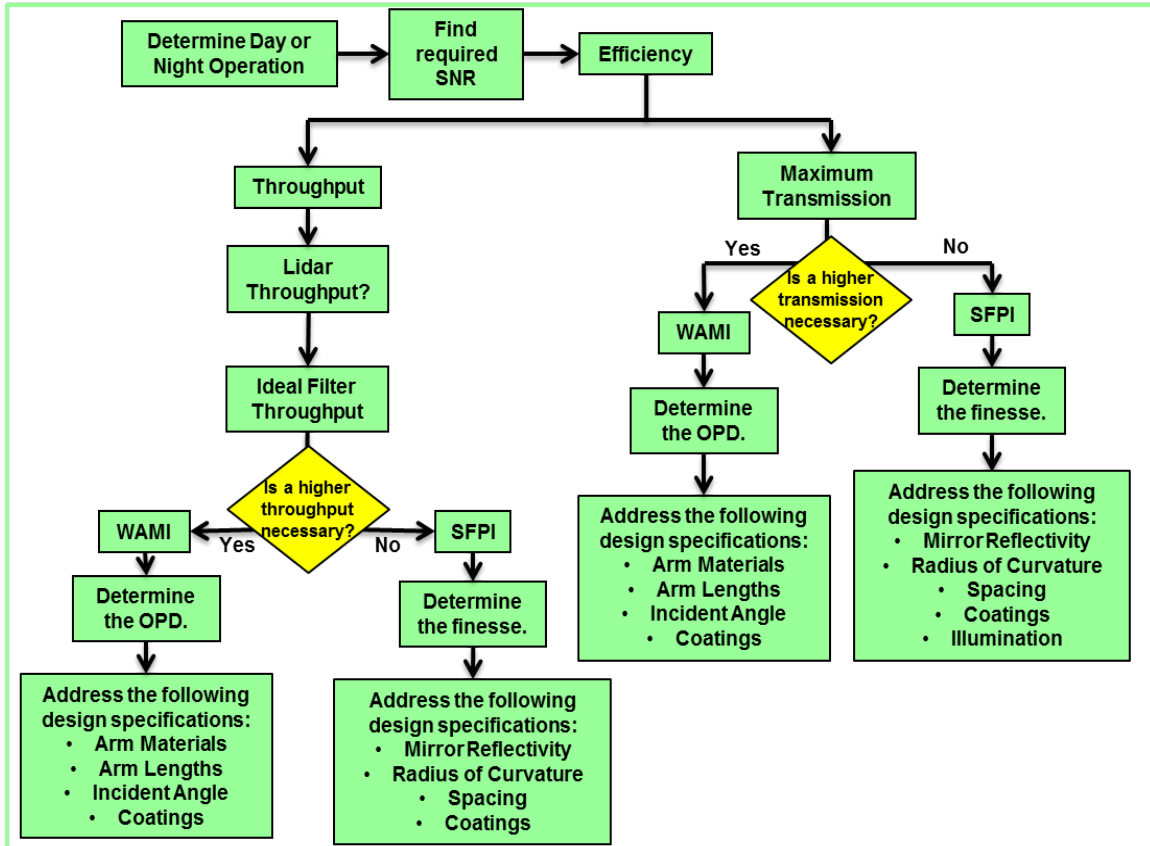


Figure 4-26: Flow chart showing the efficiency design methodology discussed in section 4.3.4.

SFPI Specification	Action to increase θ
Mirror Spacing	Increase
Finesse*	Decrease
ROC	Increase
Wavelength	Increase
Mirror Reflectivity	Increase
Source height	Decrease

Table 4-13: The trend of optimization for an increased throughput using a SFPI. A balance between the RP and throughput is found at 70% of the initial RP (Connes 1956, Vaughn 1989).

WAMI Specification	Action to increase θ
RP	Decrease
OPD	Decrease
Wavelength	Increase
Air Arm Length, $d1^*$	Decrease
Air Arm Index, $n1^*$	Decrease
Glass Arm Length, $d2^*$	Increase
Glass Arm Index, $n2^*$	Increase

Table 4-14: The trend of optimization for an increase in the throughput using a WAMI. The starred () specifications have the caveat that the aforementioned QZP be maintained.*

4.3.5 Summary of Design Methodology

This section has addressed the necessary criteria to consider when specifying a SFPI or a WAMI as the narrow band filter in a HSRL. In order to select the best interferometer for a specific purpose, several questions were addressed:

- a) First, the spectral range and the necessary RP were determined, and the factors

that affect the RP of the SFPI and the WAMI were discussed. The possibility of removing either the Mie or Rayleigh signal from the total lidar return was addressed.

- b) Second, the effect of the HSRL platform on the filter requirements was discussed, and the factors that affect the acceptance angle of the SFPI and the WAMI were addressed. It was determined that the WAMI is capable of larger acceptance angles than the SFPI.
- c) Third, the need to determine the required SNR was addressed, which determines the necessary throughput and transmission.

These three comparison criteria, when combined, address the many design considerations for a narrow band filter in a HSRL, and can be carefully considered for any optical design.

4.4 Summary

This chapter includes a comprehensive comparison of the SFPI and the WAMI performance as the narrow band filter in a HSRL. The interferometers were evaluated on three comparison criteria: the specular performance, the angular performance, and the efficiency. The metrics used for these comparison criteria were the RP, the acceptance angle, the throughput, and the transmission. A design methodology was included, where the factors that affect these design metrics were addressed for the SFPI and the WAMI.

CHAPTER 5: CONCLUSIONS AND FUTURE WORK

5.1 Conclusions

The goal of this dissertation was to develop a generalized methodology for the design of narrow band filters in multi-spectral HSRL systems. This goal was approached by completing a comprehensive comparative analyses of two interferometers currently being used for this purpose, and the creation of a design tool based on three criteria: the spectral, angular, and efficiency performance of each interferometer.

Chapter 1 provided background on the motivation behind this research, and presented information on lidar and HSRL technologies. Additionally, two models for the lidar backscattered return were presented: the simple Gaussian model and the Bruneau model. It was shown that, despite some differences in how they were generated, each model provides a realistic representation of the backscattered Mie and Rayleigh signal that is incident on a HSRL, and both models were used in the analyses of the SFPI and the WAMI.

In chapter 2, the SFPI at MSU was described and analyzed, and the total finesse was determined to be a primary metric. For larger beam sizes incident on the cavity, the maximum transmission and the acceptance angle were significantly reduced due to the finesse from spherical aberration. Additionally, it was concluded that Zemax is not an appropriate tool for this analysis, due to its inability to accurately trace coherent rays while maintaining energy conservation.

Chapter 3 examined and analyzed the WAMI at NASA LaRC. The OPD is a primary metric for the WAMI performance, and depends primarily on the construction of the interferometer. The transmission function of the WAMI was critical in analyzing its performance, and was found using the FRED model, and verified using a model described by Bruneau et al. in 2003.

Chapter 4 includes a comparison of the results from these two analyses, and a design methodology for future interferometric HSRL narrow band filters. Spectral, angular, and efficiency considerations were discussed, and methods were presented that maximize the performance of a SFPI or a WAMI.

In closing, this dissertation accomplishes the following goals:

- (1) Verified non-sequential models of a SFPI and a WAMI were presented, which offer a vehicle for further analysis, including diffractive and interferometric effects.
- (2) A comprehensive analysis of the performance of the SFPI and the WAMI as the HSRL narrow band filter was presented, along with detailed comparisons between the spectral, angular, and efficiency capabilities of each.
- (3) A generalized design methodology for a narrow band HSRL filter, based on the analysis of the SFPI and the WAMI, was presented. This methodology includes a list of specifications for consideration, and enumerates their effect on the filter performance.

5.2 Future Work

Further research into interferometric filters used in multi-spectral HSRL systems would benefit the field of lidar research. This research developed a methodology for designing a narrow band HSRL filter based on two options currently in use. Additional interferometers should be examined, as well as exploring non-interferometric options. A comprehensive analysis of additional filtering options could streamline the HSRL design process, resulting in improved and more versatile HSRL systems that could ultimately enhance our understanding of atmospheric aerosols.

Additional future work includes several next steps in HSRL capabilities. The possibility of a HSRL combined with a Micro-Pulse Lidar (MPL) has been discussed with Dr. John Reagan (personal communication, January 26, 2009), and could combine the cost-effectiveness of the MPL with the superior HSRL data product. A HSRL using a holographic narrow band filter has also been discussed with Dr. Erich de Leon and John Brownlee (private conversation), of the University of Arizona Photonics Systems Lab. Theoretically, significant improvements to the HSRL narrow band filter are possible, but further analysis of the holographic filtering capabilities is necessary (de Leon, 2012).

Appendix A

The Matlab code used to generate the Simple Gaussian Lidar Return Model.

```

%Plots simple Doppler broadened lidar returns, modeled using a SIMPLE
%GAUSSIAN and the FWHM for the Mie and Rayleigh signals, found in Liu,
%2012.

clc;
clear all;
close all;

%Some useful constants
c = 299792458000000;           %speed of light (um/s)
peakscale = 4;                 %the divisor for the ratio btwn the Mie
and Rayleigh returns

%Wavelength
w0 = 0.355;                    %central wavelength in um
wdelta = 0.000005;            %Deviation to max and min from central
wavelength
wmin = w0-wdelta;              %Minimum wavelength examined
wmax = w0+wdelta;              %Maximum wavelength examined
wstep = 0.00000001;           %step size for wavelength range
w = wmin:wstep:wmax;           %Wavelength range for analysis

%Mie Distribution
FWHMmf = 100000000;            %Mie FWHM, in Hz
FWHMmw = (FWHMmf.*w0^2)/c ;    %Mie FWHM, in um
cm = FWHMmw/(2*sqrt(2*log(2)));
bm = w0;                        %central value of Gaussian
am = 1;                          %normalized maximum value of Gaussian
Gm = am.*exp((- (w-bm).^2)./(2*cm.^2)); %Mie signal, in simple gaussian
form

%Rayleigh Distribution
FWHMrf = 3000000000;           %Rayleigh FWHM, in Hz
FWHMrw = (FWHMrf.*w0^2)/c ;    %Rayleigh FWHM, in um
cr = FWHMrw/(2*sqrt(2*log(2)));
br = w0;                          %central value of Gaussian
ar = am/peakscale;              %normalized maximum value of
Gaussian
Gr = ar.*exp((- (w-br).^2)./(2*cr.^2)); %Mie signal, in simple gaussian
form
Total = Gr+Gm;

%Normalize to 1
MaxTotal = max(Total);
TotalNorm = Total./MaxTotal;

```

```
%Plot
figure (1)
plot(w,TotalNorm)
title('Mie and Rayleigh Returns Modeled with Simple Gaussians: 355 nm');
xlabel('Wavelength (um)')
ylabel('Normalized Irradiance')
grid on
```

Appendix B

The Matlab code used to generate the Bruneau Lidar Return Model.

```

%Plots the doppler broadened lidar returns, modeled using the method
%described in Bruneau, 2001 and Bruneau 2003.
clc;
clear all;
close all;

%Some useful constants
k = 1.3806503*10^-11;      %Boltzmann constant ((um^2 kg)/(K s^2))
T = 250;                  %system temperature (Kelvin)
c = 299792458000000;     %speed of light (um/s)
res = 3000;               %number of sample points
linewidthscale = 75;
Rb = 1.05;                %The Backscatter Ratio

%Wavelength
w0 = 0.355;               %central wavelength in um
wdelta = 0.000001;       %Deviation to max and min from central
wavelength
wmin = w0-wdelta;        %Minimum wavelength examined
wmax = w0+wdelta;        %Maximum wavelength examined
wstep = (wmax-wmin)/(res-1); %step size for wavelength range
w = wmin:wstep:wmax;     %Wavelength range for analysis

%WaveNumber
sc = 1/w0;                %Wavenumber for central wavelength (m^-1)
smax = 1/wmin;           %remember, this is 1/wmin
smin = 1/wmax;           %remember, this is 1/wmax
sstep = (smax-smin)/(res-1); %step size for wavenumber range
s = smin:sstep:smax;     %Wavenumber range

%Solve for molecular mass
gmtest = 7.1e-6;         %the molecular linewidth (1/e HWHM in units of
um^-1)
m = (2*sc/c)^2*((2*k*T)/gmtest^2);
%average mass of atmospheric molecule, found using previous values and
EQ 5.

%calculation of the molecular and particulate linewidth (1/e HWHM in
units of m^-1)
scale = 4;                %scale btwn molecular and particulate linewidth
gm = ((2*sc)/c)*((2*k*T)/m)^(1/2); %the molecular linewidth (1/e HWHM
in units of m^-1)
gp = gm./linewidthscale; %the particulate linewidth (1/e HWHM
in units of m^-1)

%Calculate the frequency dependent gaussian return for molecular and

```

```
particulate signal:
Im = (1/(gm*sqrt(pi))).*exp(-((s-sc).^2)./gm.^2);
Ip = (1./(gp.*sqrt(pi))).*exp(-((s-sc).^2)./gp.^2);
Ia = (1/Rb)*Im + ((Rb-1)/Rb) * Ip;
%Normalize to 1
Max = max(Ia);
Ianorm = Ia/Max;

%Plot the Total Irradiance vs the wavelength
figure(1)
plot(w,Ianorm)
xlabel('Wavelength(um)')
ylabel('Normalized Irradiance')
grid on
title('Mie and Rayleigh Returns Modeled Using Bruneau 2003')
```

Appendix C

The Matlab code used to generate the Bruneau Transmission Functions for a WAMI lidar: (Bruneau2001v3)

```

%WAMI: This follows the procedure in Bruneau 2001 for convolving an
incident
%irradiance with the transmission of an interferometer path to see the
%signal incident on a detector - EQ 4-5.

clc;
clear all;
close all;

%Some useful constants
res = 3000; %number of sample points
B1 = 0.6961663; %Sellmeir coefficients for fused silica,
from
http://cvmellesgriot.com/products/Documents/Catalog/Dispersion\_Equations.pdf
B2 = 0.4079426;
B3 = 0.8974794;
C1 = 0.00467914826;
C2 = 0.0135120631;
C3 = 97.9340025;
q = .1; %the sensitivity of the detectors, taken
from HSRL 1 detector's QE.
peakscale = 4; %the divisor for the ratio btwn the Mie
and Rayleigh returns
theta = 1;

%Wavelength
w0 = 0.355; %central wavelength in um
wdelta = 0.000001; %Deviation to max and min from central
wavelength
wmin = w0-wdelta; %Minimum wavelength examined
wmax = w0+wdelta; %Maximum wavelength examined
wstep = (wmax-wmin)/(res-1); %step size for wavelength range
w = wmin:wstep:wmax; %Wavelength range for analysis

%Wavelength Range for Convolution
wstepcon = (wmax-wmin)/(res*2-1-1); %For the convolutions using
Bruneau
wcon = wmin:wstepcon:wmax;
wstepconF = (wmax-wmin)/(5998-1); %For the convolution using the
FRED model
wconF = wmin:wstepconF:wmax;

%WaveNumber
sc = 1/w0; %Wavenumber for central wavelength (m^-1)

```

```

smax = 1/wmin;           %remember, this is 1/wmin
smin = 1/wmax;           %remember, this is 1/wmax
sstep = (smax-smin)/(res-1); %step size for wavenumber range
s = smin:sstep:smax;     %Wavenumber range

%Define indices of refraction in WAMI:
n1 = sqrt(1 + B1*(1./s).^2./((1./s).^2.-C1) + B2.*(1./s).^2./
((1./s).^2.-C2) + B3.*(1./s).^2./((1./s).^2.-C3));
ncentral = sqrt(1 + B1*(1./sc).^2./((1./sc).^2.-C1) + B2.*(1./sc).^2./
((1./sc).^2.-C2) + B3.*(1./sc).^2./((1./sc).^2.-C3));
%Wavelength dependent index for fused silica:
n2 = 1.00027;           %index for air in WAMI

%Define WAMI arm lengths
d1 = 87578;             %Glass arm length, in um
d2 = 59318;             %Air arm length, in um

%OPD of WAMI at LaRC
OPD = 2*(n1*d1 - n2*d2) - (sin(theta).^4/4)*(d1./n1.^3 - d2/n2^3) -
(sin(theta).^6/8)*(d1./n1.^5 - d2/n2^5);
OPDCentral = 2*(ncentral*d1 - n2*d2) - (sin(theta)^4/4)*(d1/ncentral^3 -
d2/n2^3) - (sin(theta)^6/8)*(d1/ncentral^5 - d2/n2^5);

%Define Transmission Functions of interferometer arms
T2 = 0.5 - 0.5.*cos(2.*(pi.*(s.*OPD))); %used a trig ID for sin^2
T1 = 0.5 + 0.5.*cos(2.*(pi.*(s.*OPD))); %used a trig ID for cos^2

%Calling other functions
MieRayleighPlot_Bruneau2003_V2 %Calls incident irradiance, modeled
from Bruneau (Ianorm)
MieRayleighPlot_simple_V3 %Calls incident irradiance, modeled
from Gaussians (TotalNorm)
FREDWavelengthWAMI %Calls transmission modeled in FRED
using 355Michelsonv4.FRD

%Calculate convolution to see signal on the detector using Simplified
Gauss
%and Bruneau Transmission Model
S1Gauss = q*conv(TotalNorm, T1);
S2Gauss = q*conv(TotalNorm, T2);

%Calculate convolution to see signal on detector using Bruneau return
Model
%and Bruneau Transmission Model
S1Bru = q*conv(Ianorm, T1);
S2Bru = q*conv(Ianorm, T2);

%Calculate convolution to see signal on the detector using Simplified
%Gauss and FRED Transmission Model
S1GaussFRED = q*conv(TotalNorm, Det1);
S2GaussFRED = q*conv(TotalNorm, Det2);

```

```

%Calculate convolution to see signal on detector using Bruneau return
Model
%and FRED Transmission Model
S1BruFRED = q*conv(Ianorm, Det1);
S2BruFRED = q*conv(Ianorm, Det2);

%Integrate under each curve for the Signals in order to get a single
value.
int1 = trapz(wcon, S1Bru);
int2 = trapz(wcon, S2Bru);
int3 = trapz(wconF, S1BruFRED);
int4 = trapz(wconF, S2BruFRED);
int5 = trapz(wcon, S1Gauss);
int6 = trapz(wcon, S2Gauss);
int7 = trapz(wconF, S1GaussFRED);
int8 = trapz(wconF, S2GaussFRED);
BARSignal = [int1 int2; int3 int4; int5 int6; int7 int8];
S1meanInt = (int1+int3+int5+int7)/4;
yS1meanInt = [S1meanInt S1meanInt S1meanInt S1meanInt S1meanInt
S1meanInt];
S2meanInt = (int2+int4+int6+int8)/4;
yS2meanInt = [S2meanInt S2meanInt S2meanInt S2meanInt S2meanInt
S2meanInt];
xInt = (0:1:5);

%Calculating the differences in integration above
IntA1 = int1 - int5;
IntA2 = int2 - int6;
IntB1 = int3 - int7;
IntB2 = int4 - int8;
IntC1 = int1 - int3;
IntC2 = int2 - int4;
IntD1 = int5 - int7;
IntD2 = int6 - int8;
ReturnDiff = (IntA1 +IntA2+ IntB1 +IntB2)/4;
TXDiff = (IntC1 +IntC2 +IntD1 +IntD2)/4;

%Calculate the Resolving Power
width = (2*sqrt(log(2)))/(pi)
RP = 2*(1/width)*OPDCentral

%Plot the Total Irradiance vs the wavelength
figure(1)
plot(w,Ianorm)
xlabel('Wavelength(um)')
ylabel('Normalized Irradiance')
grid on
title('Mie and Rayleigh Returns Modeled Using Bruneau 2003')

%Plot Results in one simple plot

```

```

figure (2)
plot(w,TotalNorm)
title('Mie and Rayleigh Returns Modeled with Simple Gaussians');
xlabel('Wavelength (um)')
ylabel('Normalized Irradiance')
grid on

%Plot the WAMI Transmission through 2 paths, from Bruneau model
figure(3)
plot(w,T1,w,T2)
title('Transmission through Paths in Interferometer, using Bruneau 2003
Model');
xlabel('Wavelength (um)')
ylabel('Transmission')
leg = legend ('Detector 1', 'Detector 2');
set(leg, 'Location', 'SouthEast');
grid on

%Plot the WAMI Transmission through 2 paths, from FRED
figure(22);
plot(Wavelength, Det1, Wavelength, Det2);
title ('Transmission through Paths in Interferometer, using FRED
Model');
xlabel('Wavelength(um)');
ylabel('Transmission');
leg = legend ('Detector 1', 'Detector 2');
set(leg, 'Location', 'SouthEast');
grid on;

%Plot the Signal on Detectors using Simplified Gauss return model and
Bruneau
%Transmission Function
figure(5)
plot(wcon,S1Gauss, wcon, S2Gauss)
title('Simple Gaussian Return & Bruneau Transmission Function');
xlabel('Wavelength (um)')
ylabel('Signal')
grid on
legend('Signal 1', 'Signal 2')

%Plot the Signal on Detectors using Bruneau return model and Bruneau
%Transmission Function
figure(6)
plot(wcon,S1Bru, wcon, S2Bru)
title('Bruneau Return & Bruneau Transmission Function');
xlabel('Wavelength (um)')
ylabel('Signal')
grid on
legend('Signal 1', 'Signal 2')

%Plot the Signal on Detectors using Simplified Gaussian return model and

```

```

%FRED Transmission Function
figure(7)
plot(wconF,S1GaussFRED, wconF, S2GaussFRED)
title('Simple Gaussian Return & FRED Transmission Function');
xlabel('Wavelength (um)')
ylabel('Signal')
grid on
legend('Signal 1', 'Signal 2')

%Plot the Signal on Detectors using Bruneau return model and
%FRED Transmission Function
figure(8)
plot(wconF,S1BruFRED, wconF, S2BruFRED)
title('Bruneau Return & FRED Transmission Function');
xlabel('Wavelength (um)')
ylabel('Signal')
grid on
legend('Signal 1', 'Signal 2')

%Plot a comparison of the total signal for each method using the
%integration of all previous signal plots
figure(10)
bar(BARSignal)
hold on
plot(xInt, yS1meanInt, xInt, yS2meanInt, '--');
colormap gray
grid on;
xlabel('1=Bruneau x Bruneau, 2=Bruneau x FRED, 3=Gauss x Bruneau,
4=Gauss x FRED')
ylabel('Signal on the detector');
leg2 = legend ('Signal 1', 'Signal 2', 'Average Signal 1', 'Average
Signal 2');
set(leg2, 'Location', 'SouthEast');
title('Integrated Signal for 4 Scenarios')

```

Appendix D

An alphabetical list of acronyms used in this dissertation.

AR	Anti-Reflection
CTE	Coefficient of Thermal Expansion
FOV	Field of View
FSR	Free Spectral Range
FWHM	Full-width Half-maximum
HR	High Reflection
HSRL	High Spectral Resolution Lidar
LaRC	Langley Research Center
Lidar	Llght Detection And Ranging
MI	Michelson Interferometer
MPL	Micro-Pulse Lidar
MSU	Montana State University
OPD	Optical Path Difference
PFPI	Planar Fabry-Perot Interferometer
PPP	Plane Parallel Plate
QZP	Quasi-Zero Position
ROC	Radius of Curvature
RP	Resolving Power
SFPI	Spherical Fabry-Perot Interferometer
SNR	Signal-to-Noise Ratio
WAMI	Wide-Angle Michelson Interferometer

REFERENCES

- 1) Antireflection Coatings [CVI Laser Optics: BBAR-Series Coatings]. Retrieved April 9, 2013, from <https://www.cvimellesgriot.com/Products/Documents/GeneralInfo/AntireflectionCoatings.pdf>.
- 2) Bilbro, James W., DiMarzio, C., Fitzjarrald, D., Johnson, S., and Jones, W.. (1986). "Airborne Doppler lidar measurements," *Appl. Opt.* **25**, 3952-3960
- 3) Boyd, G.D. and Gordon, J.P.. (1961). "Confocal multimode resonator for millimeter through optical wavelength masers," *Bell Sys.Tech. J.*, vol. 40, pp. 489-508.
- 4) Bradley, D.J., and Mitchell, C.J.. (1968). "Characteristics of the Defocused Spherical Fabry-Perot Interferometer as a Quasi-Linear Dispersion Instrument for High Resolution Spectroscopy of Pulsed Laser Sources" *Phil. Trans. R. Soc. Lond.* 263 1140 209-223.
- 5) Bruneau, Didier. (2001). "Mach-Zehnder Interferometer as a Spectral Analyzer for Molecular Doppler Wind Lidar," *Appl. Opt.* **40**, 391-399.
- 6) Bruneau, Didier. (2002). "Fringe-Imaging Mach-Zehnder Interferometer as a Spectral Analyzer for Molecular Doppler Wind Lidar," *Appl. Opt.* **41**, 503-510
- 7) Bruneau, Didier and Pelon, Jacques. (2003). "Simultaneous Measurements of Particle Backscattering and Extinction Coefficients and Wind Velocity by Lidar with a Mach-Zehnder Interferometer: Principle of Operation and Performance Assessment," *Appl. Opt.* **42**, 1101-1114.
- 8) Cattrall, C., Reagan, J., Thome, K., and Dubovik, O.. (2005). "Variability of aerosol and backscatter to extinction ratios of key aerosol types derived from selected Aerosol Robotic Network locations," *J. Geophys. Res.*, 110, D10S11, doi:10.1029/2004JD005124.
- 9) Chen, Wei-Nai, Chiang, Chih-Wei, Nee, Jan-Bai. (2002). "Lidar Ratio and Depolarization Ratio for Cirrus Clouds," *Appl. Opt.* **41**, 6470-6476.
- 10) Connes, P., *Revue d'optique* 35, 37 (1956).
- 11) Connes, P., *J. Phys. RadiLm* 19, 262 (1958).

- 12) de Leon, Erich E. (2012). *Investigations into VHIS*. (Doctoral dissertation). University of Arizona, Tucson, Arizona.
- 13) Ferrare, R.A., Turner, D.D., Brasseur, L.H., Feltz, W.F., Dubovik, O. and Tooman, T.P., (2001). "Raman lidar measurements of the aerosol extinction-to-backscatter ratio over the Southern Great Plains," *Journal of Geophysical Research* 106-17.
- 14) Gimmestad, G., Roberts, D.A., Stewart, J. M., Wood, J.W., (2007). LIDAR System for monitoring turbulence profiles, in the Proceedings from the Advanced Maui Optical and Space Surveillance Technologies, 2007, Maui, HI. (<http://www.amostech.com/TechnicalPapers/2007/Atmospherics/Gimmestad.pdf>)
- 15) Hair, J.W. "A High Spectral Resolution Lidar at 532 nm for Simultaneous Measurement of Atmospheric State and Aerosol Profiles Using Iodine Vapor Filters," Ph.D. Thesis, Colorado State University, Fall 1998.
- 16) Hair, Johnathan W., Hostetler, Chris A., Cook, Anthony L., Harper, David B., Ferrare, Richard A., Mack, Terry L., Welch, Wayne, Ramos-Izquierdo, Luis, and Hovis, Floyd E.. (2008). "Airborne High Spectral Resolution Lidar for profiling aerosol optical properties," *Appl. Opt.* **47**, 6734-6752
- 17) Hercher, Michael. (1968). "The Spherical Mirror Fabry-Perot Interferometer" *Applied Optics*, Vol. 7, Issue 5, pp. 951-966.
- 18) Hoffman, David S., Repasky, Kevin S., Reagan, John A., and Carlsten, John L.. (2012). "Development of a high spectral resolution lidar based on confocal Fabry-Perot spectral filters," *Appl. Opt.* **51**, 6233-6244
- 19) Johnson, J.. (1968). "A high resolution scanning confocal interferometer," *Applied Optics*, vol. 7, no. 6, pp. 1061:1072.
- 20) Khanna, Jaya, Bando, Justin, Sica, R. J., and McElroy, C. Thomas, "New technique for retrieval of atmospheric temperature profiles from Rayleigh-scatter lidar measurements using nonlinear inversion," *Appl. Opt.* **51**, 7945-7952 (2012)
- 21) Kovalev, Vladimir A., Eichinger, William E. (2004). *Elastic Lidar: Theory, Practice, and Analysis Methods*. Wiley Intersciences.
- 22) Liu, Dong, Hostetler, Chris, Miller, Ian, Cook, Anthony and Hair, Johnathan. (2012). "System analysis of a tilted field-widened Michelson interferometer for high spectral resolution lidar," *Opt. Express* **20**, 1406-1420

- 23) Malitson, I. H., (1965). "Interspecimen Comparison of the Refractive Index of Fused Silica," *J. Opt. Soc. Am.* **55**, 1205-1208.
- 24) Matthias, I., et al., 2004: Multiyear aerosol observations with dual wavelength Raman lidar in the framework of EARLINET. *J. Geophys. Res.*, **109**, D13203, doi:10.1029/2004JD004600.
- 25) Measures, Raymond M., "Laser Remote Sensing: Fundamentals and Applications" John Wiley & Sons, 1984.
- 26) Modeling Coherence [FRED Application Note]. Retrieved April 8, 2013, from <http://www.photonengr.com/files/2011/04/appNoteCoherence.pdf>.
- 27) Neal, K.A. (2009), "A Confocal Fabry-Perot Interferometer for Use in Lidar Receivers." Master's Thesis, Montana State University, Bozeman, Montana, USA.
- 28) Nehrir, Amin R., Kevin S. Repasky, John L. Carlsten, 2011: Eye-safe diode-laser-based micropulse differential absorption lidar (dial) for water vapor profiling in the lower troposphere. *J. Atmos. Oceanic Technol.*, **28**, 131–147.
- 29) Optical Coatings [CVI Laser Optics: Material Properties]. Retrieved April 9, 2013, from <http://www.cvimellesgriot.com/products/Documents/TechnicalGuide/Optical-Coatings.pdf>.
- 30) Piironen, P., and Eloranta, E. W. (1994). "Demonstration of a high-spectral-resolution lidar based on an iodine absorption filter," *Opt. Lett.* **19**, 234-236
- 31) Sassen, Kenneth and Dodd, Gregory C., "Lidar crossover function and misalignment effects," *Applied Optics* **21**, 3162-3165 (1982).
- 32) Schwiesow, R. L. and Lading, L.. (1981). "Temperature profiling by Rayleigh-scattering lidar," *Appl. Opt.* **20**, 1972-1979
- 33) She, C. Y., Alvarez II, R. J., Caldwell, L. M., and Krueger, D. A.. (1992). "High-spectral-resolution Rayleigh—Mie lidar measurement of aerosol and atmospheric profiles," *Opt. Lett.* **17**, 541-543
- 34) Shipley, S. T., Tracy, D. H., Eloranta, E. W., Trauger, J. T., Sroga, J. T., Roesler, F. L., and Weinman, J. A.. (1983). "High spectral resolution lidar to measure optical scattering properties of atmospheric aerosols. 1: Theory and instrumentation,"

Appl. Opt. 22, 3716-3724

- 35) Shimizu, H., Lee, S. A., and She, C. Y.. (1983). "High spectral resolution lidar system with atomic blocking filters for measuring atmospheric parameters," Appl. Opt. 22, 1373-1381
- 36) Solomon, S., D. Qin, M. Manning, Z. Chen, M. Marquis, K.B. Averyt, M. Tignor and H.L. Miller (eds.) (2007). *Contribution of Working Group I to the Fourth Assessment Report of the Intergovernmental Panel on Climate Change*. Cambridge University Press, Cambridge, United Kingdom and New York, NY, USA.
- 37) Spinhirne, J.D., (1993). "Micro Pulse Lidar," *IEEE Transactions on Geoscience and Remote Sensing*, 31, 48-55.
- 38) Tenti, G., Boley, C., and Desai, R., (1974). "On the kinetic model description of Rayleigh-Brillouin scattering from molecular gases," *Can. J. Phys.* 52, 285–290
- 39) Thome, Kurt (2007). *OPTI509: Optical Design and Instrumentation II* [Powerpoint Slides].
- 40) Ramaswamy, V., et al., (2001). Radiative forcing of climate change. In: *Climate Change 2001: The Scientific Basis. Contribution of Working Group I to the Third Assessment Report of the Intergovernmental Panel on Climate Change* [Houghton, J.T., et al. (eds.)]. Cambridge University Press, Cambridge, United Kingdom and New York, NY, USA, pp. 349– 416.
- 41) Repasky, Kevin S., John A. Reagan, Amin R. Nehrir, David S. Hoffman, Michael J. Thomas, John L. Carlsten, Joseph A. Shaw, Glenn E. Shaw, 2011: Observational studies of atmospheric aerosols over bozeman, montana, using a two-color lidar, a water vapor dial, a solar radiometer, and a ground-based nephelometer over a 24-h period. *J. Atmos. Oceanic Technol.*, **28**, 320–336.
- 42) Riris, H., Li, S., Numata, K., Wu, S., Yu, A., Burris, J., Krainak, M., and Abshire, J., "LIDAR Technology for Measuring Trace Gases on Mars and Earth," in *Lasers, Sources and Related Photonic Devices*, OSA Technical Digest Series (CD) (Optical Society of America, 2010), paper LMC6.
- 43) Russell, P. B., Morley, B. M., "Orbiting lidar simulations. 2: Density, temperature, aerosol, and cloud measurements by a wavelength-combining technique," Appl. Opt. 21, 1554-1563 (1982)

- 44) Russell, P.B. and Coauthors, 2002: "Comparison of aerosol single scattering albedos derived by diverse techniques in two North Atlantic experiments." *J.Atmos.Sci.*,**59** ,609 –619.
- 45) Vaughn, J.. (1989). "The fabry-perot interferometer: History, theory, practice and applications," IOP Publishing Ltd, Bristol, England and Philadelphia, PA, USA.
- 46) Weitkamp, Claus (Ed.). (2005). *Lidar: Range-Resolved Optical Remote Sensing of the Atmosphere*. Springer Series in Optical Sciences, Volume 102.
- 47) Welton, E.J., J.R. Campbell, J.D. Spinhirne, and V.S. Scott, 2001: Global monitoring of clouds and aerosols using a network of micro-pulse lidar systems. In: *Lidar Remote Sensing for Industry and Environmental Monitoring* [Singh, U.N., T. Itabe, and N. Sugimoto (eds.)]. SPIE, Bellingham, WA, pp. 151–158.
- 48) What is Optical Engineering Software? [FAQ page]. retrieved April 7, 2013, from <http://www.photonengr.com/software/faq/>.
- 49) Yu, A. W., Harding, D. J., Krainak, M., Abshire, J. B., Sun, X., Cavanaugh, J. F., Valett, S. R. and Ramos-Izquierdo, L. A., "Development of an Airborne Lidar Surface Topography Simulator," in *CLEO:2011 - Laser Applications to Photonic Applications*, OSA Technical Digest (CD) (Optical Society of America, 2011), paper AtuA4.
- 50) Zemax User's Manual (2013). *Zemax 13*. Radiant Zemax, Redmond, WA. University of Arizona.